Thermal Creak Induced Dynamics of Space Structures

by

Yool A. Kim

B.S., Aerospace Engineering
University of Virginia, 1992
S.M., Aeronautics and Astronautics
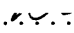Massachusetts Institute of Technology, 1995

SUBMITTED TO THE DEPARTMENT OF AERONAUTICS AND
ASTRONAUTICS IN PARTIAL FULFILLMENT OF THE DEGREE OF

DOCTOR OF PHILOSOPHY
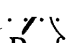at the
MASSACHUSETTS INSTITUTE OF TECHNOLOGY
February 1999
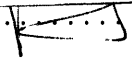
Signature of Author . . .

Department of Aeronautics and Astronautics
October 30, 1998

Certified by. . . . .
Dr. Hugh McManus
Principal Research Engineer
Thesis Committee Chairman

Certified by. . . . .
Professor David Miller
Boeing Assistant Professor of Aeronautics and Astronautics

Certified by. . . . .
Professor S. Mark Spearing
Esther and Harold E. Edgerton Assistant Professor of Aeronautics and Astronautics

Certified by. . . . .
Professor Leon Glicksman
Department of Architecture

Accepted by . . . .
Professor Jaime Peraire
Chairman, Department Graduate Committee
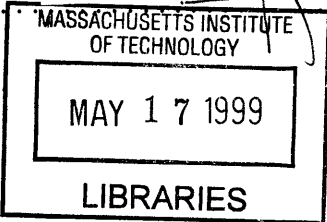
Thermal Creak Induced Dynamics of Space Structures

by

Yool A. Kim

ABSTRACT

Space structures may be subjected to a continually changing thermal environment due to Earth eclipse transients and changes in the spacecraft orientation. During the transient thermal state, components in a structure may experience different amounts of thermal strain due to temperature gradients or coefficient of thermal expansion (CTE) mismatches. Such differential thermal strain can result in stress build-up, especially in statically indeterminate structures. If a nonlinear element, such as a friction dependent joint, is present, stress in the element builds up until the maximum load that can be sustained by friction is reached, at which point the element slips and releases some of the stored elastic energy. Such a nonlinear release mechanism will induce impulsive broadband and possibly high frequency loading to the system, in response to low frequency thermal excitations. This phenomenon is referred to as thermal creak. Nonlinear joints with freeplay, tensioning cables and pulleys, and other structural components that depend on friction and allow relative motion are all examples of potential creak elements that are common in space structures.

An analytical and experimental investigation of the thermal creak phenomenon is presented. A generic model of a thermal creak element is developed to understand the mechanism and to identify the key parameters. The model captures the thermoelastic response, the friction behavior, and the dynamic response of a system. Key parameters that govern the response and quantify the parameters correlated with the energy storage, energy release and energy propagation are identified. The dynamic response is parametrically studied to qualitatively understand the range of behaviors.

Two laboratory experiments were conducted to demonstrate thermal creak and to correlate with the model behavior. The first experiment, a joint characterization, focused on the local thermal creak response and the friction behavior. The model is shown to capture the nonlinear creak response over a range of loading conditions and trends seen in the experiment. The second experiment, a set of thermal tests on a representative deployable structure, investigated the structural response due to thermal creak. Thermal creak events were observed and the resulting dynamics were characterized. The results from the ground experiments and an on-orbit flight experiment conducted by Jet Propulsion Laboratory are used to assess the model and its applicability. The developed model and the experimental results provide a tool for developing thermal creak analysis techniques and mitigation strategies.

Thesis Committee:
  Dr. Hugh McManus, Principal Research Engineer
  Professor David Miller, Assistant Professor of Aeronautics and Astronautics
  Professor S. Mark Spearing, Assistant Professor of Aeronautics and Astronautics
  Professor Leon Glicksman, Professor of Building Technology

ACKNOWLEDGMENTS

5

A special thanks goes to SharonLeah Brown for her moral support and her genuine concern during my M.I.T. years. I was fortunate enough to have a great officemate, Eric Prechtl, who always knew how to make me feel better and made my graduate student life more fun. I will definitely cherish our friendship and the interesting office conversations. Many thanks to Kamyar Ghandi for all of his help throughout the years at M.I.T. and for always being there no matter what time of the day it was or how little sleep he had the night before. I thank Jeremy Yung for all the attention he's given me and for always looking after me. I would like to thank another special friend, Andrew Gnau, who has provided endless moral support even when he was half way around the world. Knowing that I was in his thoughts made me get through some of the toughest times. I am grateful for having such wonderful labmates and friends who helped me pull through by taking care of me and making me laugh. I especially appreciate all the help and support I received during the last six months of my thesis. Thanks for helping me move, giving me a place to stay, giving me wake-up calls, giving me a song, staying up late with me, worrying about me, and thinking of me. Their acts of kindness and friendship made the toughest times during my thesis process the most fun and memorable times.

Finally, I am most thankful for having a strong, supportive family, whose unconditional love has put me where I am now. I thank my father, Kim Chulwhan, my mother, Jun Chunja, my brother, Kim Yoolbum (Roger), and my sister Kim Yoojin (Alex).

TABLE OF CONTENTS

LIST OF FIGURES

LIST OF TABLES

Chapter 1

INTRODUCTION

Society has always been searching for the truth about the beginning of the universe. This quest for the truth inspired NASA's Origins program in 1995 [1]. Origins is a space science program created to answer fundamental questions about the beginning of the universe. The program's mission is to study the evolution of galaxies and to search for Earth-like planets. The program proposed three telescopes to accomplish this mission: Next Generation Space Telescope (NGST), Planetary Finder (PF), and Space Interferometry Mission (SIM). Successful observation of far away and dim stellar objects requires a very large structure to achieve high angular resolution. Some deployable structure or components are necessary to maintain a reasonable launch cost. Further, stringent requirements on the dimensional stability of the structure and the optics are unavoidable. For example, SIM requires alignment of on the order of the fraction of operating wavelength, which is on the order of a nanometer. A precision deployable structure is necessary for such a high performance space based observatory.

There are many technological challenges facing the design of a precision structure. Identifying and understanding all disturbances, including small amplitude disturbances, are critical in the structural and the control system design processes. Several layers of disturbance attenuation strategies, varying from disturbance isolation to optical control, may be implemented to meet the performance requirements and to maximize the observation time. The difficulty in designing an appropriate mitigation or attenuation strategy arises from

lack of knowledge about the characteristics of the disturbances. One of the unfamiliar, yet significant, disturbances is a thermally induced impulsive event referred to as thermal creak.

1.1 Thermal creak mechanism

Thermal creak, sometimes referred to as thermal snap, is a phenomenon where thermally induced stored elastic energy is released via a nonlinear mechanism such as friction [2]. This phenomenon is similar to stick-slip behavior seen in earthquakes [3]. Space structures may be subjected to continually changing thermal environments due to Earth eclipse transients and changes in the spacecraft orientation. During the transient thermal state, components in a structure may strain different amounts due to temperature gradients or coefficient of thermal expansion (CTE) mismatches. Such differential thermal strain can result in stress build-up in statically indeterminate structures. If a nonlinear element, such as a joint which depends on friction, is present, stress in the element builds up until the maximum load that can be sustained by friction is reached, at which point the element slips and releases some of the stored elastic energy. Such a nonlinear release mechanism will induce impulsive broadband and possibly high frequency loading to the system, in response to low frequency thermal excitations. Nonlinear joints with freeplay, tensioning cables and pulleys, and other structural components that depend on friction and allow relative motion are all examples of potential creak elements that are common in space structures. Thus, deployable structures where these nonlinear mechanisms are dominant are especially susceptible to thermal creak.

Thermal creak has been observed in space structures but has been neglected in the design process in the past. For instance, an anomalous behavior was observed in the Hubble Space Telescope flight data, where small disturbances were found throughout the orbit [Figure 1.1]. Later these disturbances were suspected to be caused by thermal creak in the solar array deployment mechanism [2]. Thermal creak is a serious problem because high frequency vibrations are difficult to control due to the limitations in control bandwidth.

Characterizing thermal creak and the resulting dynamics are crucial in designing precision space structures. Thus, the objectives of the thesis are 1) to qualitatively understand the mechanisms of thermal creak and the resulting structural dynamics and 2) to develop an analytical model that can quantitatively characterize thermal creak as a disturbance to a system.
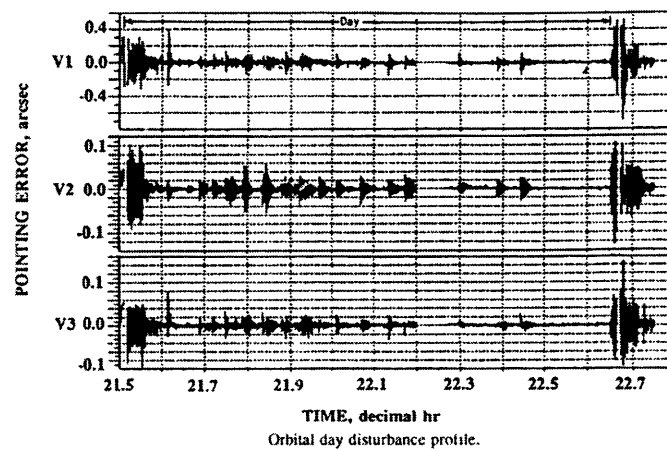
Figure 1.1 Hubble space telescope flight data [2]

1.2 Scope

Sources of thermal creak can be categorized into three groups based on the sources of non-linearities: 1) material, 2) component, and 3) structure. The material level thermal creak includes microcracking of composites and cracking of metal alloy due to material nonlinearity. Component level thermal creak encompasses thermal creak in nonlinear joints, cables, and other deployable mechanisms. Examples of structural level thermal creak include solar array panel creaking and thermal snap-through, where the structure can buckle due to built up thermal stress.

Typical magnitudes of the vibrations induced by thermal creak disturbances at these different levels are qualitatively illustrated in Figure 1.2. The chart shows the relative magni-

tude level for a typical creak source from each category. As the figure indicates, depending on the structural design and the performance metric, the thermal creak of concern can vary from an insignificant material level creak to a catastrophic structural level creak. The plot can vary because the relative magnitude of the different levels of thermal creak are strongly dependent on the following mechanisms: 1) energy storage, 2) energy release (disturbance mechanism), and 3) energy propagation (paths to performance metric).
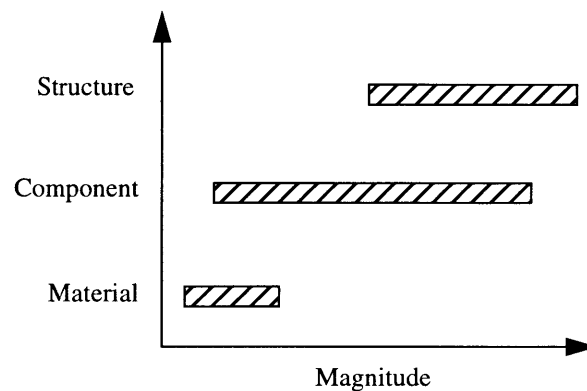
Figure 1.2 Thermal creak category

These key parameters depend on the details of the thermal load, nonlinear mechanisms in the system, and the system dynamics. The exact location, time, magnitude, and the frequency content of thermal creak are difficult to predict because good physical understanding and models that describe the mechanism are lacking. Developing such a deterministic model requires knowledge of all the key parameters affecting thermal creak response, which may involve characterizing a variety of nonlinear mechanisms and complex load paths. Such tasks are difficult to complete and are impractical for spacecraft design purposes. A simpler approach that can provide bounds on the characteristics of the vibrations induced by thermal creak is desirable at a preliminary design stage. Such a simple approach is sufficient from a design point of view and for applications of disturbance attenuation strategies.

1.3 Previous work

Thermally induced disturbances have received little attention in the past, and only a limited effort to understanding thermal creak has been made. As a result, no documented work on thermal creak has been found in the open literature. Both experimental and analytical work are lacking. No directly measured data exist and no fundamental understanding of thermal creak has been achieved. In order to better understand and characterize the mechanisms of thermal creak and the resulting dynamic response of the structure, both analytical and experimental work done towards characterizing these mechanisms are reviewed and evaluated in this section.

1.3.1 Energy storage mechanism

The ability to trigger thermal creak depends on the loading condition and the structural design. Characterization of the thermal environment and the thermoelastic response of the structure are required to determine the stress state. A number of analytical and numerical tools used for the thermal analysis of space structures are available. Simple analytical methods to calculate temperature histories for simple geometry are used in [4]. Mahaney and Strode used a finite difference method to calculate the thermal response of a truss structure in low Earth orbit [5]. Several simplifying assumptions were made: the truss members were isothermal, and the axial and the circumferential conduction were neglected. Member-to-member shadowing was neglected in this analysis, but such effects on the thermal response are investigated in [6]. In general, a commercial thermal analysis tool in conjunction with a structural analysis tool is commonly used to obtain temperature distributions and static structural deformations for a complex geometry. Many finite element model packages have the capabilities (such as view factor calculations) to include radiative heat transfer. Refer to [7] for a summary of the available tools and approaches used for calculating thermostructural response of space structures, including truss structures.

1.3.2 Energy release mechanism

The nonlinear energy release mechanisms include joints that depend on friction and allow relative motion. In this section, previous work on characterization of nonlinear joints is reviewed. Various friction models are discussed to evaluate the applicability of the models to thermal creak.

Joints

Joints in space structures may introduce nonlinearities into the structure due to friction, impacts and deadbands. Such joints contribute significantly to passive damping in a structure because of the inherent dissipative mechanisms in these joints. Energy is dissipated via friction and impacts due to relative motion in the joints. A considerable amount of both analytical and experimental work has been done in effort to quantify the nature of effects of joints on damping and structural dynamics. Joints that display such nonlinear behavior may be a potential source of thermal creak and thus they are discussed in this section. In addition, some friction laws and models applicable to creaking joints as well as other creak source elements are reviewed.

Several types of joints that display stick-slip behavior due to friction have been analyzed. Ferri developed a generic sleeve joint model to study the effects of these joints on structural damping [8]. In this joint concept, a concentric outer sleeve fits around the end of a mating structural member such as a beam. The friction exists between the sleeve and the beam. A joint was also considered by Hertz and Crawley [9]. A pin joint was considered in this technical note where the relative motion between the pin and the socket caused energy dissipation. Onoda et al. modeled a two-dimensional truss joint with a backlash to study the effects of backlash on energy dissipation [10]. More friction-dependent joints are presented in [11].

A scaled down deployable truss structure for the Joint Damping Experiment (JDX) was constructed at the University of Utah to study the effects of joints on damping and structural dynamics. Analytical models and experimental results for the JDX are presented in

[12], [13], and [14]. The JDX truss joints are pinned joints with tang-clevis mechanism to allow one rotational degree of freedom. Relative motion in the axial direction is allowed due to the clearance in the pins, which introduces friction damping and nonlinearities. This type of joint was also present in the deployable truss for the Middeck zero-gravity Dynamics Experiment (MODE) [15].

Joint modeling

Nonlinear joints are difficult to model because of the complex load paths in the joint as well as the various geometric and friction parameter values that are specific to the joint design [16]. Simplified analytical joint models have been developed to characterize qualitative behaviors of the jointed structures. These joint models consist of a friction model that describes the friction forces and a structural model that describes the behavior of the joint under loading.

Most of the models assume that the friction mechanism is governed by the Coulomb's law of dry friction. Despite the fact that the Coulomb's friction law is a simple law, many complex systems have been modeled based on this model. Some modifications of this friction law are made specific to a certain design or component [11]. A displacement dependent friction model where the normal force depends on the displacement was incorporated in the analysis of a space truss joint in [9]. Reference [8] used a similar displacement dependent friction model. An amplitude dependent friction model, where the friction force depends on the vibration amplitude, has also been developed and described in [17]. Reference [17] contains other analytical friction models of interest. Finally, Folkman et al. attempted to use friction elements available in a finite element package, but they found some problems with convergence [14].

The key problem with these joint models is accurately predicting parameters that capture the characteristics of the friction mechanisms and joint behavior. Parameters such as the coefficient of friction and joint deadband are difficult to predict. These parameters need to be determined experimentally because they are specific to the interface and the joint

design. Experimental methods such as force displacement plots of a joint have been commonly used to characterize joints [14]. The joint stiffness, gaps, and the static friction between the mating surfaces in the joint can be determined from such plots. Another powerful experimental technique for joint characterization is the force-state mapping technique [18]. The force transmitted by the joint is assumed to be a function of the instantaneous state displacement and velocity. The displacement, velocity, acceleration, and the applied force are measured at each time interval and a map of the total force transmitted to the surrounding element (applied force minus the inertial force) as a function of the state, is constructed. Here the effects of the joint on the system is modeled as a force that the surrounding structure sees. The force-state mapping technique has been applied for joint characterization of the JDX truss, MODE truss and Precision Truss Structure developed by Colorado and NASA Langley [13], [15], and [19].

A specific model for each component was used in the past. The friction models used in these joint models were applicable for capturing the damping and the nonlinear response due to friction. The friction characteristics that allow thermal creak to occur, such as stick-slip, and the parameters that govern these characteristics, may not be captured by these models. A generic model for a creak source that incorporates friction may be more appropriate for obtaining bounds on the response rather than accurately capturing the response. A survey of various friction models is presented in Ref. [20]. Friction models can range from a simple Coulomb friction model to a complex dynamic friction model that captures microslips or presliding displacement, stick-slip behavior, viscous friction, and memory dependence.

1.3.3 Energy propagation mechanism

The dynamics of nonlinear structures are difficult to characterize due to the nonlinear variations of the response with varying excitations and other environmental and system parameters. Several analytical methods have been used to incorporate joint nonlinearities and to compute the structural response of a nonlinear truss. Describing function method is

a common approach to model nonlinear effects, where harmonic balance in conjunction with a Newton-Raphson iteration method is applied to solve the nonlinear dynamic equations. Bowden and Webster employed describing functions to model the joint nonlinearity in a truss structure and to characterize the structural behavior [21 and 22]. Variations of describing functions have also been used to handle specific structures. Masters developed an algorithm that used a combination of alternate frequency-time domain and describing function methods to characterize the dynamic behavior of the MODE truss structure [15]. Wang used a method similar to the describing functions and applied the discrete Fourier transform to deal with the strong nonlinearity introduced by joint clearances [23]. However, in these earlier problems, the interest lies in the steady state response of the structure, and the effects of the nonlinearities are observed in an average sense. The structural vibration induced by thermal creak is a transient problem, and thus the describing functions method may not apply. An alternative method such as direct time integration can be used for transient analyses, but this method can be computationally intensive and time consuming [22].

1.4 Thesis overview

The focus of the thesis is on component level thermal creak as a key source of disturbance in a precision space structure, such as a truss structure with nonlinear joints. Simple analytical models are first developed in Chapter 2 to 1) understand the fundamental mechanisms of thermal creak and 2) to identify the key parameters that dictate the thermal creak response and the structural behavior. Two experiments are conducted in a laboratory environment: joint characterization and thermal creak induced dynamics characterization. The joint characterization experiment entails measurement of local thermal creak response. The structural response due to thermal creak is characterized in the dynamics experiment. The objectives of the experiments are to 1) demonstrate thermal creak, 2) characterize the micro-motions and friction mechanism at the creak source, 3) characterize the dynamic response due to thermal creak, and 4) assess the models. Chapter 3 presents the descriptions of the experimental hardware and procedures used to assess these models. The

results and model correlations are discussed in Chapter 4. A flight experiment was conducted by the Jet Propulsion Laboratory in effort to investigate thermal creak in a deployable structure. The description of the flight experiment and the results are the subject of Chapter 5. Finally, the thesis concludes with the recommendations and contributions in Chapter 6.

Chapter 2

THERMAL CREAK MODEL

A general framework for thermal creak modeling is presented in this chapter. The following approach is taken in developing the model. A simple model of a single degree of freedom system with a nonlinearity introduced due to thermal creak is first developed as presented in [24]. In this system, the creak element behaves statically. The nonlinear response of the creak element and the ensuing dynamic response are investigated. Next, a multi-degree of freedom system with thermal creak is developed where inertia is included in the creak element. The response becomes more complex.

The model captures the thermoelastic response, the friction behavior, and the dynamic response of a system. Key parameters that govern the responses and quantify the parameters, correlated with the energy storage, energy release and energy propagation, are identified. The dynamic responses are parametrically studied to qualitatively understand the range of behaviors. To illustrate the application of the model, thermal creak in a proposed telescope is analyzed as an example.

2.1 Problem statement

Consider a creak element composed of a pin with mass m_1 on a slider with mass m_2. A mass M is attached to the creak element via a spring and a damper whose stiffness and damping coefficient are K and C, respectively. A normal load N is applied to the pin and the slider such that friction holds them together [Figure 2.1]. The pin is connected to a

spring whose stiffness, length, and coefficient of thermal expansion (CTE) are k_1, l_1, and α_1, respectively. The slider is attached to a spring whose stiffness, length, and CTE are k_2, l_2, and α_2, respectively. Initially, the temperatures of the springs are at a stress free temperature of T_{ref}. A thermal load is applied to the creak element such that the temperatures of the springs attached to the pin, T_1, and the slider, T_2, change with time. During this thermal transient, the pin and the slider quasistatically move together and the internal forces build up in the springs due to the different stiffnesses, different temperatures, and the CTE mismatch. The pin and the slider are stuck together until the critical friction, F_s, at the interface can no longer sustain the stress built up in the springs. At this critical state, the pin slips relative to the slider as the friction reduces to a lower value, F_k. Further, the attached mass M is excited due to the slip motion as the creak element acts as a disturbance to the attached system. Once the friction is reduced and the stored elastic energy released, the pin and the slider sticks again and the forces in the springs build up until the next slip occurs. This stick-slip motion repeats as the temperature continues to change, stopping if the pin reaches a stop at either side.
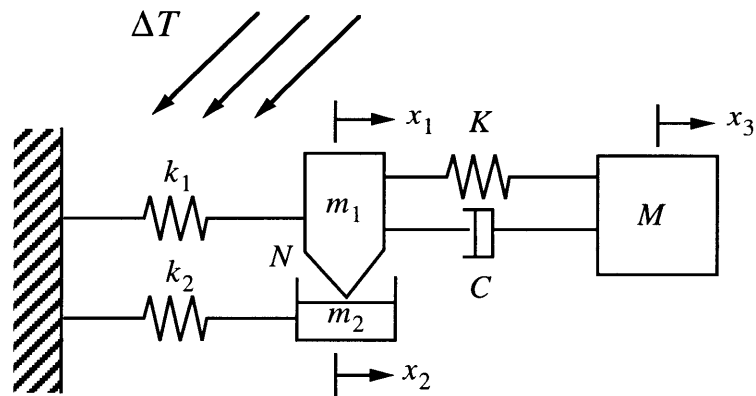
Figure 2.1   Schematic representation of thermal creak element

In this chapter, the responses of the creak element and the attached mass are investigated. The responses are characterized by determining

1. necessary conditions for thermal creak to occur

2. energy release profile

3. magnitude of energy release

4. frequency of energy release

5. transmissibility of thermal creak disturbance to system performance

A few simplifying assumptions are made in developing the model. First, the friction behavior is assumed to be Coulombic. The stress build up rate is assumed to be high enough and the Stribek parameter is small enough such that the friction behavior can be approximated as Coulombic. Second, the pin does not reach the stops during the thermal load time period of interest. Finally, the creak element is initially at rest with no initial stress in the springs.

2.2 Static thermal creak analysis

The analysis begins with a simple model where the creak element (m_1 and m_2) is assumed to be massless. The governing equation for the creak element is first derived. The equation is nondimensionalized to identify the key parameters and to qualitatively understand the physical significance of the parameters. The dynamic response of the attached mass (M) is then obtained. The creak response and the resulting dynamic response are parametrically studied to observe the range of behaviors.

2.2.1 Thermal creak response

The response of the static thermal creak element without the attached mass M is obtained in this section. The states of the pin and the slider can be determined based on the equilibrium condition, the constitutive relations, and the compatibility relation. The equilibrium equation of the creak element as a stuck system is first written.

$$F_1 + F_2 = 0 \qquad (2.1)$$

where F_1 and F_2 are the internal forces in the springs attached to the pin and the slider, respectively. The constitutive relations are written as follows.

$$F_1 = k_1(x_1 - x_1^t)$$
$$F_2 = k_2(x_2 - x_2^t)$$
(2.2)

where x_1 and x_2 are the total displacements of the pin and the slider, respectively. The thermal displacements of the pin and the slider are x_1^t and x_2^t, respectively and they are defined as

$$x_1^t = \alpha_1 \Delta T_1 l_1 \qquad x_2^t = \alpha_2 \Delta T_2 l_2$$
(2.3)

where

$$\Delta T_1 = T_1 - T_{ref}$$
$$\Delta T_2 = T_2 - T_{ref}$$
(2.4)

Finally, the compatibility relation is established by introducing the displacement of the pin relative to the slider, Δx.

$$\Delta x = x_1 - x_2$$
(2.5)

The governing equation of the system in a stuck mode results by substituting Eq. (2.2) into Eq. (2.1) and eliminating the variable x_2 using Eq. (2.5).

$$x_1 = \left(\frac{1}{k_1 + k_2}\right)[k_1 x_1^t + k_2 x_2^t + k_2 \Delta x] \qquad \text{for } \left| k_1(x_1 - x_1^t) \right| < F_s$$
(2.6)

When the internal force attains the static friction load, the pin and the slider instantaneously slip as the internal force is balanced by friction.

$$F_1 = -F_f$$
$$F_2 = F_f$$
(2.7)

Substituting the constitutive relation given in Eq.(2.2) into Eq. (2.7), the independent equations for the states of the pin and the slider result.

$$k_1 x_1 = -F_f + k_1 x_1^t$$

$$k_2 x_2 = F_f + k_2 x_2^t$$

$$(2.8)$$

Based on the Coulombic friction model, the friction value in Eq. (2.8) are computed as

$$F_f = \begin{cases} F_k & \text{for } k_1(x_1 - x_1^t) > 0 \\ -F_k & \text{for } k_1(x_1 - x_1^t) < 0 \end{cases} \tag{2.9}$$

where F_k is the kinetic friction.

Nondimensionalized equilibrium equation

In this section the equations governing the creak response are rewritten in a dimensionless form. Key nondimensional parameters are identified and their effects on the response are discussed.

First, the characteristic length x_1^* is introduced to define the dimensionless displacements ξ_1, ξ_2, ξ_1^t, and ξ_2^t. The characteristic length is the critical displacement at which a slip would occur under the condition that the pin has zero thermal strain ($x_1^t = 0$) [Eq. (2.2)].

$$x_1^* = \frac{F_s}{k_1} \qquad \xi_1 = \frac{x_1}{x_1^*} \qquad \xi_2 = \frac{x_2}{x_1^*} \qquad \xi_1^t = \frac{x_1^t}{x_1^*} \qquad \xi_2^t = \frac{x_2^t}{x_1^*} \tag{2.10}$$

The characteristic force is the static friction F_s such that the dimensionless forces in the system can be defined.

$$f_1 = \frac{F_1}{F_s} \qquad f_2 = \frac{F_2}{F_s} \qquad f_f = \frac{F_f}{F_s} \qquad f_k = \frac{F_k}{F_s} \tag{2.11}$$

Equations (2.1) and (2.2) are normalized by the characteristic force F_s to nondimensionalize the equilibrium and constitutive relations.

$$f_1 + f_2 = 0 \qquad \text{stuck system}$$

$$\left. \begin{array}{l} f_1 = -f_f \\[2mm] f_2 = f_f \end{array} \right\} \quad \text{sliding system} \qquad (2.12)$$

$$\left. \begin{array}{l} f_1 = \xi_1 - \xi_1^t \\[2mm] f_2 = \kappa(\xi_2 - \alpha_r \xi_1^t) \end{array} \right. \qquad \text{constitutive} \qquad (2.13)$$

where the dimensionless parameters α_r and κ are defined as follows.

$$\alpha_r = \frac{x_2^t}{x_1^t} \qquad \kappa = \frac{k_2}{k_1} \qquad (2.14)$$

The nondimensionalized compatibility relation is obtained by normalizing Eq. (2.5) by the characteristic length x_1^*.

$$\Delta\xi = \xi_1 - \xi_2 \qquad \text{compatibility} \qquad (2.15)$$

The equation governing the creak behavior in the stuck region transforms into the following dimensionless form when the constitutive relation, Eq. (2.13), is substituted into the equilibrium equation, Eq. (2.12). The compatibility relation in Eq. (2.15) is used to eliminate ξ_2.

$$\xi_1 = \left(\frac{\kappa\alpha_r + 1}{\kappa + 1}\right)\xi_1^t + \left(\frac{\kappa}{\kappa + 1}\right)\Delta\xi \qquad \left|\xi_1 - \xi_1^t\right| < 1 \qquad (2.16)$$

The slip motion is described by the following nondimensionalized equations by substituting the constitutive relations into the equilibrium equation.

$$\xi_1 = -f_f + \xi_1^t$$

$$\xi_2 = \frac{f_f}{\kappa} + \alpha_r \xi_1^t$$

$$f_f = \begin{cases} f_k & \text{for } \xi_1 - \xi_1^t > 0 \\ -f_k & \text{for } \xi_1 - \xi_1^t < 0 \end{cases}$$

(2.17)

Equations (2.16) and (2.17) show that the dimensionless parameters dictating the creak response are α_r, f_k, and κ. The thermal strain mismatch parameter α_r is the ratio of the thermal displacements between the pin and the slider. It can be a function of time, but it is assumed to be constant from hereon for simplicity. The next key parameter, f_k, is the ratio between the kinetic and the static friction. Finally, κ is the ratio of the stiffnesses between the components,.

The physical significance of these key dimensionless parameters is revealed by observing the creak behavior under the limiting cases. Assuming that $\Delta\xi = 0$, Eq. (2.16) indicates that as α_r approaches one, the total displacement approaches the thermal displacement, and thus the internal force in the creak element approaches zero. The thermal strain mismatch parameter α_r is then the key parameter that represents the ability of the creak element to store energy, where $|1 - \alpha_r| = 0$ corresponds to zero stored strain energy. The relation of f_k to the energy parameters of the system is determined by observing the response with the limiting values of f_k. The value of f_k can range from zero to one based on the Coulombic friction model. Recall that f_k is balanced by the internal force at slip [Eq. (2.17)]. As a result, when f_k is zero, the internal force reduces to zero and all of the stored energy is released at slip. On the other extreme side, when f_k equals one, the internal force remains at the maximum level, hence eliminating stick-slip. The pin and the slider continuously slide and the amount of energy released per slip approaches zero as f_k approaches one. The dimensionless parameter f_k is therefore associated with the ability of the creak element to release energy during slip, where $1 - f_k = 0$ corresponds to no energy release at slip.

Finally, the stiffness ratio κ acts as a scaling factor to the displacements of the pin and the slider. The effects of κ on the creak response are discussed in the disturbance characterization section.

Disturbance characterization

The nondimensional equations (2.16-2.17) show that the creak response ξ_1 is a sum of a linear thermoelastic response ξ_1^t and a nonlinear friction-induced function $\Delta\xi$. The thermoelastic response is governed by the thermal load applied to the system and is generally a quasi-static response. The relative motion, a sudden change in $\Delta\xi$, occurs as a result of the energy release during slip via friction. Such a relative motion is introduced as a disturbance to the surrounding structure and thus the nonlinear function $\Delta\xi$ is a measure of the disturbance. In this section, the profile, the magnitude, and the frequency of $\Delta\xi$ are determined to characterize thermal creak as a disturbance.

The profile of $\Delta\xi$ is governed by the friction behavior at the interface. Because the creak element is static and no relative motion is allowed until the critical state is attained, $\Delta\xi$ instantaneously jumps to a new constant value at slip. Thus $\Delta\xi$ has a step profile at each slip point. The magnitude of these steps, denoted by A_c, is then the difference in the relative displacements just before and after slip.

$$A_c = \Delta\xi|_{slip+} - \Delta\xi|_{slip-} \tag{2.18}$$

The relative displacement just before slip can be determined from Eq. (2.17) by equating $f_f = 1$ and solving for $\Delta\xi$ from the compatibility relation. Similarly, the relative displacement just after slip can be obtained from Eq. (2.17) by substituting $f_f = f_k$. As a result, the magnitude of the step becomes

$$A_c = \left(1 + \frac{1}{\kappa}\right)(1 - f_k) \tag{2.19}$$

Equation (2.19) indicates that the step function at each slip is constant. Because A_c is related to the energy release during slip, only the friction ratio and the stiffness ratio are present in the equation.

Before deriving the expression for the creak frequency, the condition that guarantees an occurrence of creak is first established by introducing the critical thermal displacement, $(\xi_1^t)_{cr}$. The critical thermal displacement is defined as the thermal displacement at which the initial slip occurs. Based on this definition no slip occurs if the thermal displacement is always less than the critical value, $\xi_1^t < (\xi_1^t)_{cr}$. To obtain $(\xi_1^t)_{cr}$, Eq. (2.16) is first substituted into the top equation in Eq. (2.17). Then the equation is solved for ξ_1^t by applying the conditions that $f_f = 1$ just before slip and that initially $\Delta\xi = 0$.

$$(\xi_1^t)_{cr} = \pm\frac{1}{\kappa}\left(\frac{\kappa+1}{1-\alpha_r}\right) \tag{2.20}$$

The critical thermal displacement is inversely proportional to the energy storage capacity of the creak element. As the energy storage capacity, proportional $(|1-\alpha_r|)$,approaches zero, $(\xi_1^t)_{cr}$ approaches infinity.

If ξ_1^t is monotonic and the condition for the initial slip is met, a periodic repeatable slip behavior may be observed. The period of the creak P_c is defined here as the time elapsed between two successive slips. The period is then equal to the time required for the internal forces to build up from the reduced friction to the critical force. The period is implicitly defined as

$$\int_0^{\omega P_c} \left|\dot{\xi}_1 - \dot{\xi}_1^t\right| d\tau = 1 - f_k \tag{2.21}$$

where $(1/\omega)$ is the characteristic time and τ is the dimensionless time defined as $\tau = \omega t$. The characteristic time $(1/\omega)$ is assumed to be arbitrary for time being. The dot over the variable represents the first time derivative of the variable. The rate of change of the displacement is obtained by taking the time derivative of Eq. (2.16).

$$\dot{\xi}_1 = \left(\frac{\kappa\alpha_r + 1}{\kappa + 1}\right)\dot{\xi}_1^t \tag{2.22}$$

Note that $\Delta\dot{\xi} = 0$ since no relative motion is allowed while the creak element is in the stuck mode. By substituting Eq. (2.22) into Eq. (2.21) and assuming that $\dot{\xi}_1^t > 0$, the following expression results.

$$\int_0^{2\pi(\omega/\omega_c)} \dot{\xi}_1^t d\tau = \frac{\kappa + 1}{|1 - \alpha_r|}\left(\frac{1 - f_k}{\kappa}\right) \tag{2.23}$$

where the creak frequency, ω_c is related to the period as $\omega_c = (2\pi)/P_c$. Equation (2.23) is a general expression for the creak frequency. Depending on the thermal response of the creak element, the creak frequency can be a function of time. To obtain an explicit expression for ω_c, the integral in Eq. (2.23) needs to be evaluated for a specified thermal displacement function. For a ramp thermal displacement, $\dot{\xi}_1^t = C_t$, the creak frequency can be computed from Eq. (2.23) as follows.

$$\omega_c = 2\pi\omega C_t \left|\frac{1 - \alpha_r}{\kappa + 1}\right|\left(\frac{\kappa}{1 - f_k}\right) \tag{2.24}$$

Note that the creak frequency is proportional to the thermal displacement rate C_t. Equation (2.24) further reveals that the creak frequency is inversely proportional to energy release (proportional to $1 - f_k$) and the energy storage capacity (proportional to $|1 - \alpha_r|$). As the amount of energy released or the energy storage capacity increases, the creak frequency decreases.

As an example, the displacements of the pin and the slider are computed for a typical exponential thermoelastic response of the pin.

$$\xi_1^t = A_t\left(1 - \exp\left(-\frac{\tau}{\tau_0}\right)\right) + B_t \tag{2.25}$$

The numerical values used in this example are listed in Table 2.1. The creak response is computed by numerically integrating Eqs. (2.16) and (2.17). The resulting displacements are plotted in Figure 2.2. The pin and the slider move together following the thermal displacement until the critical state is attained.   At this point, the pin begins to follow the thermoelastic response in discrete steps. The initial slip occurs when the thermal displace-

TABLE 2.1 Parameters for numerical example

Parameter	Numerical Value
A_t	2
B_t	1.78
τ_0	100
f_k	0.8
α_r	0
κ	1
ω	1
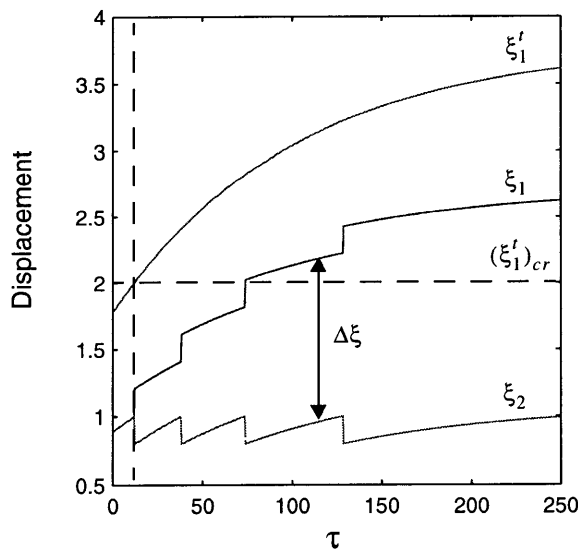
Figure 2.2 Displacements of static creak element
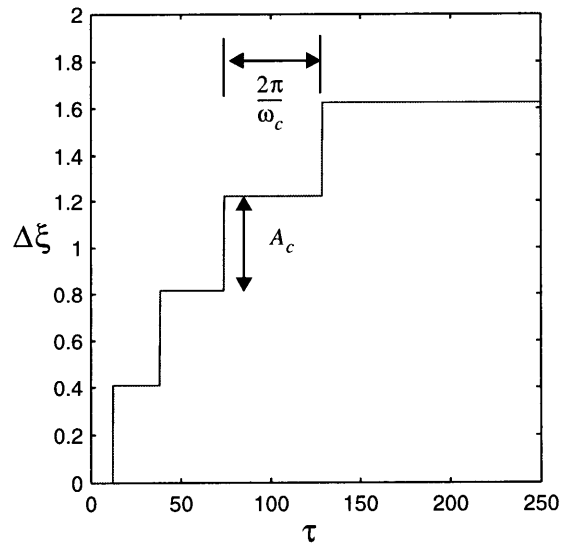
Figure 2.3 Relative displacement in static creak element

ment reaches the dimensionless critical thermal displacement, in this case two. The step size of $\Delta\xi$ remains constant at $A_c = 0.4$ as expected from Eq. (2.19). The creak frequency, however, is a function of time as illustrated by the increasing time between each slip. Note that the frequency decreases as ξ_1^t approaches the thermal equilibrium.

2.2.2 Structural response

The response of a static creak element was analyzed in the previous section. The governing equations indicated that the creak element moves in fixed discrete steps with frequency ω_c [Eqs. (2.16-2.17)]. Such periodic step displacements cause the attached mass (M) shown in Figure 2.1 to oscillate. In this section, the ensuing structural response is investigated. The equation of motion for the single degree of freedom (SDOF) system with thermal creak is derived and nondimensionalized. The transmissibility of the creak disturbance to the system performance is discussed and parametrically studied in the numerical results section.

The static creak response derived in Section 2.2.1 is slightly modified to include the effect of the structural response. The equilibrium equation is rewritten to include the response of the mass.

$$F_1 + F_2 = F_3 \tag{2.26}$$

where F_3 is the restoring force due to the spring attached to M. The additional constitutive relation for this spring is

$$F_3 = K(x_3 - x_1) \tag{2.27}$$

where the displacement of the mass is denoted by x_3 as shown in Figure 2.1 Parallel to Section 2.2.1, the constitutive relations, Eqs. (2.2) and (2.27) are substituted into Eq. (2.26) to obtain the creak response. The same procedure outlined in the nondimensionalization section is then applied to obtain the new creak response in a dimensionless form.

$$\xi_1 = \left(\frac{\kappa\alpha_r + 1}{\kappa + \kappa_0 + 1}\right)\xi_1^t + \left(\frac{\kappa}{\kappa + \kappa_0 + 1}\right)\Delta\xi + \left(\frac{\kappa_0}{\kappa + \kappa_0 + 1}\right)\xi_3 \qquad \text{for } \left|\xi_1 - \xi_1^t\right| < 1 \quad (2.28)$$

where ξ_3 is the dimensionless displacement of M and κ_0 is the stiffness ratio between the attached mass and the pin.

$$\xi_3 = \frac{x_3}{x_1^*} \qquad \kappa_0 = \frac{K}{k_1} \qquad\qquad (2.29)$$

The remaining dimensionless variables and parameters were defined in Section 2.2.1. At slip, the creak response is governed by the following equations.

$$\xi_1 = -\frac{f_f}{1 + \kappa_0} + \left(\frac{1}{1 + \kappa_0}\right)\xi_1^t + \left(\frac{\kappa_0}{1 + \kappa_0}\right)\xi_3$$

$$\xi_2 = \frac{f_f}{\kappa} + \alpha_r\xi_1^t$$

$$f_f = \begin{cases} f_k & \xi_1 - \xi_1^t > 0 \\ -f_k & \xi_1 - \xi_1^t < 0 \end{cases} \qquad (2.30)$$

Equations (2.28) and (2.30) are almost identical to Eqs. (2.16) and (2.17), except that the creak response is now a function of ξ_3 and κ_0 due to coupling with the structural response. The strength of coupling between the creak element and the attached mass are measured by κ_0 [Eqs. (2.28) and (2.30)]. As κ_0 approaches zero, the effect of the structural response on the creak response becomes negligible. The coupled creak response is still qualitatively the same as that derived in Section 2.2.1. The relative displacement $\Delta\xi$ changes in discrete steps, exciting the attached system.

The equation of motion for the attached mass is now derived based on the force balance on the mass. Note that no external force is applied to the mass.

$$M\ddot{x}_3 + C\dot{x}_3 + Kx_3 = Kx_1 \qquad (2.31)$$

To nondimensionalize Eq. (2.31) the dimensionless time τ is first defined.

$$\tau = \omega t \qquad \omega^2 = \frac{K(k_1 + k_2)}{M(k_1 + k_2 + K)} \tag{2.32}$$

The inverse of the characteristic time, ω, is the natural frequency of the linear system when the pin and the slider are stuck together.

Equation (2.31) is divided by M to rewrite the equation in terms of ω and the stiffness ratios.

$$\ddot{x}_3 + 2\zeta\omega\dot{x}_3 + \omega^2\left(\frac{\kappa + \kappa_0 + 1}{\kappa + 1}\right)x_3 = \omega^2\left(\frac{\kappa + \kappa_0 + 1}{\kappa + 1}\right)x_1 \tag{2.33}$$

where the damping ratio ζ is defined as

$$\zeta = \frac{C}{2M\omega} \tag{2.34}$$

Using the chain rule, the acceleration and the velocity can be written in terms of the dimensionless time.

$$\frac{dx}{dt} = \omega\frac{dx}{d\tau}$$
$$\frac{d^2x}{dt^2} = \omega^2\frac{d^2x}{d\tau^2} \tag{2.35}$$

Equation (2.33) is nondimensionalized by normalizing the equation by x_1^* and substituting Eq. (2.35) into Eq. (2.33).

$$\ddot{\xi}_3 + 2\zeta\dot{\xi}_3 + \left(\frac{\kappa + \kappa_0 + 1}{\kappa + 1}\right)\xi_3 = \left(\frac{\kappa + \kappa_0 + 1}{\kappa + 1}\right)\xi_1 \tag{2.36}$$

Equation (2.28) is finally substituted into Eq.(2.36) to arrive at the following equation of motion for the system dynamics.

$$\ddot{\xi}_3 + 2\zeta\dot{\xi}_3 + \xi_3 = \left(\frac{\kappa\alpha_r + 1}{\kappa + 1}\right)\xi_1^t + \left(\frac{\kappa}{\kappa + 1}\right)\Delta\xi \tag{2.37}$$

Equation (2.37) is the governing equation for thermal creak induced vibrations of a SDOF system. The displacements of the pin and the slider are treated as internal degrees of freedom. This equation of motion must be solved simultaneously with Eqs. (2.28) and (2.30) to fully describe the system response. In the regime where the disturbance and the structure are weakly coupled, $\kappa_0 \ll 1$, Eqs. (2.28) and (2.30) reduce to Eqs. (2.16) and (2.17). The creak response can then be computed independent from the structural response.

Equation (2.37) shows that the system can be excited by two types of thermally induced forcing functions. First, the thermoelastic response (ξ_1^t) may cause the structure to vibrate as first observed by Boley [25]. Significant dynamic response results if the characteristic thermal response time is on the order of the structural characteristic time. In most cases, the dynamics introduced by the thermoelastic response can be neglected because the thermal response time is much greater than the structural response time. The second forcing function is the thermal creak response, $\Delta\xi$. The creak response is a series of discrete relative motion of the components in the system as seen in Section 2.2.1. Equation (2.37) implies that this nonlinear response appears as a series of step loads applied to the system performance.

Note that the characteristics of the dynamic response depends the load path from the creak location to the system, represented by κ_0, and the characteristics of the thermal creak response, represented by $\Delta\xi$. As κ_0 approaches zero, all of the energy released by the creak element at slip is transferred to the system. As κ_0 approaches infinity, the dynamic response of the system approaches zero and all of the released energy remains in the creak element.

Transmissibility

Assuming that the creak response is weakly coupled to the structural response and that the creak frequency is constant, the transmissibility of the creak disturbance to the performance metric, H, is defined as follows.

$$H\left(\frac{\omega_c}{\omega}\right) = \frac{\left|\ddot{\xi}_3\right|_{max}}{\left(\frac{\kappa}{\kappa + 1}\right)A_c} \tag{2.38}$$

The transmissibility can be measured by the ratio of the maximum amplitude of the acceleration to the step force imparted on the structure at each slip. Based on this definition, the static contribution to the response is neglected. In addition, the stepping is assumed to be periodic and repeatable. Substituting Eq. (2.19) into Eq. (2.38), the transmissibility is now defined as

$$H\left(\frac{\omega_c}{\omega}\right) = \frac{\left|\ddot{\xi}_3\right|_{max}}{1 - f_k} \tag{2.39}$$

The attached single degree of freedom (SDOF) system in Eq. (2.37) can easily be replaced by a multiple degrees of freedom (MDOF) system. A conventional structural dynamics analysis method can then be used to compute the structural response. However, one of the shortcomings of the modal analysis or the finite element analysis is that many degrees of freedom may be required if high frequency response is of interest. Due to the impulsive nature of thermal creak, high frequency local modes are also excited. A conventional structural dynamics model may not capture the local response accurately. Therefore, another dynamics model may be necessary to capture the high frequency responses.

Wave propagation models have been used for impulsive loading where high frequency vibrations were of concern [26, 27]. Because thermal creak disturbance introduces a step load into the system the Fourier components of the disturbance contain all frequencies. However, the disturbance may be distorted during propagation due to the dispersive effects of the medium or any discountinuities in the medium [28]. Hence not all Fourier compo-

nents of the disturbance are transmitted to the performance. To determine the families of frequencies that are not transmitted to the performance, the dispersive relation for the medium needs to be derived and the transmissions of the waves at the discontinuities need to be considered. Such analytical work is outside the scope of this thesis and thus interested reader should refer to [29].

In summary, in a MDOF system, the transmissibility of thermal creak to the system performance varies depending on the frequency spectrum of interest. In the structural dynamics regime, where global modes dominate, the transmissibility is a function of κ_0. In the acoustic regime, where wave propagation dominates, the transmissibility is a function of wave properties such as the wave speed and the transmission coefficients.

2.2.3 Results

Qualitative results for the static thermal creak model are presented in this section. First, the following assumptions are made.

1. The thermoelastic response is a constant ramp, $\xi_1^t = C_t \tau$

2. The inverse of the thermal response time is assumed to be much smaller than ω to avoid exciting the system due to the thermoelastic response, ($C_t \ll \omega$)

3. $\alpha_r \geq 0$

A range of behavior for the attached mass was explored by varying the ratio between the creak frequency and the structural frequency. Exploring the dynamic response as a function of the ratio provides qualitative characterization of the transmissibility of the disturbance to the system performance. The transient response of the system is calculated by numerically integrating Eqs. (2.16-2.17). The friction force is monitored at each time step to evaluate $\Delta\xi$. The different regimes of behavior are illustrated in Figure 2.4. The numerical values of the parameters are presented in Table 2.2. The creak response characterized by $\Delta\xi$ is shown on the top row and the corresponding structural response $\ddot{\xi}_3$ is shown on the second row. The first behavior, labeled banging, is self-explanatory. If the energy storage capacity is large, nothing will happen for long periods, and then suddenly,

a large-amplitude slip will take place. The second behavior is more frequent, and hence lower magnitude, slipping. The creak frequency is high enough such that the structural response has not died out noticeably before the next creak occurs. Finally, if the creaking frequency is close to the frequency of the structure, large motions result due to resonance.

The plot of the forcing function $\Delta\xi$ shows that the creak frequency is not constant due to the coupling between the structure and the disturbance. The coupling causes the magnitude and the frequency of the disturbance to deviate from the nominal values determined in Eq. (2.19) and (2.23). A range of creak frequencies may be present during the thermal transient of interest. The nominal magnitude given in Eq. (2.19) is an upper bound and the frequency given by Eq. (2.23) is a lower bound.

For a simple case where the system is weakly coupled ($\kappa_0 \ll 1$), the transmissibility H can be computed. The result is shown in Figure 2.5 for a given set of parameters. The friction parameter f_k is kept constant and the frequency is varied by adjusting α_r. The amplitude is largest at resonance, as expected. The smaller peaks are located at ω_c/ω equal to 1/2, 1/3, 1/4, and so forth. At these frequencies, the oscillations of the mass constructively add with the prior oscillations, amplifying the response.

TABLE 2.2 Numerical values of the parameters used in parametric study

Dimensionless Parameters	case 1 $\omega_c \ll \omega$	case 2 $\omega_c < \omega$	case 3 $\omega_c \approx \omega$
C_t	1×10^{-3}	1×10^{-3}	0.01
α_r	0.3	0.3	0
f_k	0.96	0.96	0.956
κ	1	5	1
κ_0	1	1	1
ω	1	1	1

Figure 2.4 Structural response at various creak frequencies
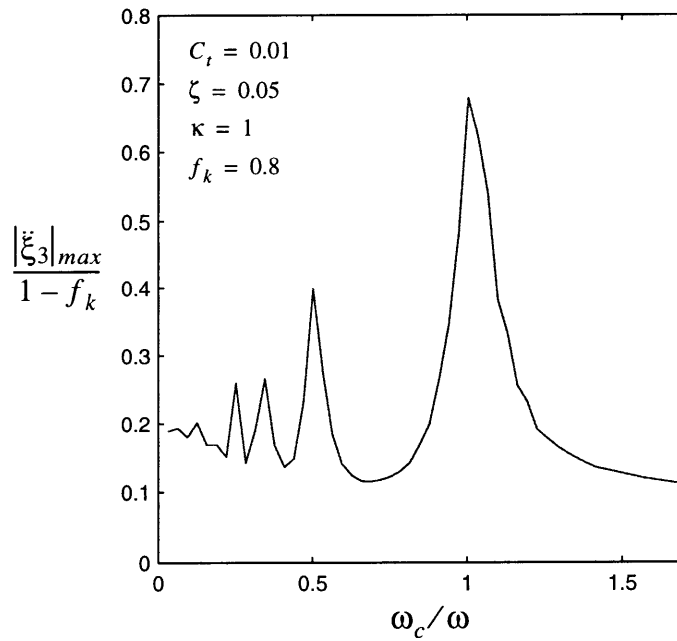
Figure 2.5 Transmissibility of static creak response to system response

In summary, a static creak element model was developed and the dynamic response of the attached system was investigated. The static assumption is valid for a creak element whose natural frequency is much higher than that of the structure, such as a flexible system with a stiff component. In the following section, inertia effects on the creak and the system response are studied.

2.3 Dynamic thermal creak analysis

In this section, the mass of the creak element is incorporated in the model. Analogous to Section 2.2 the creak response is first obtained. The structural response of the coupled two degrees of freedom system with thermal creak is then presented. The response is explored parametrically in the numerical results section and compared to that observed in the system with the static creak element.

2.3.1 Thermal creak response

The new governing equation of motion for the dynamic creak element is derived and non-dimensionalized. The creak disturbance is then characterized in terms of the profile, the magnitude, and the frequency of the energy release. The disturbance characteristics are compared to those obtained from the static creak model.

The equilibrium equation for the dynamic creak element without the attached mass is modified to include the inertia.

$$-m_1 \ddot{x}_1 - m_2 \ddot{x}_2 = F_1 + F_2 \tag{2.40}$$

As shown in Section 2.2.1, the constitutive and the compatibility relations in Eq. (2.2) and Eq. (2.5) are combined with Eq. (2.40), to write the equation of motion for the creak element.

$$(m_1 + m_2)\ddot{x}_1 + (k_1 + k_2)x_1 = k_1 x_1^t + k_2 x_2^t + m_2 \Delta \ddot{x} + k_2 \Delta x$$

$$\text{for } \left| k_1(x_1^t - x_1) - m_1 \ddot{x}_1 \right| < F_s \tag{2.41}$$

where $\Delta\ddot{x}$ is the relative acceleration extracted by taking the second time derivative of the compatibility relation, Eq. (2.5).

Similarly for the sliding system, the inertia are added to the equilibrium equations given in Eq. (2.7). The constitutive relations in Eq. (2.2) are then used to obtain the equations of motion for the pin and the slider.

$$m_1\ddot{x}_1 + k_1 x_1 = -F_f + k_1 x_1^t$$

$$m_2\ddot{x}_2 + k_2 x_2 = F_f + k_2 x_2^t$$

$$F_f = \begin{cases} F_k & \text{for } \dot{x}_1 - \dot{x}_2 > 0 \\ -F_k & \text{for } \dot{x}_1 - \dot{x}_2 < 0 \end{cases}$$

(2.42)

Nondimensionalized equations of motion

The equations of motion are now nondimensionalized to present them in a generalized form. The characteristic length x_1^* and the characteristic force F_s were introduced in Section 2.2.1 to define the dimensionless displacements and forces. The characteristic time $(1/\omega)$ is redefined such that

$$\tau = \omega t \qquad \omega^2 = \frac{k_1}{m_1}$$

(2.43)

Using the characteristic parameters, the dimensionless relative acceleration is defined.

$$\Delta\ddot{\xi} = \ddot{\xi}_1 - \ddot{\xi}_2$$

(2.44)

Parallel to the approach presented in the static analysis, the nondimensionalized equation of motion is acquired by rewriting Eq. (2.41) in terms of the dimensionless time using Eq. (2.35) and normalizing by x_1^*.

$$\ddot{\xi}_1 + \left(\frac{1+\kappa}{1+\mu}\right)\xi_1 = \left(\frac{1}{1+\mu}\right)[(1+\kappa\alpha_r)\xi_1^t + \mu\Delta\ddot{\xi} + \kappa\Delta\xi] \qquad \left|\xi_1^t - \xi_1 - \ddot{\xi}_1\right| < 1 \quad (2.45)$$

where μ is the mass ratio between the pin and the slider. The dimensionless parameters α_r and κ were defined in Section 2.2.1.

$$\mu = \frac{m_2}{m_1} \tag{2.46}$$

While the system is in the stuck mode, the relative acceleration is zero and the relative displacement remains at a constant value. The equation governing the relative motion during the sliding period, Eq. (2.42), is nondimensionalized using the same procedure to obtain Eq. (2.45).

$$\ddot{\xi}_1 + \xi_1 = -f_f + \xi_1^t$$

$$\ddot{\xi}_2 + \frac{\kappa}{\mu}\xi_2 = \frac{f_f}{\mu} + \frac{\kappa\alpha_r}{\mu}\xi_1^t \tag{2.47}$$

$$f_f = \begin{cases} f_k & \dot{\xi}_1 - \dot{\xi}_2 > 0 \\ -f_k & \dot{\xi}_1 - \dot{\xi}_2 < 0 \end{cases}$$

Recall that the friction parameter f_k was defined in Section 2.2.1. The friction force is a function of the relative velocity as indicated by Eq. (2.47). When the relative velocity is zero, the spring force and the inertia at that point must be greater than the static friction F_s for sliding motion to continue. Otherwise, the pin and the slider stick and move as one system.

Equations (2.45) and (2.47) are slightly more complex than the equations governing the static creak response, Eqs. (2.16) and (2.17). However, the dynamic and the static creak responses are qualitatively the same. The relative motion in the system occurs as a result of the nonlinear energy release via friction, which in turn acts as a disturbance to the system. Unlike the static case, a dynamic response of the creak element results due to the inertia. Therefore a dynamic creak element can be used to represent a structure with system level thermal creak.

Disturbance characterization

The characteristics of the disturbance introduced by a dynamic creak element are discussed in this section. The profile, the magnitude, and the frequency of the relative states $\Delta\ddot{\xi}$ and $\Delta\xi$ are determined.

To obtain the profile and the magnitude of the change in the relative displacement, the system of differential equations in Eq. (2.47) is first solved to compute ξ_1 and ξ_2 during sliding.

$$\xi_1 = A_1\cos(\tau - \tau_1) + B_1$$

$$\xi_2 = A_2\cos\left(\left(\frac{\kappa}{\mu}\right)^{1/2}(\tau - \tau_1)\right) + B_2 \tag{2.48}$$

For convenience, the times at which a slip initiates and terminates are denoted by τ_1 and τ_2, respectively. The displacements of ξ_1 and ξ_2 just prior to a slip need to be known to solve for the coefficients. For simplicity, the initial slip is investigated such that the velocity, the acceleration, and the relative displacement just prior to the initial slip are all zero.

$$\dot{\xi}_1(\tau_1) = \dot{\xi}_2(\tau_1) = 0$$

$$\ddot{\xi}_1(\tau_1) = \ddot{\xi}_2(\tau_1) = 0 \tag{2.49}$$

$$\Delta\xi(\tau_1) = 0$$

The coefficients B_1 and B_2 in Eq. (2.48) are then determined by substituting Eq. (2.48) and the subsequent derivatives into the differential equations in Eq. (2.47). Recall that the thermal displacement at the initial slip is equal to $(\xi_1^t)_{cr}$.

$$B_1 = (\xi_1^t)_{cr} - f_k$$

$$B_2 = \frac{f_k}{\kappa} + \alpha_r(\xi_1^t)_{cr} \tag{2.50}$$

The critical thermal displacement for the dynamic creak element is identical to the static case given by Eq. (2.20) because the system is assumed to be initially at rest and the

dynamics introduced by the thermoelastic response is neglected. The remaining coefficients are computed by first evaluating Eq. (2.48) at $\tau = \tau_1$ and substituting it into Eq. (2.45). The initial conditions in Eq. (2.49) and the critical thermal displacement given in Eq. (2.20) are then applied.

$$A_1 = 1 - f_k$$
$$A_2 = \frac{1}{\kappa}(1 - f_k) \tag{2.51}$$

Finally, the compatibility relation in Eq. (2.15) is used to arrive at the expression for the relative displacement during the sliding period.

$$\Delta\xi = A_1 \cos(\tau - \tau_1) + B_1 - \left(A_2 \cos\left(\left(\frac{\kappa}{\mu}\right)^{1/2}(\tau - \tau_1)\right) + B_2\right) \tag{2.52}$$

Equation (2.52) shows that $\Delta\xi$ is zero when $\tau = \tau_1$. Since the initial relative displacement is assumed to be zero, the profile of the relative displacement is smooth during the stick-slip transitions unlike the static case. As a result, the Fourier components of $\Delta\xi$ contains two frequencies, the natural frequency of the pin ($\omega_1 = \omega$) and the natural frequency of the slider ($\omega_2 = \omega(\kappa/\mu)^{1/2}$) as implied by Eq. (2.52).

The magnitude of change in $\Delta\xi$ during the stick-slip transition, A_c, can be computed as

$$A_c = \Delta\xi(\tau_2) - \Delta\xi(\tau_1) \tag{2.53}$$

To solve for the time at which the system sticks again, τ_2, the condition that the relative velocity is zero at $\tau = \tau_2$ is applied. The relative velocity is obtained by taking the time derivative of Eq. (2.52). The following transcendental equation results and thus τ_2 cannot be solved explicitly.

$$A_2\left(\frac{\kappa}{\mu}\right)^{1/2}\sin\left(\left(\frac{\kappa}{\mu}\right)^{1/2}(\tau_2 - \tau_1)\right) - A_1\sin(\tau_2 - \tau_1) = 0 \tag{2.54}$$

An exception exists for the case when $\kappa/\mu = 1$. Equation (2.54) reveals that the relative velocity is zero when $\tau_2 - \tau_1 = \pi$. The relative displacement at this point is at a maximum as suggested by Eq. (2.52). Using these conditions that $\kappa/\mu = 1$ and $\tau_2 - \tau_1 = \pi$ in Eq. (2.52), A_c is computed from Eq. (2.53).

$$A_c = 2(1 - f_k)\left(\frac{1}{\kappa} + 1\right) \qquad \frac{\kappa}{\mu} = 1 \qquad (2.55)$$

Because the inertia introduces a dynamic overshoot, A_c is greater than that introduced by the static creak element. For the special case where $\kappa/\mu = 1$ the magnitude of change in $\Delta\xi$ is twice the magnitude introduced by the static creak element [Eq. (2.19)]. This value of change in the relative displacement $\Delta\xi$ is an upper limit for the dynamic creak element with a given stiffness ratio, κ.

To characterize the relative acceleration, Eq. (2.52) is differentiated twice with respect to τ.

$$\Delta\ddot{\xi} = -A_1\cos(\tau - \tau_1) + A_2\frac{\kappa}{\mu}\cos\left(\left(\frac{\kappa}{\mu}\right)^{1/2}(\tau - \tau_1)\right) \qquad (2.56)$$

The relative acceleration is zero when the system is in the stuck mode. At the transition from the stuck to the sliding mode ($\tau = \tau_1$), the relative acceleration jumps to a nonzero value. This sudden jump in the acceleration is computed by evaluating Eq. (2.56) at $\tau = \tau_1$.

$$\Delta\ddot{\xi}(\tau_1) = (1 - f_k)\left(\frac{1}{\mu} + 1\right) \qquad (2.57)$$

Thus the acceleration has a step profile at the beginning of a slip due to the discontinuity in the friction force. Equation (2.56) indicates that another discontinuity in the relative acceleration exists at the end of the sliding cycle when the system becomes stuck again. The magnitude of the step function at this transition is dependent on τ_2, which cannot be solved explicitly. The maximum value of the jump, however, is attained when $\kappa/\mu = 1$.

Earlier in this section, τ_2 was determined for this special case, $\tau_2 - \tau_1 = \pi$. The magnitude of the second step function is then acquired by evaluating Eq. (2.56) at $\tau = \tau_2$. As expected, the magnitude of the second step function is the same as the magnitude of the first step at the beginning of the slip, $\left|\Delta \ddot{\xi}(\tau_1)\right| = \left|\Delta \ddot{\xi}(\tau_2)\right|$.

The following assumptions are made to determine the approximate creak frequency for the dynamic creak element. The thermoelastic response ξ_1^t is monotonic and $\xi_1^t > (\xi_1^t)_{cr}$ during the period of interest. The amplitude of the oscillations in the creak response during the stuck mode is negligible compared to magnitude of the total response, such that the dynamically-induced slips are avoided.

The approach developed in the static creak analysis to obtain the creak frequency is implemented. The creak period is equal to the time required for the reduced friction force, as a result of a slip, to build up to the static friction. The expression for the rate of change in the friction is obtained by taking the time derivative of the top equation in Eq. (2.47).

$$\int_0^{\omega P_c} \left| \ddot{\xi}_1 + \dot{\xi}_1 - \dot{\xi}_1^t \right| d\tau = 1 - f_f(\tau_2) \tag{2.58}$$

Based on the assumption that the oscillations in the creak response are small, $\dddot{\xi}_1$ is assumed to be negligible in Eq. (2.58). In the static case, the friction value at slip, $f_f(\tau_2)$, was f_k. In the dynamic creak model, the friction also reduces to f_k at the beginning of the slip and remains at f_k until the system sticks again at $\tau = \tau_2$. Because the dynamic overshoot causes more energy to be released, the friction value is actually lower than the kinetic friction when the system sticks again. The special case when $\kappa/\mu = 1$ is revisited to find this friction value.

Substituting Eq. (2.48) into Eq.(2.47), the friction value at the end of the sliding period is

$$f_f(\tau_2) = 2(1 - f_k) \tag{2.59}$$

The reduction at $\tau = \tau_2$ is the same amount as the initial drop in the friction force. Since the maximum change in the relative displacement occurs at $\kappa/\mu = 1$, this is the maximum reduction in the friction.

Thus, the expression for the creak frequency is

$$\int_0^{\omega P_c} \left| \dot{\xi}_1 - \dot{\xi}_1^t \right| d\tau = 2(1 - f_k) \tag{2.60}$$

Comparing Eq. (2.60) with Eq. (2.21), it can be seen that for the same thermoelastic response, the creak frequency of a dynamic creak element is half the creak frequency of the static creak element. The inertia causes more energy to be released per creak than the static case and thus the frequency of the release is reduced. This creak frequency for $\kappa/\mu = 1$ is a lower bound on the dynamic creak element. The upper bound is approached as the parameters approach the static case. A complex behavior results if additional slips occur due to the dynamic response of the creak element. These dynamically induced slips cause the creak frequency to vary with time even under a constant thermal loading. A similar behavior was seen when the structural response was coupled with the static creak response in Section 2.2.2.

As an example, the dynamic creak response is computed for an exponential thermoelastic response given in Eq. (2.25). The same numerical values of the dimensionless parameters provided in Table 2.1 are used to compare the results to those from the static creak model. The mass ratio μ is set to be one. The equations of motion, Eqs. (2.45) and (2.47), are numerically integrated to compute the displacements and the relative states. Figure 2.6 presents the displacements of the pin and the slider. The response is qualitatively similar to that seen in the static creak element [Figure 2.2]. The displacements of the pin and the slider follow the thermoelastic response in gross slips. These slips however are not step functions. In addition to the gross displacements, oscillatory motion appears. As seen in the static creak response, the initial slip occurs when $\xi_1^t = (\xi_1^t)_{cr}$.
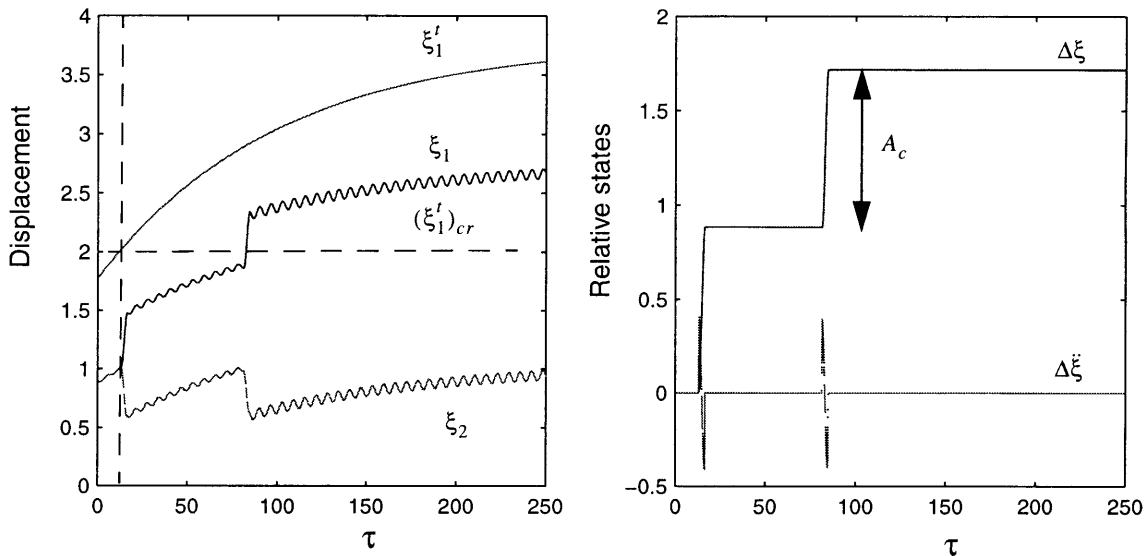
Figure 2.6 Displacements of dynamic creak element **Figure 2.7**   Relative acceleration in dynamic creak element

The relative motions in the creak element are plotted in Figure 2.7. The profile of the relative displacement $\Delta\xi$ is smooth during the stick-slip transitions. The acceleration, however, is discontinuous at the stick-slip transitions due to the discontinuity in the friction force. At the beginning of a slip, the accelerations of the pin and the slider instantaneously jump to new values. The sliding motion continues until the relative velocity is zero, at which point the system sticks together because the inertia and the spring forces cannot overcome the static friction. As a result, another discontinuity in the relative acceleration occurs. Thus two successive step forces, separated in time by $\tau_2 - \tau_1$, are imparted on the system during each slip.

As expected, the magnitude of the change in the relative displacement is twice as large as that in the static creak response, $A_c = 0.8$. The magnitude of the jump in the relative acceleration is 0.4 as suggested by Eq. (2.57). The figure shows that the magnitudes at each slip are approximately constant. The creak frequency however is a function of time as result of the exponential thermoelastic response. Note that a total of two slips occurred as opposed to four in the static creak model as shown in Figure 2.3. The number of slips are reduced in the dynamic creak model as implied by Eq. (2.60).

In summary, the disturbances introduced by the dynamic creak element were character-ized. The disturbances arise from the relative displacement and relative acceleration. Bounds on the profile, the magnitude and the frequencies of the change in the relative motion were determined. The frequency content of the relative displacement consists of the natural frequencies of the pin and that of the slider. The Fourier components of the rel-ative acceleration, however, contains all frequencies since step functions are introduced. These disturbances are transmitted to the surrounding structure, exciting all the modes in the system. The ensuing structural response of the attached mass is investigated in the fol-lowing section.

2.3.2 Structural response

The same approach presented in Section 2.2.2 is taken to derive the nondimensional equa-tions of motion for the fully coupled system shown in Figure 2.1. For the sake of comple-tion, damping is introduced to the creak element, where c_1 and c_2 are the damping coefficients for the pin and the slider, respectively. The equations of motion for the creak element and the attached mass are formulated from the equilibrium and the constitutive relations. The equations are then nondimensionalized by rewriting them in terms of the dimensionless time using Eq. (2.35) and normalizing them by x_1^* as demonstrated in Section 2.2.2.

$$
\begin{bmatrix} 1 + \mu & 0 \\ 0 & \mu_0 \end{bmatrix} \begin{bmatrix} \ddot{\xi}_1 \\ \ddot{\xi}_3 \end{bmatrix} + \begin{bmatrix} 2\zeta(1 + \gamma + \gamma_0) & -2\zeta\gamma_0 \\ -2\zeta\gamma_0 & 2\zeta\gamma_0 \end{bmatrix} \begin{bmatrix} \dot{\xi}_1 \\ \dot{\xi}_3 \end{bmatrix} + \begin{bmatrix} 1 + \kappa + \kappa_0 & -\kappa_0 \\ -\kappa_0 & \kappa_0 \end{bmatrix} \begin{bmatrix} \xi_1 \\ \xi_3 \end{bmatrix}
$$

$$
= \left(\begin{bmatrix} (1 + \kappa\alpha_r)\xi_1^t \\ 0 \end{bmatrix} + \begin{bmatrix} f_{nl} \\ 0 \end{bmatrix} \right)
$$

(2.61)

where

$$
f_{nl} = \mu\Delta\ddot{\xi} + \gamma\Delta\dot{\xi} + \kappa\Delta\xi
$$

(2.62)

As a result of the nondimensionalization, additional dimensionless parameters are introduced.

$$\mu_0 = \frac{M}{m_1} \qquad \gamma_0 = \frac{C}{c_1} \qquad \gamma = \frac{c_2}{c_1} \qquad \zeta = \frac{c_1}{2m_1\omega} \qquad (2.63)$$

The remaining dimensionless parameters were defined earlier in Section 2.2.1 and Section 2.3.1.

When the friction force exceeds the static friction, an additional degree of freedom is introduced because the pin and the slider are separated. The equations of motion for the separated system are written and nondimensionalized to arrive at the following system of equations.

$$\begin{bmatrix} 1 & 0 & 0 \\ 0 & \mu & 0 \\ 0 & 0 & \mu_0 \end{bmatrix} \begin{bmatrix} \ddot{\xi}_1 \\ \ddot{\xi}_2 \\ \ddot{\xi}_3 \end{bmatrix} + \begin{bmatrix} 2\zeta(1+\gamma+\gamma_0) & 0 & -2\zeta\gamma_0 \\ 0 & 2\zeta\gamma & 0 \\ -2\zeta\gamma_0 & 0 & -2\zeta\gamma_0 \end{bmatrix} \begin{bmatrix} \dot{\xi}_1 \\ \dot{\xi}_2 \\ \dot{\xi}_3 \end{bmatrix} + \begin{bmatrix} 1+\kappa_0 & 0 & -\kappa_0 \\ 0 & \kappa & 0 \\ -\kappa_0 & 0 & \kappa_0 \end{bmatrix} \begin{bmatrix} \xi_1 \\ \xi_2 \\ \xi_3 \end{bmatrix}$$

$$= \left(\begin{bmatrix} \xi_1^t \\ \kappa\alpha_r\xi_1^t \\ 0 \end{bmatrix} - \begin{bmatrix} f_f \\ f_f \\ 0 \end{bmatrix} \right) \qquad (2.64)$$

Equation (2.61) is the nondimensional equations of motion for the fully coupled two degrees of system with thermal creak. The displacement of the slider is an internal degree of freedom and the effective response is introduced via the relative states. Note that the mass, the damping, and the stiffness matrices in the equation of motion are identical to those of the two DOF linear system. The relative motion in the system is a nonlinear response and this nonlinearity in the system is introduced into the equation as a forcing function [Eq. (2.61)]. The response of the system strongly depends on the characteristics of the forcing function f_{nl}.

Again, as κ_0 approaches zero, the system response ξ_3 and the creak response ξ_1 become decoupled. As μ approaches zero the disturbance contribution from the relative acceleration is neglected. The relative magnitudes of the relative states depend on the system parameters.

Results

A range of behavior for the attached mass M was explored by varying the parameters. The thermal load is assumed to be a ramp load. The transient response of the system is calculated by numerically integrating Equations 2.61 and 2.64. The different regimes of behavior are illustrated in Figure 2.8 and the numerical values of the parameters are listed in Table 2.3. Recall that the characteristic time was defined differently for the dynamic creak element model. The creak frequency is varied relative to the frequency of the attached system defined as $\omega_0^2 = \kappa_0/\mu_0$. The disturbance characterized by f_{nl} is shown on the top row and the corresponding structural response $\ddot{\xi}_3$ is shown on the second row. The response contains multiple frequencies as the dynamics of the creak element are introduced. However, the behavior is qualitatively similar to the behavior exhibited in the static creak element analysis [Figure 2.4]. Both the forcing function and the structural response have similar trends as seen in Figure 2.4. As seen in the static case, the transmissibility of the thermal creak disturbance to the system performance is a strong function of the average creak frequency. Here, the creak frequency is time varying due to the inertia effects and the coupling between the structural response and the creak response.

In summary the equations of motion and the results indicate that the behaviors of the dynamic creak element and the static creak element are qualitatively similar. In both models, the energy is released via relative motions in the creak element and introduce step disturbances to the system. The results also show that the structural response is a strong function of the ratio of the creak frequency to the structural frequency.

TABLE 2.3 Numerical values of the parameters used in parametric study

Dimensionless Parameters	case 1 $\omega_c \ll \omega_0$	case 2 $\omega_c < \omega_0$	case 3 $\omega_c \approx \omega_0$
C_t	1×10^{-3}	8×10^{-3}	0.01
α_r	0	0	0
f_k	0.95	0.5	0.95
κ	1	10	1
μ	1	10	1
κ_0	1	1	1
μ_0	1	10	5
ω	1	1	1
ω_0	1	0.316	0.447

Figure 2.8 Structural response at various creak frequency

2.4 Example of creak analysis

The model developed earlier in this chapter is implemented to analyze thermal creak in a real structure. As an example, a proposed conceptual design of the Next Generation Space Telescope (NGST) is considered to investigate the possible thermal creak sources and the effects on the performance metric [Figure 2.9]. In this example study, thermal creak in the sunshield is analyzed. The sunshield is based on a deployable concept, where six inflatable petals form an enclosed shell [30]. A schematic diagram of the sunshield is shown in Figure 2.10. Each petal overlaps with the adjacent petals and create frictional interfaces. A transient temperature gradient across the thickness of the petal may develop due to the spacecraft reorientation during the operation. Such a gradient causes the petals to bend, assuming a linear temperature gradient [31]. The bending motion of the petal however is restrained by the sunshield because the sunshield as a whole resists the deformation in this radial mode. As a result, the stress in the petal builds up until the stress reaches a critical point where the static friction can be overcome at the overlap. At this point, the petal slips relative to the rest of the shield. This slip motion introduces a sudden change in the moment to the sunshield and thus vibrations of the structure follow. The creak response in the sunshield and the corresponding force transmitted to the structure is computed to analyze the effect on the performance metric.

The following approach is applied to obtain the NGST performance metric due to thermal creak in the sunshield. Based on the assumption that the creak response is decoupled from the structural response, the sunshield is first reduced to the simple thermal creak model presented in Section 2.3. The creak response is obtained in a dimensionless form due to lack of knowledge of friction parameters. By mapping the NGST system parameters to the dimensionless parameters in the model, the nondimensionalized equations of motion developed in Section 2.3.1 are used to obtain the creak response. The creak response is then scaled to an effective moment applied to the surrounding structure. The moment is applied to the structural dynamics model to compute the structural response and thus the performance metric.
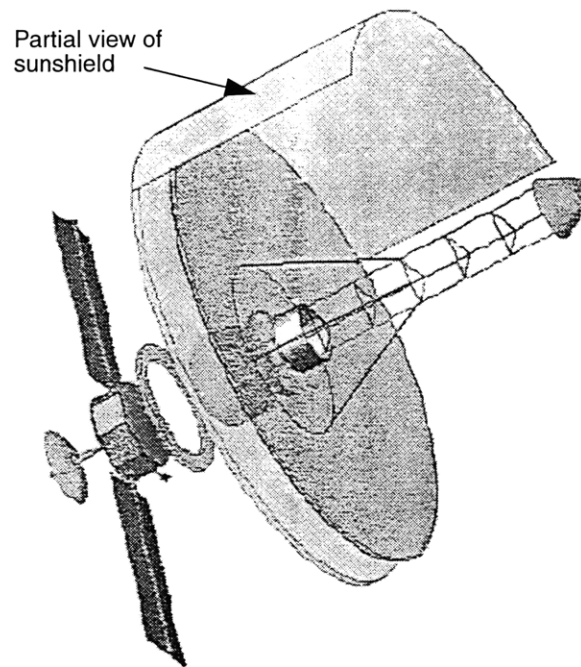
Figure 2.9   A conceptual design of NGST[30]
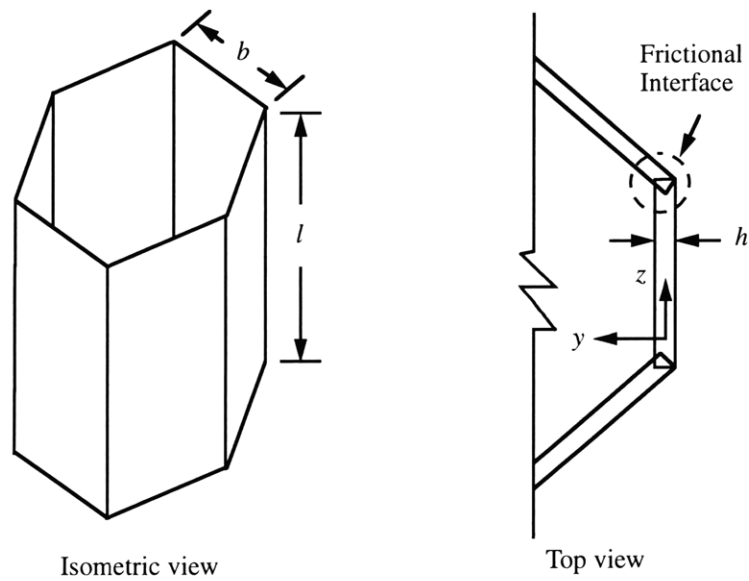
Figure 2.10   Schematic diagram of sunshield

2.4.1 Creak response

The petal undergoing thermal strain relative to the rest of the shield is modeled as a beam with modulus of elasticity, E, moment of inertia, I, mass per unit length m, and coefficient of thermal expansion α [Figure 2.10 and Figure 2.11]. The beam length, thickness, and
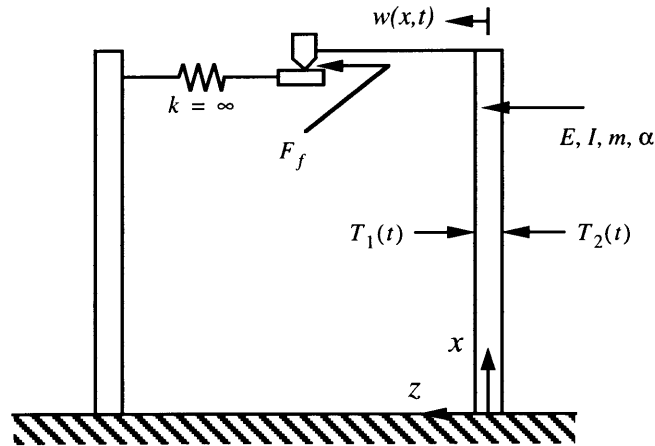
Figure 2.11 Mathematical model of sunshield

width are l, h, and b, respectively. The beam deflection in the z direction is denoted by w. The temperatures at the inner and the outer surfaces of the beam are $T_1(t)$ and $T_2(t)$, respectively. The petal is assumed to be cantilevered at the base to the primary mirror, and the creak response of the beam is assumed to be decoupled from the dynamics of the surrounding structure. The friction at the interface acts on the entire contact area, which is along the length of the beam. In the model, this friction force is reduced to an effective friction force, F_f, concentrated at the tip of the petal resisting the transverse motion. Note that the stiffness of the sunshield in the direction of the slip is very large compared to the bending stiffness of the beam and thus no motion is allowed when the petal is intact with the rest of the shield. Finally, the temperature gradient through the thickness of the petal is assumed to be a linear function of z.

$$T_z(z, t) = \Delta T_m(t)\frac{z}{h} + T_{avg}(t) \tag{2.65}$$

where

$$\Delta T_m = T_1 - T_2$$

$$T_{avg} = \frac{(T_1 + T_2)}{2}$$ (2.66)

Equation of motion

No motion is allowed when the beam is stuck with the rest of the shield. The equation of motion for the beam when sliding is written using the beam equation, followed by the geometric boundary conditions.

$$m\frac{\partial^2 w}{\partial t^2} + EI\frac{\partial^4 w}{\partial x^4} + \frac{\partial^2 M_T}{\partial x^2} = -F_f(t)\delta(x-l)$$ (2.67)

$$w(0, t) = 0$$

$$\frac{\partial w}{\partial x}(0, t) = 0$$ (2.68)

where M_T and F_f are the thermal moment and an effective friction force acting at the tip of the beam, respectively. The friction behavior is assumed to be Coulombic, where F_s and F_k represent the effective static and kinetic friction at the tip. The Kronecker delta function in Eq. (2.67) is defined as

$$\delta(x-l) = \begin{cases} 0 & x \neq l \\ 1 & x = l \end{cases}$$ (2.69)

The thermal moment is computed as follows [31].

$$M_T(t) = \int_{-h/2}^{h/2} bE\alpha T_z(z, t)z\,dz$$ (2.70)

Equation (2.70) is evaluated for the temperature function given in Eq. (2.65) to obtain the following expression for the thermal moment.

$$M_T(t) = \frac{EI}{h}\alpha\Delta T_m \tag{2.71}$$

To reduce to the model to the simple dynamic creak model developed in Section 2.3 the beam is reduced to an equivalent SDOF system using the Rayleigh-Ritz energy method. First, the beam deflection is approximated as a function of the first bending mode shape ϕ_1 and a generalized degree of freedom q.

$$w(x, t) = \phi_1(x)q(t) \tag{2.72}$$

where the assumed first bending modeshape of the beam is as follows.

$$\phi_1 = \frac{1}{2}\left[3\left(\frac{x}{l}\right)^2 - \left(\frac{x}{l}\right)^3\right] \tag{2.73}$$

Using this approximation, the kinetic and the potential energy of the system along with the work done by the system are written. These energy terms are then substituted into the Lagrange equation to yield

$$M\ddot{q} + Kq = Q \tag{2.74}$$

The generalized mass, stiffness, and force are computed as follows.

$$M = \int_0^l m(\phi_1)^2 dx$$
$$K = \int_0^l EI(\phi_1'')^2 dx \tag{2.75}$$
$$Q = -\int_0^l M_T\phi_1'' dx - F_f\int_0^l \phi_1\delta(x - l)dx$$

Evaluation of the integrals in Eq. (2.75) leads to the values of the mass, the stiffness, and the force.

$$M = 0.24ml$$

$$K = \frac{3EI}{l^3}$$

(2.76)

$$Q = -\frac{3}{2l}M_T - F_f$$

Here an effective thermal displacement q^t is introduced to rewrite the thermal moment as

$$M_T = -\frac{2EI}{l^2}q^t$$

(2.77)

where

$$q^t = \alpha(\Delta T_m)l_{eff}$$

$$l_{eff} = \frac{l^2}{2h}$$

(2.78)

Substituting Eq. (2.77) into the expression for the generalized force in Eq. (2.76), the equation of motion for the SDOF system now takes the form

$$M\ddot{q} + Kq = Kq^t - F_f$$

$$F_f = \begin{cases} F_k & \text{for } \dot{q} > 0 \\ -F_k & \text{for } \dot{q} < 0 \end{cases}$$

(2.79)

Nondimensionalization

The equation of motion is nondimensionalized by mapping the system parameters to those introduced in Section 2.3.1. Thus the characteristic displacement q^* and the inverse of the characteristic time $(1/\omega)$ are defined as

$$q^* = \frac{F_s}{K} \qquad \omega = \sqrt{\frac{K}{M}}$$

(2.80)

The characteristic force remains as F_s. Then the nondimensionlized displacements, forces, and time are

$$\xi_1 = \frac{q}{q^*} \qquad \xi_1^t = \frac{q^t}{q^*} \qquad f_f = \frac{F_f}{F_s} \qquad \tau = \omega t \tag{2.81}$$

The nondimensionalized parameters for this example study are

$$\alpha_r = 0 \qquad f_k = \frac{F_k}{F_s} \qquad \kappa = \infty \tag{2.82}$$

The motion of the petal is restrained when the effective friction at the tip is below the static friction. As a result, the tip displacement remains at a constant value when stuck.

$$\xi_1 = \Delta\xi \qquad \left|\xi_1 - \xi_1^t - \ddot{\xi}_1\right| < 1 \tag{2.83}$$

When the friction is overcome, the shield moves according to the following equation of motion.

$$\ddot{\xi}_1 + \xi_1 = \xi_1^t - f_f$$

$$f_f = \begin{cases} f_k & \dot{\xi}_1 > 0 \\ -f_k & \dot{\xi}_1 < 0 \end{cases} \tag{2.84}$$

Because the creak response is not coupled with the dynamic response of the system, the creak response can be computed separately from the structural response.

In Section 2.3.2, Eq.(2.61) showed that thermal creak in a MDOF system appears as a forcing function. The mass, damping, and the stiffness matrices remain unaffected by the nonlinearity in the system. Thus the equation of motion for the telescope is written as

$$M\ddot{q} + C\dot{q} + Kq = F_{nl} \tag{2.85}$$

where the mass, damping, and stiffness matrices of the telescope, denoted by M, C, and K, respectively, are extracted from the finite element model developed by Gutierrez [3232]. The vector q consists of the degrees of freedom in the system. Thermal creak is assumed

to be the only disturbance introduced in the system and this disturbance is represented by F_{nl}. The thermal forces and moments are neglected in Eq. (2.85) assuming that the dynamics introduced by the thermoelastic response is small.

The vector F_{nl} is a vector containing forces and moments due to thermal creak as seen in Eq. (2.61). This nonlinear forcing function is a function of the creak response applied at the petal tip. Because the sunshield was modeled separately from the spacecraft, the reaction force at the base of the petal needs to be applied. The reaction force is equal and opposite to the creak force applied at the tip of the petal.

The nonlinear force is first converted to an equivalent moment. The effective moment required to cause the same tip displacement is

$$\overline{M}_{nl} = (\xi_1^t - f_f)\frac{l}{q^*} \tag{2.86}$$

2.4.2 Numerical results

The performance metrics for the NGST telescope are computed by numerically integrating Eq. (2.85) and the results are presented in this section. The performance variables are differential pathlengths (DPL) and wavefront tilts (WFT) of the incoming lights as defined in [33]. These performance variables depend on the motions of the primary and the secondary mirror. The forces and the moments were first computed from Eq. (2.86). The transient dynamic response was then obtained via direct time integration of Eq. (2.85) to compute the performance metrics

The numerical values of the parameters are listed in Table 2.4. The natural frequency of the petal is assumed to be 0.1 Hz. The frequency of the lowest mode of the system is 0.5 Hz. Hence the dynamic creak element model is more appropriate because the natural frequency of the petal is on the order of the first natural frequency of the system.

Because the natural frequency of the petal is relatively low, the persistent creaking behavior seen in Figure 2.8 is unlikely to occur. Therefore, only the results for a single slip is

TABLE 2.4 NGST system parameters

Parameters	Values
ω [rad/sec]	0.628
l [m]	8
F_s [N]	0.125
f_k	0.5

considered. The thermal response of the petal as a function of time is not crucial in the analysis as long as $\xi_1^t \geq (\xi_1^t)_{cr}$. Due to the lack of knowledge of the friction parameters, the results are obtained in terms of the dimensionless parameters. Once the friction values are known, the response plots can be scaled accordingly.

Figure 2.12 shows the normalized forcing function that is applied to the petal tip, where $\overline{M}_{nl} = M_{nl}/(F_s l)$. There are two step functions due to the inertia effect as discussed in Section 2.3. The magnitude of the step is based on the value $f_k = 0.5$. The step size can be scaled accordingly for different values of f_k. The performance variables as a function of time are plotted in Figure 2.13 and Figure 2.14. The time response of the differential pathlength indicates that thermal creak in the sunshield introduces broadband disturbance
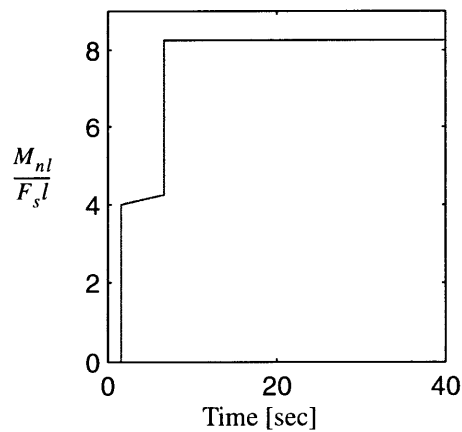
Figure 2.12 Dimensionless moment applied to NGST due to thermal creak
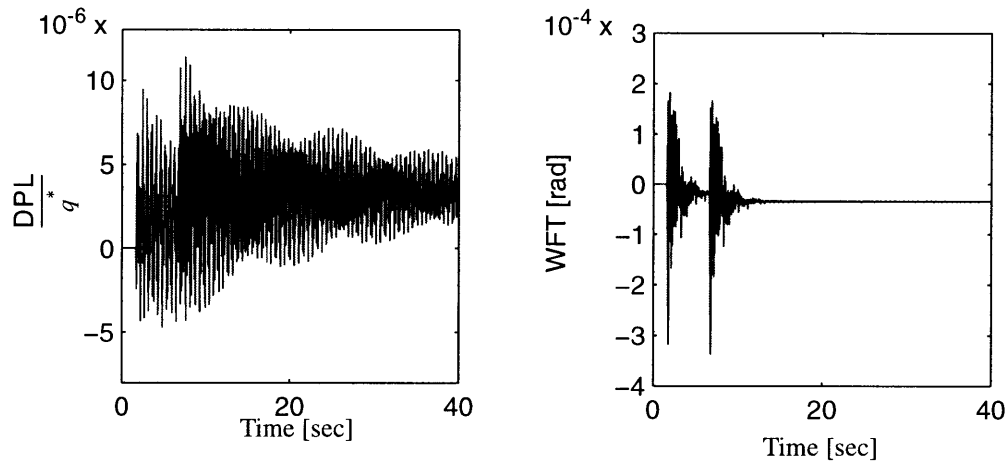
Figure 2.13   Differential pathlength in NGST due to thermal creak

Figure 2.14   Wavefront tilt in NGST due to thermal creak

to the telescope. Note that the DPL is sensitive to the low frequency vibrations and hence, takes a while to settle. On the other hand, the WFT is more sensitive to the high frequency vibrations in the system and thus settles rapidly.

2.5 Summary

A thermal creak model that captures the energy storage, energy release, and energy propagation mechanisms was developed. The nondimensional equation of motion revealed the key parameters that govern the creak response and the resulting dynamic response. The key parameters that dictate the creak behavior are the thermal strain mismatch parameter α_r and the dimensionless kinetic friction f_k. The thermal strain mismatch parameter determines the energy storage capacity of the creak element. The dimensionless kinetic friction determines the energy release capacity of the creak element. As expected, the creak frequency is a function of the energy input rate, the energy storage capacity and the energy release capacity. The bounds on the magnitude and the frequency of the energy release were determined.

The key parameters that govern the dynamic response are the system parameters κ_0 and μ_0, as well as the creak frequency. The equation of motion for the structural response also

showed that the relative motion in the creak element acts as a disturbance to the attached system. The profile of the energy release contains a step function and thus the relative motion excites all the modes in the system. Because the forcing function exciting the system is an internal force, the creak response is coupled with the system response. For a weakly coupled system, the creak response can be determined first and then input to the structural dynamics model as a disturbance. For complex structures, the relative motion can be measured experimentally to approximate the nonlinear forcing function f_{nl}.

These key parameters provide an insight into possible thermal creak mitigation strategies. The energy input rate, energy storage capacity, and energy release capacity can be altered to reduce the possibility of thermal creak. For instance, achieving the thermal mismatch parameter α_r and the friction parameter f_k close to unity is desirable. A thermal control system can be designed to maintain a uniform temperature distribution and allow a small fluctuation during the thermal transients to achieve $\alpha_r \approx 1$. Use of appropriate lubricants in nonlinear joints to modify f_k is another possible mitigation strategy.

The example analysis of NGST demonstrated that the system response to thermal creak is specific to the structure and the design. As the model indicated the response depends on the load path from the creak source to the performance metric, the energy parameters of the creak element and the thermal input. However, the simple creak model is generic enough that it can be applied to these real structures to analyze the effects of thermal creak on the structural performance metric.

Chapter 3

EXPERIMENT DESCRIPTION

The experimental setup and the test articles are described in this chapter. The details of the joint characterization experiment are first presented, followed by the dynamics experiment descriptions.

3.1 Joint characterization

In this section, the joint characterization experiment is described. The objectives of the joint characterization experiment are 1) to demonstrate thermal creak, 2) understand the physical mechanism of creak, 3) measure the micro-motions of a typical joint due to thermal creak, and 4) assess the analytical model. The hardware description is first presented, followed by the instrumentation and the test procedures.

3.1.1 Test article

The joint characterization test article is a beam composed of a zero-CTE graphite/epoxy bar sandwiched between two aluminum bars [Figure 3.1]. Each bar is 2.03 cm (8 in) long and 2.54 cm (1 in) wide. The thickness of the aluminum is 0.318 cm (0.125 in). The thickness of the composite is 0.102 cm (0.04 in). The composite specimen was cut from a layup manufactured by Dunn [34]. The material properties of the aluminum and the composite are shown in Table 3.1. The bars are held together by two steel bolts located near the ends of the beam. The bolts are loosely fit to allow relative motion between the com-

ponents of the beam. Steel washers are placed between the bars to allow spacing between the bars.The center of the holes are located 2.54 cm (1 in) from the edge. The bolt and the hole diameters are 0.635 cm (0.25 in) and 0.533 cm (0.21 in), respectively, and thus the clearance is 0.1 cm (0.04 in).

The thermally-induced stresses and the critical displacement for the beam are computed based on the equilibrium, constitutive, and compatibility relations for the system. Details of the model of the slip joint are presented in the next chapter. The CTE mismatch

Strip heater

Aluminum

0-CTE Gr/Ep

Washer
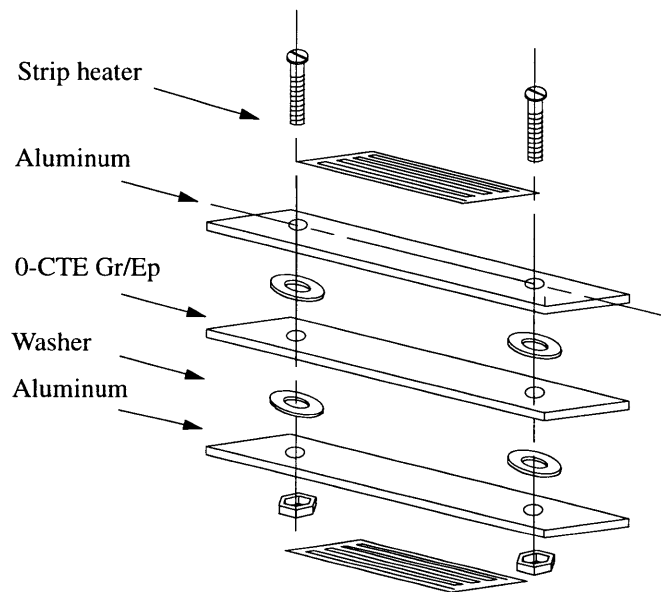
Aluminum

Figure 3.1 Exploded view of creak element test article

TABLE 3.1 Material properties of the beam

	Aluminum	**Composite**
E [N/m^2]	69×10^9	92×10^9
α [°C^{-1}]	23.6×10^{-6}	$< 0.2 \times 10^{-6}$
ρ [kg/m^3]	2700	1716
c_p [J/kg-K]	962	1123
k_x [W/m-K]	200	0.7
k_y [W/m-K]	200	0.5

between the components causes the composite and the aluminum to experience internal loads of -23.08 N/°C and 46.18 N/°C, respectively, where a positive value indicates tension. The reference temperature is the initial temperature of the beam assuming that no initial stress exists in the components.

The critical temperature at which the initial slip occurs is approximated as a linear function of the applied torque T_A in the model and is discussed in Section 4.1.1

$$(\Delta T)_{cr} = cT_A \tag{3.1}$$

where the constant is

$$c = 2.4 \frac{°C}{Nm} \tag{3.2}$$

3.1.2 Test environment

The thermal and the mechanical loading conditions are described in this section. The heating device used to apply thermal load, the mounting details, and the disturbance isolation issues are discussed.

Thermal load

Omegalux Kapton insulated flexible heaters model KHLV 105/5-P were bonded to the aluminum bars to apply heat to the beam [Figure 3.1]. The heaters were bonded via pressure sensitive adhesive on the backing of the strips. The heaters were bonded onto the outer surface of the beam for symmetric heating of the beam. The strip heater is 12.7 cm (5 in) long, 2.54 cm (1 in) wide, and 0.394 cm (0.010 inches) thick. The heat output of the strip is controlled by varying the applied voltage from 0-28 V. The corresponding heat output range is 0-25 W per heater. A voltage supply (NJE Corporation model RB 18-3) was used. When the voltage supply is turned on, a step heat load is applied to the beam. Because the aluminum bars are very conductive and thin, the gradient through the thickness is negligible. For the cooling part of the cycle, the heaters are turned off and the beam is allowed to cool via natural convection. The laboratory thermal environment is

fairly controlled such that the convective heat transfer coefficient and the ambient temperature do not vary significantly on different test days. The ambient temperature ranged from $22\,^{\circ}C$-$25\,^{\circ}C$. As a result, the thermal response of the joints are fairly repeatable.

Mounting and disturbance isolation

To isolate the test article from external disturbances, the joint was mounted on a Newport RS 4000 optics table [Figure 3.2]. The optics table provided isolation from floor disturbances. No other activities on the optics table were performed during the test runs. To simplify the experiment, the left end of the beam was clamped to an aluminum support to isolate the location of the slip to the right end of the beam. The normal load applied at the right end was varied by varying the torque applied to the bolt.

High torque   Variable torque
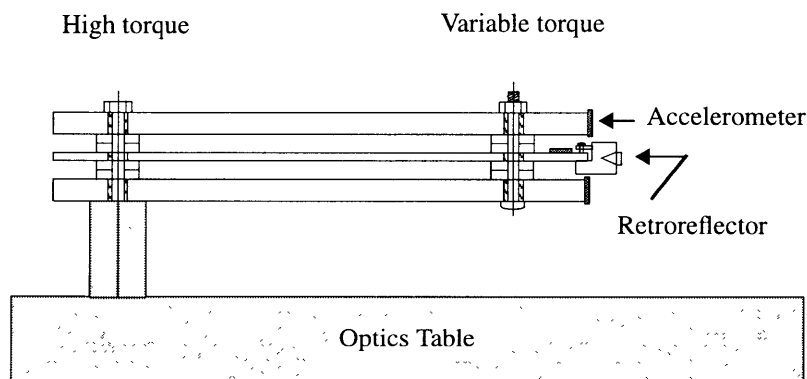
Figure 3.2 Side view of joint mounting setup

3.1.3 Instrumentation and setup

The details on the sensor specifications, mounting procedure, and locations are first provided. The data acquisition system and the signal conditioners are then described.

Sensors

The slip joint was equipped with the following sensors:1) thermocouples to measure the thermal state of the joint, 2) laser interferometer to measure axial displacements in the joint, and 3) accelerometers to measure thermal creak induced vibrations. Temperature

measurement of the slip joint was taken by Omega K type thermocouples. An Axiom 2/20 laser was used in the interferometer along with a Zygo polarization beam splitter and a Zygo 7080 detector. Endevco 2222C piezoelectric accelerometers were used. The specifications are listed in Table 3.2. The sensitivity value is approximately 100mV/g. Such high bandwidth accelerometers were chosen to detect and measure the vibrations since the slips in the joint occur in the longitudinal direction. Accelerometers are more suitable for such high frequency vibrations because the acceleration provides a stronger signal than the displacement due to the amplification from the frequency.

The thermocouples were attached onto the surface of the bars via thin aluminum tape. The thermocouples were placed at various locations on the joint to characterize the thermal response. The approximate locations are shown in Figure 3.3 as indicated by the dark dots. Only one thermocouple was active (signal fed to the acquisition system) during a test due to the limited channel availability. The location of the active thermocouple varied from test to test to obtain a survey of the temperature distribution. Based on the assump-

TABLE 3.2 Accelerometer specification

Model number	Endevco 2222C
Bandwidth [Hz]	5-8000
Resonant frequency [kHz]	32
Operating temperatures [$^\circ$C]	-73 to 177
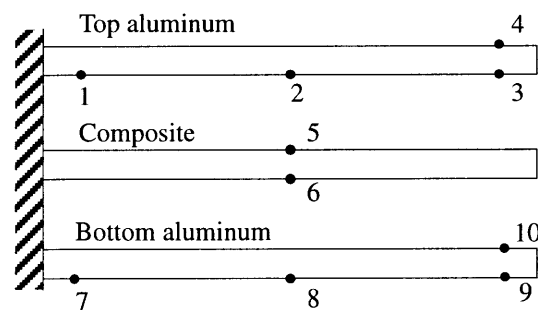
Figure 3.3 Thermocouple locations on the slip joint

tion that the thermal response is fairly repesatable, many runs of temperature measurement were taken at each location to obtain an average temperature distribution in the specimen.

The interferometer for this experiment was limited to one channel. Thus, the displacement history of only one bar was measured during a test run. Many test runs at a specified torque were taken to obtain the average response of the individual components. The average response of each bar was then plotted to view the response of all the components simultaneously at a specified torque.

A schematic diagram of the interferometer layout is shown in Figure 3.4. A beam from the laser passes through the beam splitter and two beams result, a reference beam and a measurement beam. The reference beam and the measurement beam are directed to the corresponding retroreflectors. The retroreflector for the reference beam is fixed and the retroreflector for the measurement beam is mounted on the specimen. The beams return to the detector and combine to create an interference. The retroreflector for the measurement beam was clamped on to the edge of the bar to measure the axial motion of the bar of interest [Figure 3.2]. The bandwidth and the sensitivity of the displacement sensor are limited by the data acquisition system and will be discussed in the next section.

One accelerometer was bonded onto each bar via cyanoacrylate adhesive. On the aluminum bars, the accelerometers were placed onto the edge face to measure the longitudinal
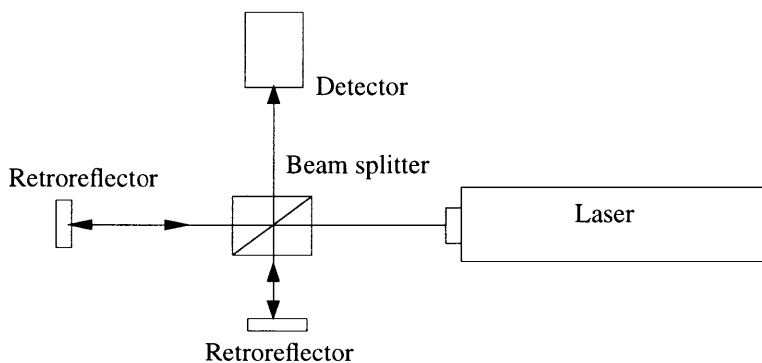
Figure 3.4 Interferometer layout

motion [Figure 3.2]. The accelerometer on the composite was mounted to measure the acceleration in the transverse direction because the composite was too thin [Figure 3.2]. The accelerometer on the composite, however, can still detect longitudinal vibrations due to the poisson effect. All three accelerometers were active during the test runs.

Signal conditioning and data acquisition

An Omega model DP-14 thermocouple reader was used to acquire data from the thermocouples and to output data to a laptop computer for storage. The output rate of the thermocouple reader was approximately 10 Hz. Because the thermal state changes relatively slowly, this sampling frequency was sufficiently high.

For the displacement measurements, the Axiom 2/20 Position Digital to Analog Converter (DAC), with a National Instruments Labview software interface, was used to for signal conditioning and acquisition of data. The Axiom DAC first converts the digital output of the laser measurement to an analog signal. The calibration of the converter was set at either 2.048 μm/V or 32.76 μm/V depending on the maximum displacement anticipated in the test runs. The analog signal is then acquired by Labview. The maximum sampling frequency imposed by Labview was approximately 10Hz for the duration of the selected data acquisition period. Thus the details of a slip event cannot be captured, but the displacement history is measured for the entire test run period.

Endevco 2721 charge amplifiers provided signal conditioning for the accelerometers. A Tektronix 2630 Fourier Analyzer was used in conjunction with a personal computer to acquire and process the signals from the accelerometers. The analysis bandwidth can be varied from 5 Hz up to 20 kHz for either DC or AC coupling. The sampling rate was 2.56 times the selected bandwidth. The analyzer also uses an anti-aliasing filter that guarantees alias protection for the entire 20kHz range [35]. Instead of recording the entire data throughout the thermal cycle, a triggering feature was employed such that data were recorded only when events similar to thermal creak were detected. The analyzer allows a trigger to be set on one of the signals obtained. The signals from the accelerometers are

continually stored in a buffer and overwritten until the trigger signal exceeds a preset value. At this point, the data from all the channels after the trigger point as well as prior to the trigger point are displayed on the monitor. The user then has the option to save or discard the displayed data. The time frame of an event data acquired by the analyzer depends on the sampling rate and the number of data points chosen.

3.1.4 Test procedures

At each test run, the heater was on for 15 minutes and the joint was allowed to cool down for 15 minutes. The heat input was set at approximately 7.5 W per heater. The heat input was sufficient to induce a slip at all normal load levels and to allow many slips. Initial stress was relieved by disassembling the joint and cooling it to room temperature at the end of every run. The normal force was controlled by the torque applied to tighten the bolt.

Three runs per bar at six torque settings were completed, leading to a total of 54 runs. The torque varied from 5 in-lb to 30 in-lb in increments of 5 in-lb. Three temperature measurements at each sensor location were taken [Figure 3.3]. No specific sequence of data gathering was implemented. The torque level, the location of the retroreflector, and the thermocouple location were chosen randomly until the entire test matrix was filled. Temperature measurements at the various locations were taken in the earlier test runs. In the later test runs, the thermocouple was used for monitoring the thermal state.

At each run, one displacement measurement and one temperature measurement were acquired for the entire thermal cycle period. Three accelerometers were active throughout the entire cycle. A trigger was set on one of the signals from the accelerometers. For acquisition of the accelerometer signal, the bandwidth of the analyzer was set at the maximum level, 20kHz, and the resulting sampling rate was 51.2kHz. The number of data points were 4096 points, the maximum allowable, and thus 80 milliseconds of data were acquired. The highest bandwidth level was selected because high frequency longitudinal vibrations due to thermal creak were anticipated. The threshold for the trigger was set

barely above the noise level measured by the accelerometers. Ten percent and ninety percent of the acquired data were pre-trigger and post-trigger data, respectively. The results are presented in Chapter 4.

3.2 Dynamics experiment

This section describes the thermal creak induced dynamics experiment performed on a representative space truss structure. The objectives of the dynamics experiment are 1) to demonstrate thermal creak, 2) measure the global motions of a typical deployable truss due to thermal creak, 3) characterize the transmissibility of the structure subjected to creak and 4) to assess the analytical model. The test article, the environmental testing facilities, and the instrumentation are described.

3.2.1 Test article

The thermal creak dynamics experiment test article is a deployable section of the Middeck 0-gravity Dynamics Experiment (MODE) Structural Test Article (STA). The truss flew in a space shuttle during STS-48 mission in 1991 and STS-62 in 1994 for experiments investigating nonlinearity and zero-gravity effects on the truss dynamics [15, 36]. A detailed description of the hardware is given in [36]. In this section, a general description of the truss is presented along with the details of the truss relevant to the thermal creak experiment.

The deployable truss consists of four bays with cable diagonals. The dimensions of the fully deployed configuration is 0.81 m x 0.2 m x 0.2 m. A partially deployed truss is shown in Figure 3.5. The longeron consists of solid Lexan rods (Lexan series 500), an aluminum knee joint at the midpoint, and aluminum hinge joints at the ends. The batten frame is constructed of solid Lexan rods with aluminum fittings at ends. The aluminum used in the truss is of type 6061. The diagonals are stainless steel cables (type 304) that are prestressed such that the nominal tension in the diagonals is 111 N (25 lbs) at deployed configuration. Such a tension leads the longerons to be preloaded at approximately 125 N

(28 lbs), which is approximately 50% of the longeron buckling load. The preload in one
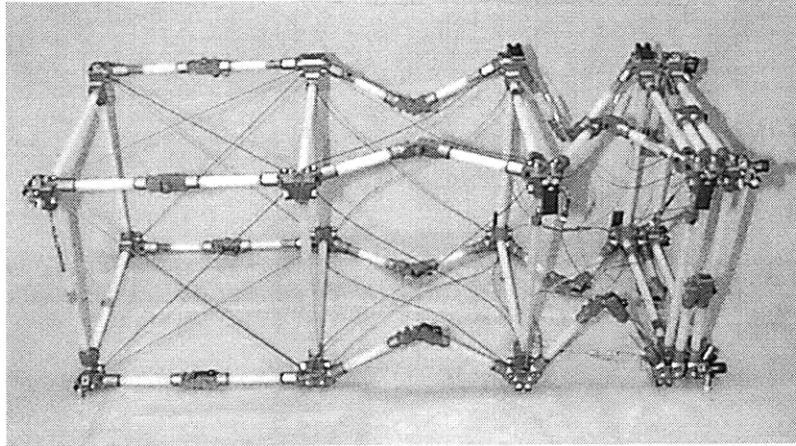
Figure 3.5 Partially deployed MODE truss

of the bays can be adjusted via a mechanism that can vary the cable tension. The tension can be set at 2.2N (0.5 lb), 35.6 N (8 lbs), or 111 N (25 lbs).

Several types of joints exist in the truss: 1) knee joint 2) pin-clevis joint and 3) batten corner fitting. The knee and the pin-clevis joints hinge to allow the longerons to fold and deploy. A latch type mechanism is employed in the knee joint assembly as shown in Figure 3.6. Once the knee joint is locked in a deployed position, the release lever and the latch creates a frictional interface. The batten frame remains rigid, as the struts are epoxied to the corner fittings. The longerons interface with the fittings via a pin-clevis joint, which can rotate in one direction [Figure 3.7]. Depending on the clearance in the hole for the pin, motion of the joint in axial and transverse directions relative to the batten fitting is also possible. The batten fitting houses the termination point of the diagonal cable. Each end point of the cable is a ball that rests in a spherical receptacle inside the batten fitting, as illustrated in Figure 3.8. Thus, another frictional interface exists between the ball and the receptacle. Under appropriate thermal loading conditions, these frictional interfaces may be sources of thermal creak.
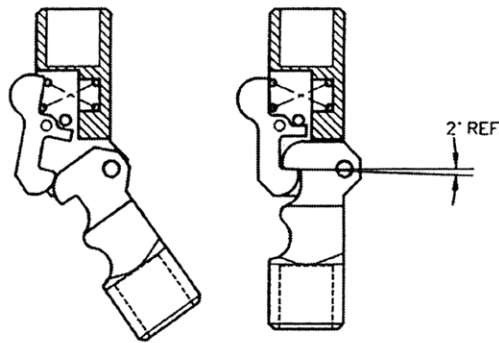
Figure 3.6 Knee joint assembly
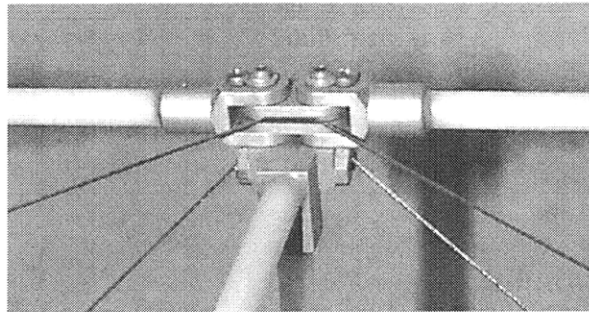
Figure 3.7 Pin-clevis joint
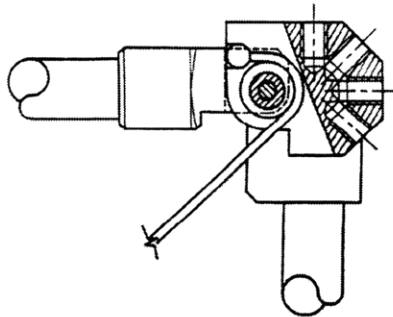
Figure 3.8 Cable termination point

The material properties and the dimensions of the truss elements are listed in [36]. The coefficients of thermal expansion (CTE) are listed in Table 3.3. Under uniform thermal loading, the CTE mismatch in this statically indeterminate structure will induce thermal

stresses in the truss elements. The stresses are computed based on the equilibrium, constitutive, and compatibility relations for the system. Details on the static model of the truss are presented in the next chapter. Internal forces of -2.1 N/$°$C, -1.7 N/$°$C, and 1.4 N/$°$C are developed in the longeron, batten, and the diagonal, respectively, where a positive force indicates tension. Consequently, the preload in the structure decreases with the decreasing temperature until the cable slackens at $\Delta T = -80°$C, assuming that the cable tension is initially set at 111 N (25 lbs).

TABLE 3.3   Coefficients of thermal expansion of components in MODE truss

Material	CTE
Aluminum 6061	23.6e-6 $°$C^{-1}
Lexan	62.5e-6$°$C^{-1}
Stainless Steel	14.5e-6$°$C^{-1}

3.2.2 Test environment

Two types of environmental chambers were used to apply thermal loads to the MODE truss: a convection thermal chamber and a radiative thermal vacuum chamber. The physical descriptions of the chamber and the heat transfer mechanisms are described in this section.

Convection chamber

The convection thermal chamber at Payload Systems, Inc. in Cambridge MA was used for a series of tests. The dimension of the chamber is approximately 4ft x 4ft x 4ft. The ambient air temperature in the chamber is controlled by heating and cooling of incoming air. Fans in the chamber provide a good air circulation, leading to uniform thermal loading of the specimen in the chamber. The temperature of the ambient air can be set by the user. The rates of heating and cooling of the ambient air were set at the maximum rates. The rates are approximately 4$°$C/min (7.2 $°$F/min), and -1.7$°$C/min (3.1 $°$F/min) for heating and cooling, respectively. Once the ambient air reaches the target temperature, the air

temperature is maintained at that temperature via continual switch between pulses of hot and cold air. Such control requires the pumps and other internal mechanical devices to be continually switched between on and off states, possibly introducing acoustic disturbances and electrical noise. The fans and the resulting turbulent air are other possible sources of undesirable disturbances. Isolation and characterization of these disturbances are addressed in Section 3.2.4.

Radiative vacuum chamber

Another set of tests was conducted at MIT Lincoln Laboratory in Lexington, MA using a thermal vacuum chamber. The length and the diameter of the chamber are approximately five and four feet, respectively. The chamber is a thin walled shroud that acts like a black-body heat source or sink. The shroud temperature is controlled by passing liquid nitrogen or nitrogen gas through tubes that are attached to the outer surface of the shroud. Unlike the convection chamber, the shroud temperature cannot remain at a specified temperature other than that of the liquid nitrogen due to absence of a controller. Changing between the cooling and the heating modes requires manual switching of the valves through which the fluid flows. Due to this chamber limitation, a shroud temperature profile was chosen carefully such that the thermal response of the test article is within a reasonable range. This temperature range for the MODE truss is determined to be $-30°C$ to $50°C$. Section 3.2.4 discusses how the bounds were obtained.

A simple method is employed to achieve the desirable temperature range for the truss. The shroud is cooled until the bottom section of the shroud reaches the liquid nitrogen temperature. At this point, hot gas is released to bring the shroud back to a room temperature or above. Figure 3.9 shows a typical temperature history of the shroud. The bottom section cools first as the nitrogen enters from the bottom. This section of the shroud attains the liquid nitrogen temperature ($-170 °C$), from room temperature in approximately seven minutes. The top part of the shroud reaches $T=-128 °C$ during that time, creating a gradient of approximately $40 °C$. The average shroud temperature as a function of time is computed from the data.

$$T_{av}(t) = \frac{1}{t}\int_0^t T(\tau)d\tau \tag{3.3}$$

where $T(t)$ is the average of the top and the bottom shroud temperatures. The plot indicates that this pulse of cooling produces a time-average temperature of approximately $-30°C$. This time-average shroud temperature indicates that a step-like thermal load is applied to the structure, similar to that encountered in space environment during the orbital day/night transition. However, the heating of the structure is extremely non-uniform. The gradient in the shroud, geometric effects such as self-shadowing, and dissimilar emissivity values between different surfaces all contribute to differential heating of the structure.
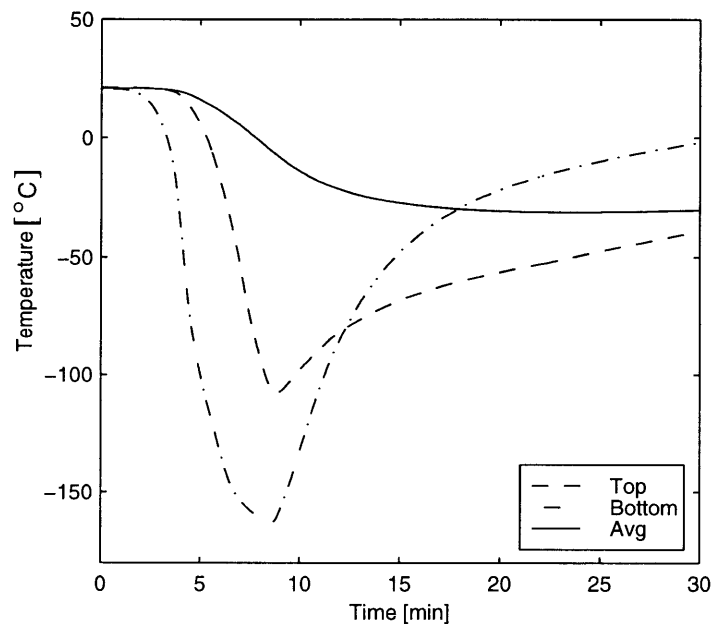
Figure 3.9 Radiative thermal chamber temperature

Some tests were conducted using cold plates to apply a controlled thermal load to the structure. Cold plates were placed in the shroud and the truss suspended above the cold plates. The truss was then covered with multi-layer insulators (MLI) such that it was isolated from all surfaces except the cold plates.

Suspension system and disturbance isolation

Disturbances in the chamber affected the truss mounting scheme as well as the data acquisition settings. To avoid transmissions of any high frequency vibrations of the chamber walls to the structure, the MODE truss was suspended in both the convection and the radiation chambers using soft springs whose natural frequency was approximately two Hertz. In the convection chamber, the MODE truss was suspended directly from a thick foam board on the chamber ceiling via soft springs. The suspension points are shown in Figure 3.10. The turbulent air in the convection chamber excited low frequency bounce and sway modes of the suspension system at approximately two hertz. In the thermal vacuum chamber, the truss was suspended in the center of the chamber via aluminum cables and the two hertz springs. Absence of air in the chamber eliminated any external excitation of low frequency suspension modes. In addition, the absence of air eliminated any acoustic disturbance. The pressure in the chamber was maintained at 0.1 torr or lower during tests. The sensor wires were slackened to eliminate undesirable load paths and incidental contact with structure. Acoustic excitation of structure due to noisy pumps, compressors, and other mechanical devices was a concern in the convection thermal chamber. In most tests, both in the convection and radiation chambers, one C accelerome-
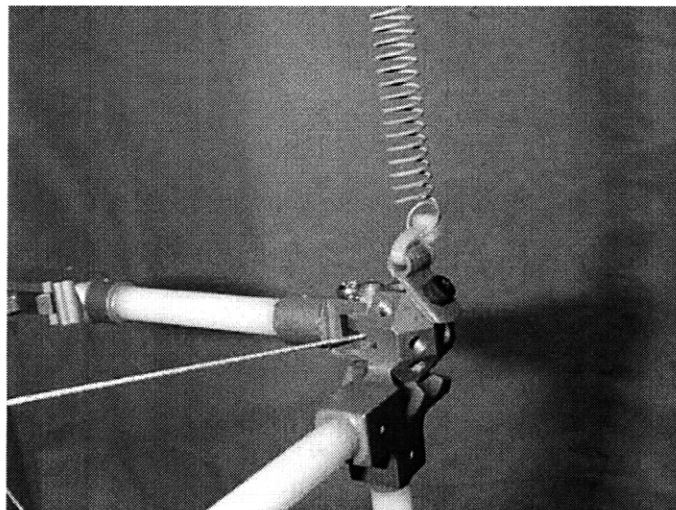
Figure 3.10 Suspension points

ter was attached to the chamber ceiling wall near one of the suspension springs and another C accelerometer on the truss near the other end of the suspension spring. This pair of accelerometers provided means to detect any acoustic events on the walls as well as to monitor the transmission of the chamber wall vibrations to the structure. A thorough discussion on measures taken to identify and isolate thermal creak is presented in [37].

3.2.3 Instrumentation and setup

The sensors and the data acquisition system are described in this section. A discussion on the mounting procedure and disturbance isolation follows.

Sensors

The following sensors were implemented in the experiment:1) thermocouples to measure the thermal loading, 2) strain gages to monitor the preload in the truss, and 3) accelerometers to measure vibrations induced by thermal creak and the noise level in the chamber. Type K thermocouples from Omega were used for measurements of surface temperature of the truss, the ambient air temperature in the convection chamber, and the shroud temperature in the vacuum chamber. The strain gages were Measurements Group EA-13 series and specifications are provided in Ref. [36]. Strain gages may not have enough sensitivity to detect small vibrations due to thermal creak. Hence, they were primarily used for sensing the change in the preload in the structure.

Two types of accelerometers were used: 1) Endevco 7265-HS piezoresistive accelerometers (denoted as accelerometer type A) and 2) Endevco 2222C piezoelectric accelerometers (denoted as accelerometer type C). Accelerometers of type C were also used in the joint characterization experiment and were discussed in Section 3.1.3. The specifications for accelerometer A are provided in Table 3.4. See Table 3.2 for specifications on C accelerometers. As indicated by the specifications, these high bandwidth accelerometers are suitable for detection and measurements of thermal creak events. The sensitivity values vary slightly among the A accelerometers and the strain gages. The sensitivity values are listed in Ref. [36].

TABLE 3.4 Accelerometer specifications

Model number	Endevco 7265-HS
Bandwidth [Hz]	0-500Hz
Resonant fre-quency [kHz]	1.4
Operating temera-tures	-18 to 66 C (op.) -54 to 85 C (non-op)

The thermocouples were attached onto the surface of interest via thin aluminum tape in the convection tests. For ambient air temperature measurement, the thermocouple was suspended off of a chamber wall. Cyanoacrylate adhesive was used for bonding the thermocouples to the structure in the thermal vacuum tests. The thermocouple locations varied from tests to tests and will be shown in the results section.

One of the faces of the adjustable preload bay were already instrumented with strain gages from a previous MODE flight experiment. Four strain gages were mounted on each member. Two strain gages were oriented to measure strain in the longitudinal and transverse directions. The other pair was placed on the other side of the member. The strain gages were wired as a full bridge circuit to 1) take out bending of the member, 2) to take out thermally induced strain in the strain gage and 3) to take out thermal strain in the member.

Accelerometers A were also mounted on the truss from the previous MODE experiment. Details on the mounting procedure of these sensors are in Ref. [36]. Accelerometers of type C were mounted on the truss via bonding wax for convection tests and cyanoacrylate adhesive for thermal vacuum tests. Not all A accelerometers were active (i.e. signals fed to the analyzer) during the tests. Locations of active accelerometers varied from tests to tests and will be shown in the results section. Both types of accelerometers were used in the convection tests, but only type C accelerometers were used for the tests conducted in the vacuum chamber due to a physical constraint imposed by the vacuum chamber. The total number of accelerometers used during a test varied due to the limited number of channels available in the data acquisition system. The number of accelerometers used in each test are provided in Table 3.5.

Signal conditioning and data acquisition

An Omega model DP25-K-A-DSS thermocouple reader was used during the convection tests. The unit acquired the data from the thermocouples and output data from one channel onto its own display. The channels were switched periodically to read off all the temperatures. The time and the temperatures were then written down. An HP 3852A Data Acquisition/Control Unit with National Instruments Labview software interface was used to acquire and record thermocouple data for the tests conducted at Lincoln Laboratory. The data from the thermocouples were stored in a computer file. Measurements Group 2120 amplifiers were used for signal conditioning of the strain gages and type A accelerometers. Endevco 2721 charge amplifiers provided signal conditioning for type C accelerometers. Tektronix 2630 and 2641 Fourier Analyzers were used in conjunction with a personal computer to acquire and process the signals from the accelerometers and the strain gages. A Tektronix 2630 analyzer was used in the joint experiment and the features are described in Section 3.1.3. Tektronix model 2641 has the same features except that the maximum analysis bandwidth is 100 kHz instead of 20 kHz. Similar to the 2630 analyzer, an anti-aliasing filter is incorporated for alias protection for the entire 100kHz for unit 2641 [35]. The trigger feature on the analyzers was used to detect and measure vibrations induced by thermal creak as employed in the joint characterization experiment [Section 3.1.3]. An improved trigger method was implemented in later tests, where a circuit board was designed such that if any of signals exceeded a threshold value, the trigger was set off and the analyzer acquired the data.

3.2.4 Test procedures

In this section, the procedure for a typical test is described. The setup varied slightly from tests to tests in effort to improve the experiment. A summary of the setup and the instrumentation is provided in Table 3.5. Any deviation from the general procedure will be mentioned in the results section, if relevant.

Thermal load

The thermal load constraints were imposed by the buckling load of the longerons, cable slackening, and sensor limitations. The buckling load of the longerons is approximately 250 N (54 lb) [36]. Because the longeron is already preloaded to 50% of the buckling load, $\Delta T = 48°C$ is required to cause buckling of the longeron. As mentioned earlier in the chapter, the cables are expected to slacken at $\Delta T = -80°C$. Cable slackening was of concern because once the cable slackens, no more thermal energy can be stored in the structure. The effect of the extreme temperature on the sensor was also considered [Table 3.2 and Table 3.4]. Based on these limitations, a conservative range of -30°C to 50°C was selected to avoid possible damage to the structure or the sensors. Specific thermal load profile for each test will be presented and discussed in Chapter 4 along with the results.

Data acquisition setting

Two Tektronix analyzers were used during each test. For tests conducted at PSI, two units of model 2630 were available. For the Lincoln Lab tests, one unit of 2630 and one unit of 2641 were used. Model 2630 had four channel capability whereas model 2641 had three available. Due to this limited number of available channels on the analyzers, active sensors were limited to seven or eight. The active sensor distribution was fairly arbitrary and varied throughout the experiment. The specific locations will be presented along with the data later in Chapter 4.

The bandwidth of the analyzer was set at the maximum level, 20kHz for model 2630 and 100kHz for model 2641. The highest bandwidth level was selected to reduce the possibilities of detection of vibrations due to other external sources, and high frequency vibrations were of interest. Whenever necessary, the trigger accelerometer was selected arbitrarily. The threshold for the trigger was set barely above the noise level measured by the accelerometers. Ten percent of the acquired data and ninety percent of the acquire data were pre-trigger and post-trigger data, respectively. Similar to the joint experiment, 4096 data

points were selected such that 80 milliseconds and 16 milliseconds of data were acquired for unit 2630 and 2641, respectively.

At the beginning of each test day, the MODE truss was deployed and mounted. The sensors were mounted and wired. Once the temperature range of the test was set, sensor locations allocated, active sensors determined, and the trigger setting completed, the test began. Upon detection of any event, the acceleration data were recorded. The results are presented in Chapter 4.

TABLE 3.5 Experimental setup summary

Test Day	Test Date	Loading	No. of Strain gage	No. of Active Accels	Common Trigger	Temp Range [C]	Sampling Freq [kHz]
1	5/22	1	0	1	N	-20/45	51.2
2	5/29	1	1 (DC)	2	N	-15/45	51.2
3	6/5	1	0	4	N	-25/45	5.12
4	6/20	1	0	4	N	-20/45	51.2
5	6/23	1	0	4	N	-15/45	51.2
6	8/28	1	0	4	N	-20/45	51.2
7	9/2	1	0	8	N	-15/45	51.2
8	9/29	2	0	6	N	-20/25	51.2
9	10/3	3	1 (DC)	6	N	-20/25	51.2/51.2
10	10/8	3	0	6	N	-20/25	256/51.2
11	11/17	1	0	6	Y	-20/25	256/51.2
12	11/18	1	1 (AC)	6	Y	-20/25	256/51.2
13	11/24	1	0	6	Y	-20/25	256/51.2
14	11/25	1	1 (AC)	6	Y	-20/25	256/51.2

Loading 1=convection
Loading 2=radiative with shroud
Loading 3=radiative with cold plates

Chapter 4

EXPERIMENTAL RESULTS

The results from the joint characterization experiment and the dynamic experiment of the MODE truss are presented in this chapter.

4.1 Joint characterization

The results of the joint characterization experiments are presented with emphasis on characterizing the response and assessing the creak models. The static thermal creak response is first investigated. The thermal creak induced vibrations due to the inertia of the joint are then discussed. The results from the model are compared to the data to evaluate the limitations and the capabilities of the model. No dynamic response was detected by the sensors. The predicted model behavior is presented to identify the source of this behavior.

4.1.1 Model description

The static creak model developed in Chapter 2 is used to model the slip joint. The following simplifying assumptions are made in modeling the test article.

1. The thermal responses of both the top and the bottom aluminum bars are identical.

2. The friction parameters are identical at all interfaces.

3. Friction is proportional to the normal load.

4. Slip occurs simultaneously in the axial direction at all interfaces.

5. The clearance is large enough that the edges of the holes are not reached by the bolt.

Based on these assumptions and the symmetry of the system, the test article is modeled as two parallel springs held together by friction as shown in Figure 2.1 without the masses. The spring stiffness representing the aluminum bars, k_1, is twice the axial stiffness of one aluminum bar. Similarly, the composite bar is reduced to a spring whose stiffness k_2 is the axial stiffness of the composite bar.

$$k_1 = 2\left(\frac{EA}{l}\right)_{al}$$

$$k_2 = \left(\frac{EA}{l}\right)_{g/e}$$

(4.1)

where A and l are the cross sectional area and the length of the bar, respectively.

The dimensionless parameters for the slip joint are then computed from the material properties and dimensions given in Table 3.1. These parameters are listed in Table 4.1.

TABLE 4.1   Numerical values of dimensionless parameters for joint test article

Parameters	Values
κ	0.213
α_r	0
f_k	0.99

Preliminary mechanical tests were conducted to determine the static and the kinetic friction values. A quasi-static mechanical load was applied to the specimen via a tensile machine. The displacement of the specimen was controlled by the machine [Figure 4.1]. The loadcell in the tensile machine measured the internal force in the composite bar. When a slip occurs, a sudden drop in the internal load appears in the loadcell history. Because the   internal force in the composite bar is balanced by the friction forces at the
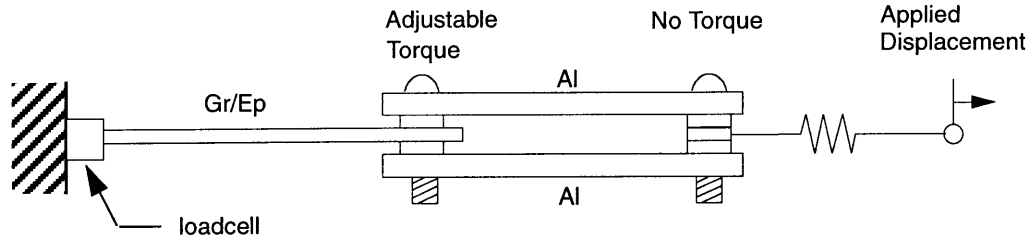
Figure 4.1 Friction test configuration for the joint characterization test article

interfaces, the static friction and the kinetic friction can be extracted from this load history. Many runs were taken at various loading rates and torque levels. The friction ratio f_k ranged from 0.83 to 0.99. The average value was used in the model. The experimental data on the friction parameters and the data reduction process are presented in the appendix for reference.

Critical temperature

Using the model, a relation between the critical temperature and the applied torque is developed. First, the critical thermal displacement for the slip joint is computed using Eq. (2.20).

$$(\xi_1^t)_{cr} = 5.69 \tag{4.2}$$

Using the definition of the critical displacement given in (2.10), the critical temperature can be determined in terms of the static friction. To obtain the relation between the static friction and the applied torque, a linear relation between the normal force and the static friction is assumed.

$$F_s = \mu_s N \tag{4.3}$$

where μ_s is the average coefficient of static friction and N is the normal force. In addition, the normal force for a given applied torque T_A is determined using the following empirical relation [38].

$$N = \frac{T_A}{(0.2 d_b)} \tag{4.4}$$

where d_b is the diameter of the bolt. The coefficient of static friction was experimentally determined to be $\mu_s = 0.063$. Substituting Eq. (4.4) into Eq. (4.3), and using the definition of critical displacement, the following relation is yielded.

$$(\Delta T)_{cr} = c T_A$$
$$c = 2.4 \,^\circ C/Nm \tag{4.5}$$

Thermoelastic response

The temperature measurements are used to determine the thermoelastic response of the aluminum bar. The aluminum bar is assumed to be isothermal at an average temperature. The average temperature corresponds to the average of all the temperature data on the aluminum bars, namely data from locations 1 through 4 and 7 through 10 shown in Figure 3.3. The computed average thermal response is presented in Figure 4.2, where ΔT is the temperature relative to the stress-free temperature as defined in Eq. (2.4). The temperature history of the top aluminum bar shown in Figure 4.2 is the average of the temperature measurements at locations 1 through 4. Similarly, the thermal response of the bottom aluminum bar is represented by the average of the temperatures at thermocouple locations 7 through 10. The thermal response of the graphite/epoxy bar is irrelevant in the model because the CTE of the graphite/epoxy bar is assumed to be zero. Thus the average composite temperature history is not shown. Note that the average temperature history is different for each aluminum bar. This gradient between the bars is neglected in the model.

The average temperature is fit to an exponential temperature function to approximate the temperature of the spring representing both aluminum bars. The dimensionless thermal displacement is then obtained by using Eq. (2.3) and the definition of ξ_1^t given in Eq. (2.10). The relation for the characteristic length x_1^* as a function of the applied torque T_A is derived by using Eq. (4.3) and (4.4). As a result, the thermoelastic response of the aluminum bar takes the form
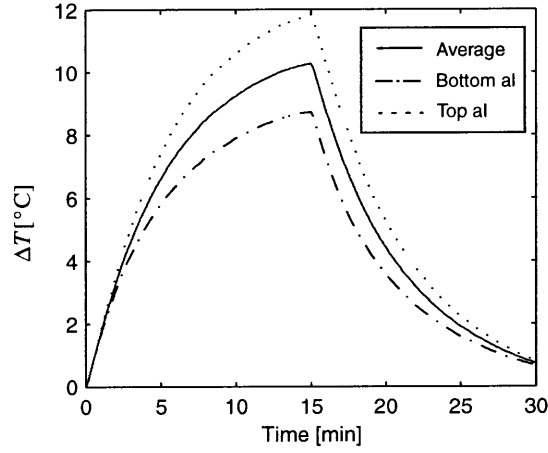
Figure 4.2   Average thermal response of the aluminum bars in slip joint

$$
\xi_1^t = \begin{cases} \dfrac{24.46}{T_A}\left[1 - \exp\left(-\dfrac{\tau}{350}\right)\right] & \text{for } 0 < \tau < 900 \\[4mm] \dfrac{22.24}{T_A}\left[\exp\left(-\left(\dfrac{\tau - 900}{350}\right)\right)\right] & \text{for } 900 < \tau < 1800 \end{cases}
\tag{4.6}
$$

The applied torque T_A is in N-m. The characteristic time is assumed to be one second for convenience such that $\tau = t$.

To simulate the joint response, Eqs. (2.16) and (2.17) were integrated in time using the thermoelastic response given in Eq. (4.6) for each torque level in the test matrix. The dimensionless displacements are then multiplied by the characteristic length to give the physical displacements in meters.

4.1.2 Thermal creak response

The experimental results are presented and discussed in this section. The average joint response under a range of loading conditions is characterized. The data and the model results are qualitatively correlated. The magnitude and the profile of the energy release are compared to the model predictions. Behaviors not captured by the model are identified and the key parameters revealed by the experimental work are presented and discussed.

The composite displacement histories will be used to characterize the creak response because the slips are more noticeable in the composite data.

The axial displacements of each component of the slip joint for a range of applied torques are presented in Figure 4.3 through Figure 4.5. In each plot, the three solid lines correspond to the data from the three test runs. The model results are shown in the dotted lines. The vertical dotted lines in the composite displacement histories indicate the initial slip points in the heating and the cool-down periods predicted by the model.

The mean displacement history of each component at each applied torque is computed from the data to characterize the average behavior. Recall that only one channel was available for acquiring the displacement data [Section 3.1.3]. Based on the assumption that the data from each component are consistent, a small deviation between the average data and the results from the individual runs is expected. Figure 4.3 through Figure 4.5 show that the scatter in the data is no more than the disagreement between the model and the data. A few exceptions are found where the response of the aluminum bars deviate significantly from the norm, namely the histories shown in Figures 4.3a, 4.3c, and 4.5d. These outliers were excluded in the averaging process. The average response and the model results for the range of applied torque are plotted in Figure 4.6 and Figure 4.7.

Average response

The average joint response displays typical creak response characteristics seen in the modeling chapter [Chapter 2]. The beam expands together until the critical state is attained and at this point, the aluminum bars slide relative to the composite. Some presliding displacements, however, were observed in the data. Presliding displacements or microslips are small relative motions prior to the true sliding. Such a series of small relative displacements is indicated by the smooth transition from the completely stuck to the sliding region. In some of the composite displacement samples, presliding displacements are strongly apparent as seen in Figure 4.8. Figure 4.3 through Figure 4.5 show that the presliding displacements are more apparent as the applied torque increases.

Figure 4.3 Axial displacements of the slip joint under a thermal cycle for T_A=5 in-lb and 10 in-lb

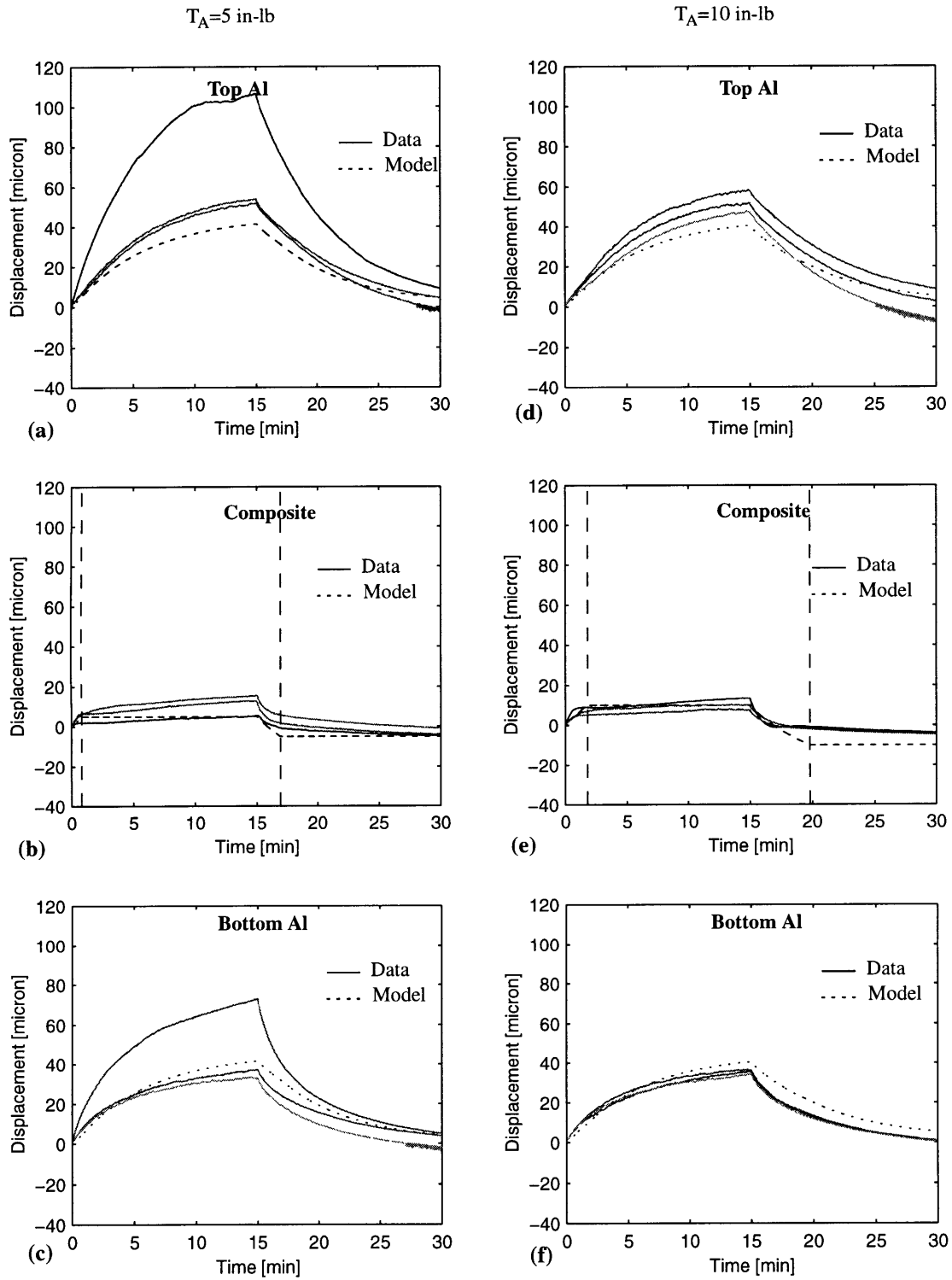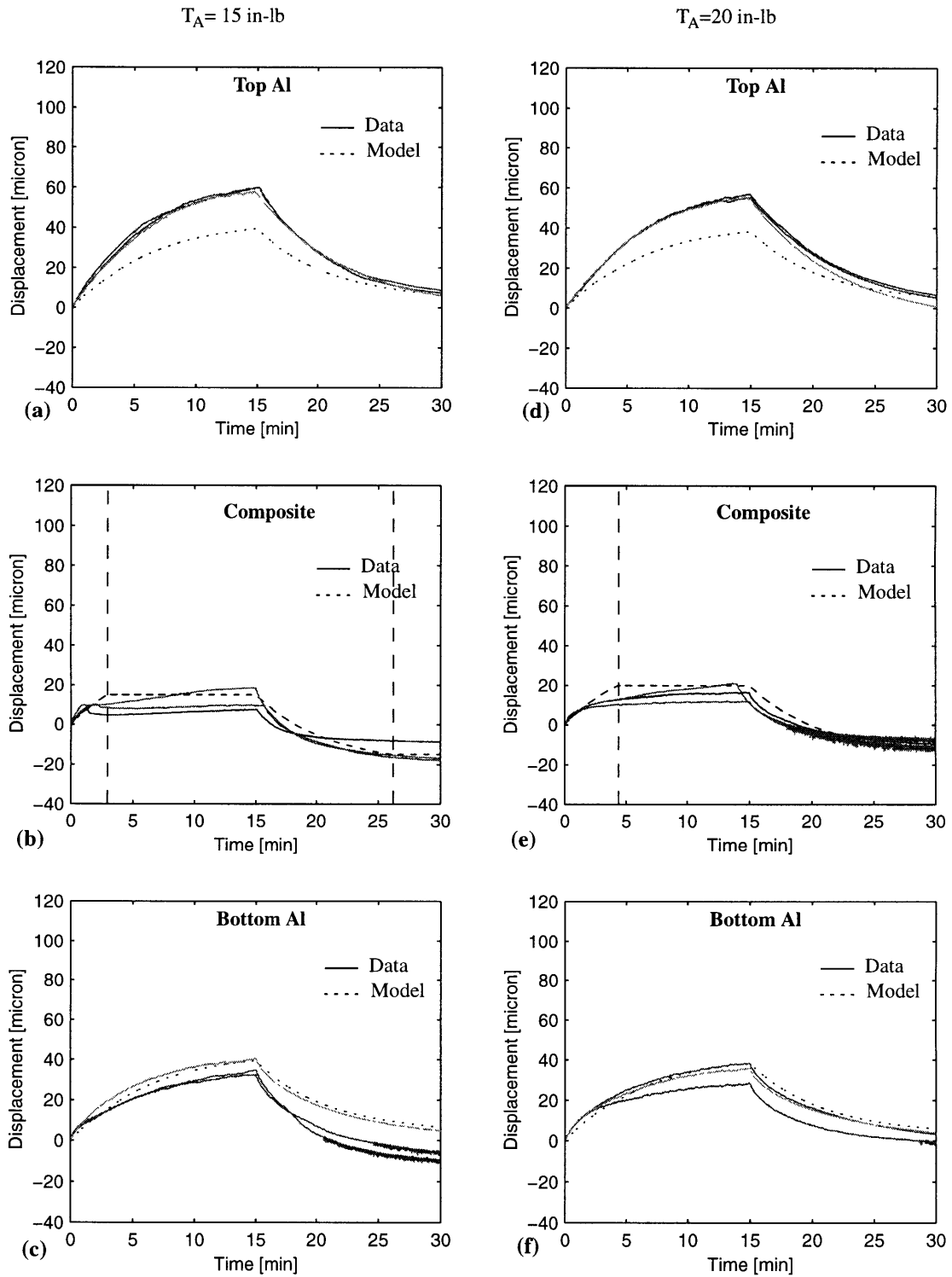**Figure 4.4** Axial displacements of the slip joint under a thermal cycle for T_A=15in-lb and 20 in-lb

Figure 4.5   Axial displacements of the slip joint under a thermal cycle for T_A=25 in-lb and 30 in-lb
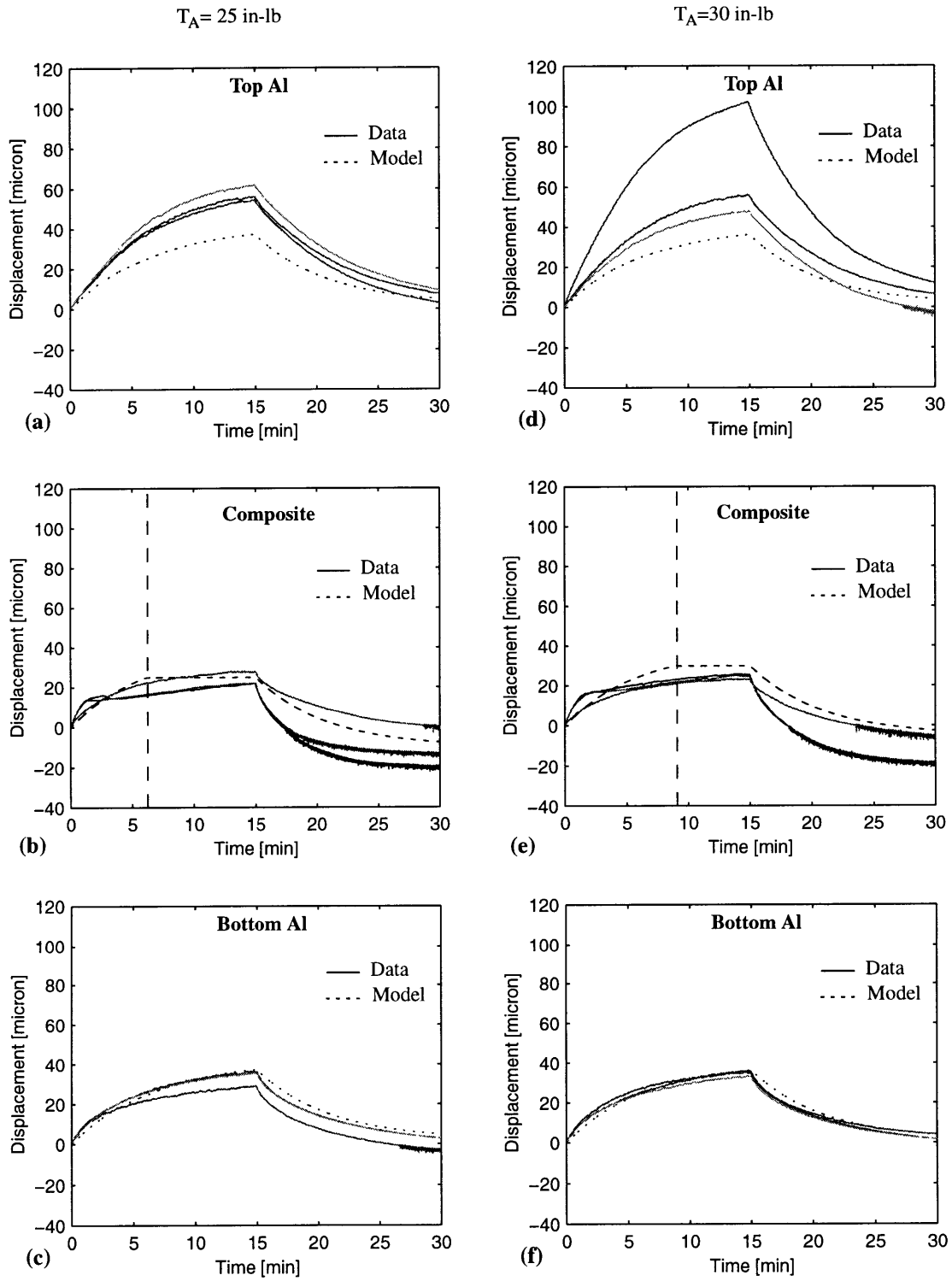
Data   **Model**
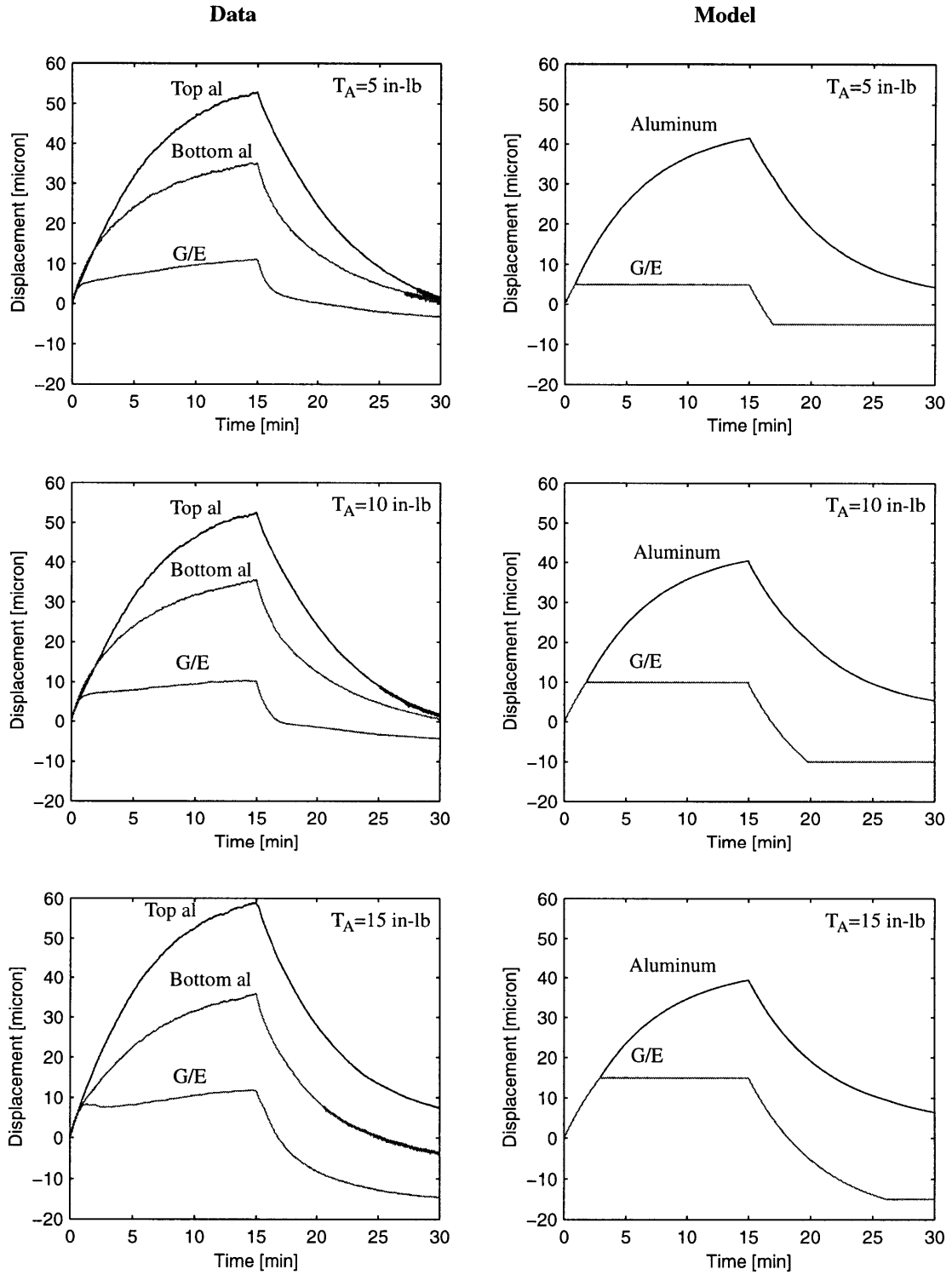
Figure 4.6   Average joint response for T_A=5 through 15 in-lb
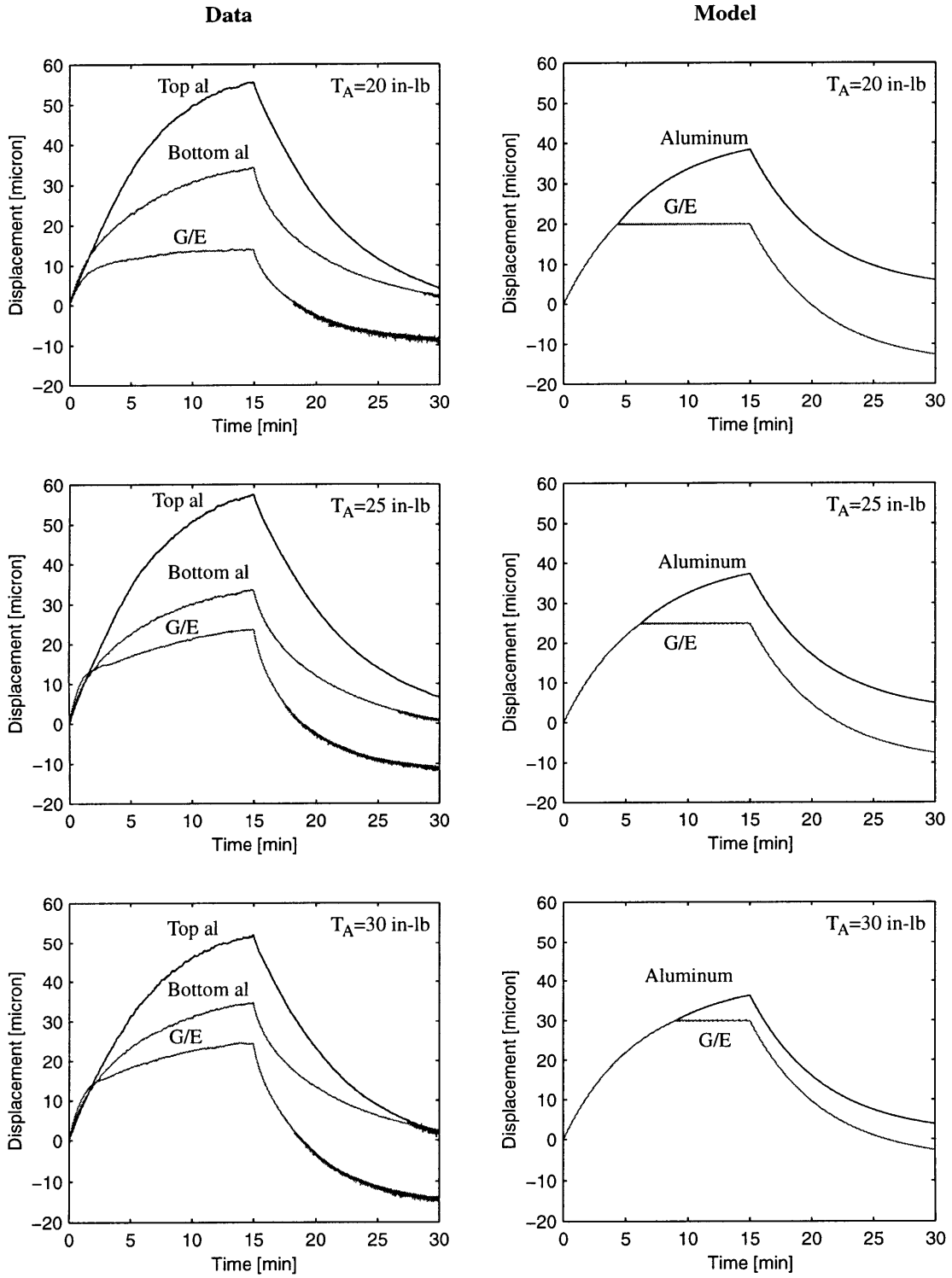
Figure 4.7 Average joint response for T_A=20 in-lb through 30 in-lb
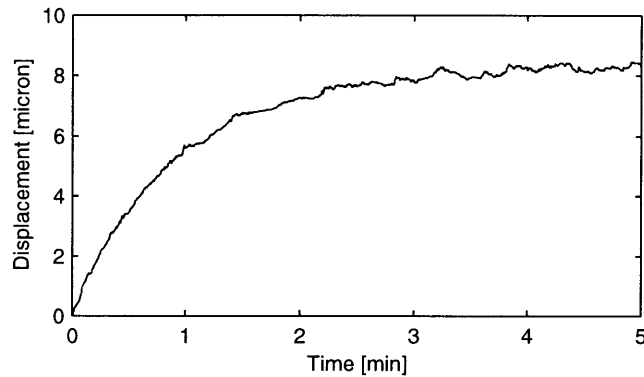
Figure 4.8 Presliding displacement seen in g/e displacement data for T_A=10 in-lb

Magnitude and profile of energy release

In most of the composite displacement histories, continuous sliding appears to be dominant. The model predicts the magnitudes of the slips in the composite to be 0.04-0.26 microns for the range of the torques used in the experiment. A magnified plot of a model response is presented in Figure 4.9 to illustrate the behavior. It is difficult to determine whether frequent small amplitude stick-slips are also occurring in the data. As discussed
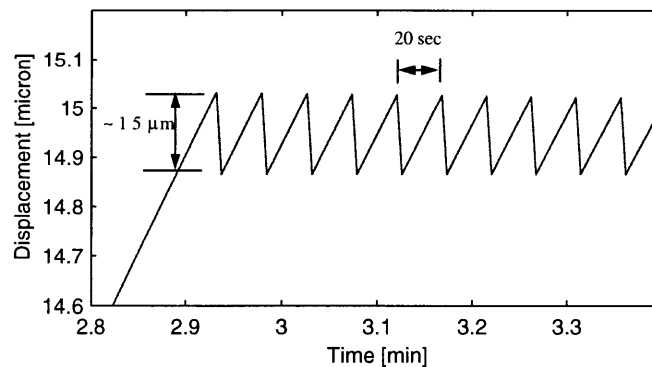
Figure 4.9 Displacements predicted by Coulomb friction model for T_A =15 in-lb

in Section 3.1.3, the calibration for the composite displacement data at T_A=5-15 in-lb is 2.048 μm/V. For the composite data at T_A=20-30 in-lb and for all of the aluminum data, the calibration was set at 32.76 μm/V. As a result, the slip amplitude predicted by the

model corresponds to a change in the signal to be on the order of 0.01 V. Such a change in the signal is difficult to distinguish from the noise.

The slip magnitudes in the composite data ranged from small, yet noticeable, slips of approximately 0.3 micron to a large amplitude slips of approximately 3 microns. The smaller slips were observed throughout the data once a slip was initiated. They are not discernible in Figure 4.3 through Figure 4.5 because the magnitude is very small relative to the total displacement. The large amplitude slips (on the order of 1 micron) occurred only as initial slips. One of these large amplitude slips was detected in a test run for T_A =15 in-lb. A magnified plot of this displacement history is presented in Figure 4.10 for clarity. As indicated by the relatively long duration of slipping (approx. 30 sec), these gross slips have a smooth profile unlike the step profiles seen in the model. A similar variations in the slip amplitudes were observed during the cool-down period as well.

The loading rate may be a key factor in inducing the large amplitude slips because the loading rate is high initially and then decreases with time. Although the creak model
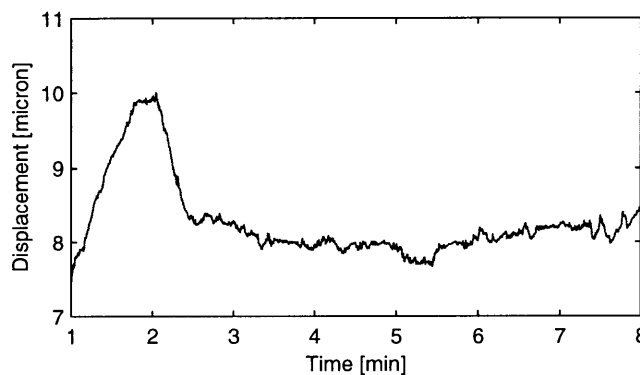

Figure 4.10 Displacement of composite bar from experimental data for T_A =15 in-lb

does not capture the scatter in the slip amplitudes, the results are consistent with the majority of the data. The slip profile however is much sharper than that observed in the data.

During the cool-down, stick-slips occur in the reverse direction [Figure 4.3-Figure 4.5]. This phenomenon is counter-intuitive because the temperature is not lower than the stress free temperature.   When the thermal load is reversed, the components of the beam stick again. The relative displacement at this point is not zero and thus some initial stress exists. As a result, a slip occurs before the beam cools to a temperature lower than the room temperature. The same characteristics found in the heating period such as the presliding displacements were exhibited during the cool-down.

Figure 4.3-Figure 4.5 demonstrate that the model captures the overall response well. In the model, the components of the slip joint move together until the critical point and a series of frequent, small amplitude stick-slips follows. When the heat is turned off, the same behavior is repeated in the reverse direction. Because the slip amplitudes are very small relative to the total displacement, the large time scale behavior appears as a continuous sliding motion. No presliding displacements are present in the model response due to the limitations of the Coulomb friction model.

Some discrepancies between the model and the data are found. First, a substantial difference in the responses of the top and the bottom aluminum bars were measured. The significant difference is mostly attributed to the temperature difference between the two bars as shown in Figure 4.2. The temperature gradient at the end of the heating period is approximately $4\ ^\circ\mathrm{C}$, which corresponds to a difference in the displacement of approximately 17 microns. Because the model assumes that the thermal response of both aluminum bars is identical at an average of the two, the model underestimates the displacement of the top aluminum and overestimates the displacement of the bottom aluminum. Other factors such as the bending of the beam may also contribute to the discrepancy. Second, the data show that once the sliding is initiated, the displacement of the composite slightly increases. The model response, however, flattens out after the initial slip. This drift may be due to the fact that the CTE of the composite is not exactly zero. For the higher torques, the drift is more pronounced. Recall that the microslips are more dominant in the

higher torque data. Thus the effect of the presliding displacements become more visible in the average response in the higher torque data.

Critical displacement

Several trends are investigated as the torque, and hence the friction, is increased. The critical displacement of the composite at which the slip is initiated in the heating period is extracted from the raw data. The slip initiation point was determined to be where the true slip occurs and not where the microslips begin. The critical displacement as a function of the applied torque is presented in Figure 4.11. The solid line represents the analytical relation derived from Eq. (2.16) and Eq. (2.20), assuming that the initial relative displacement is zero. The figure suggests that at low torque values, the critical displacement appears to be fairly constant. Relatively large scatter in the data is displayed for $T_A = 5$ in-lb. A larger error is introduced at lower torques because the percent error in the applied torque is higher. As the torque increases, the critical displacement increases linearly. The model overbounds the data and qualitatively captures the linear trend for the higher torques.
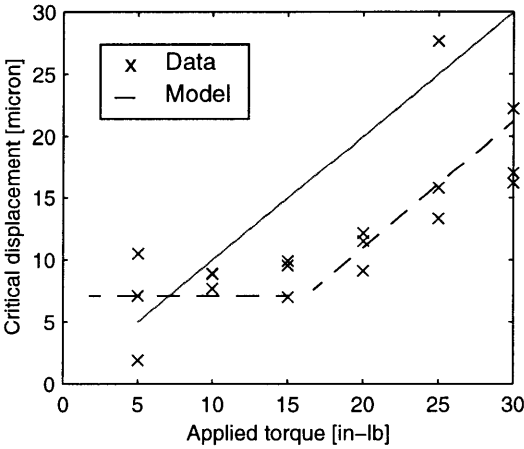
Figure 4.11 Critical displacement vs. applied torque

Total displacement

The experimental results showed that the stored energy in the joint was released by varying magnitudes of slips, from microslips to large amplitude slips. The cumulative effect of these slips are reflected in the final relative displacement at the end of the heating period. The final relative displacement should provide some insight to the total energy dissipated during the heating period. The magnitude of the relative displacement at the end of the heating cycle as a function of the applied torque is plotted in Figure 4.12. The relative displacement between the top aluminum bar and the composite is summed with that between the bottom aluminum and the composite. Similarly, the relative displacement computed from the model is doubled. The figure implies that, on average, the displacement and hence the total amount of energy released decreases with increasing friction, as expected. For a relatively low torque, the response is relatively the same. As the torque increases, the magnitude of the relative displacement appears to decrease linearly, a similar trend seen in Figure 4.11. The model response qualitatively agrees with the data for the larger torque values. Quantitatively, the model underestimates the displacement as the torque is increased.
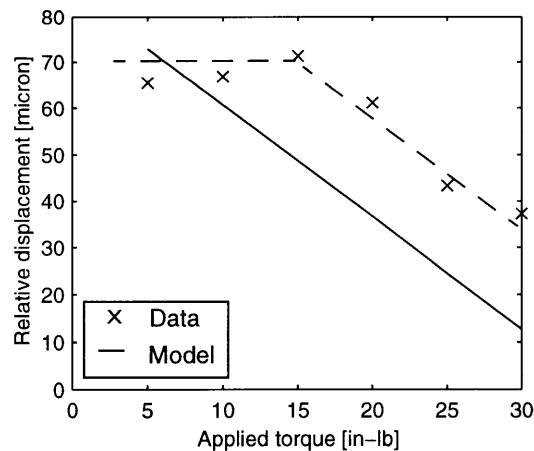

Figure 4.12 Total relative displacement at the end of the heating cycle for a range of applied torque.

Equilibrium zone

The final relative displacement in the heating period has a significant effect on the creak response during the cool-down, because it is directly related to the initial stress at cool-down. The slip joint may not attain the critical slip state in the cool-down for a sufficiently large friction load. For torques of 15 in-lb and higher, the slips in the cool-down are eliminated as seen in the data and the model response [Figure 4.6 and Figure 4.7]. To further investigate the effect of the thermal cycling or the loading history on the slips, the joint response under a series of thermal cycles was computed using the model. The results for T_A =10 in-lb and T_A =20 in-lb are presented in Figure 4.13 and Figure 4.14, respectively. For the lower torque, the slips continue to occur both during the heating and the cool-down periods. The relative displacement reaches a periodic behavior at steady state. For the higher torque, the change in the relative displacement decreases until a constant value is reached at steady state. These results imply that a similar phenomenon analogous to the equilibrium zone, studied by [39], may be displayed by the joint.

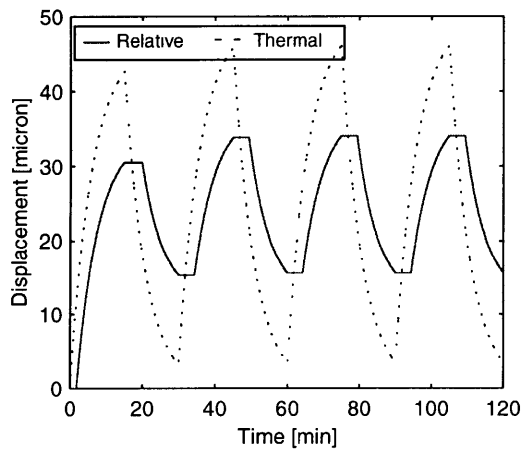O

Figure 4.13 Simulation of joint response under mul-tiple thermal cycles for T_A= 10-in-lb
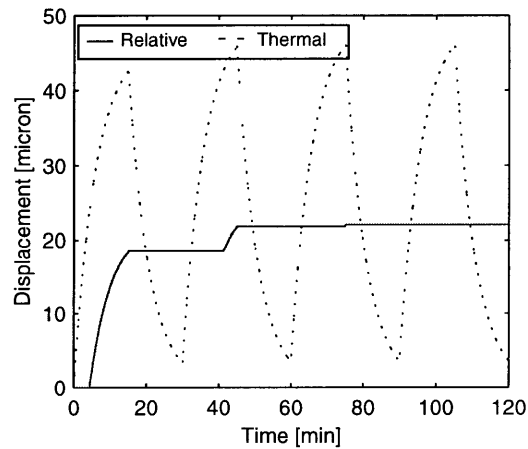
Figure 4.14 Simulation of joint response under multiple thermal cycles for T_A= 20-in-lb

Sensitivity analysis

To qualitatively investigate the effect of the parameters on the response, the parameters were deviated from the nominal values shown in Table 4.1. Recall that the magnitude of

the disturbance is proportional to the quantity $(1-f_k)$ for the static creak element [Eq. (2.19)]. Thus, when f_k was varied from the nominal value, the magnitude of the response varied by the change in the quantity $(1-f_k)$. Note that the characteristic length x_1^* acts as a scaling factor to the magnitude of the response. Thus, the magnitude is linearly proportional to x_1^*.

Source of discrepancies

The discrepancies between the model and the data were found in the slip amplitudes, the critical displacement, and the total displacements. These discrepancies can be attributed to the following sources:1) unmodeled friction behavior, 2) multiple friction interfaces, and 3) data reduction.

The complex behavior of friction was discussed in Chapter 1. Friction is a function of many parameters including the temperature, the loading rate, and time due to wear and other time dependent states. In the experiment, the temperature of the interfaces and the loading rate changed with time. The large amplitude slips are one of the indications that the loading rate affects the creak response. In addition, the experiment was conducted over the period of two months and thus the friction parameters are likely to have changed over the course of the experiment. The static creak model however assumes that the friction is a normal load dependent Coulombic friction, which is determined by two parameters - coefficients of static friction and kinetic friction. As a result, the creak model does not capture presliding displacements or the variation in the slip magnitudes and profiles.

The multiple interfaces in the system introduce some variation in the data and additional complexities not modeled in the static creak element. The slips do not occur simultaneously at all interfaces as simplified by the model. In addition, the friction behavior at each interface differs from the other. These interfaces introduce additional energy dissipation and variations in the initial slip points.

Some error was introduced in reducing the friction characterization data. The testing conditions for the mechanical tests were different from that of the thermal tests. The

mechanical tests were conducted at a room temperature and at a loading rate different from the joint characterization tests. The friction parameters however are assumed to have remain unchanged between these two different experiments. Further, the average values of the friction parameters were used in the model despite the fact that the parameters did vary with the loading rate.

4.1.3 Thermal creak induced dynamics

The dynamic creak element model developed in Section 2.3 is implemented to compute the dynamic response of the joint due to thermal creak. In the previous section the static creak element model was used to capture the large time scale response because the structural response time of the joint is very high compared to the thermal time scale. The first natural frequency of the aluminum bar in the longitudinal direction is approximately 14 kHz as mentioned in Section 3.1.3. As seen from the static creak response, the creak frequency is much lower than the natural frequency of the system. Thus the dynamic response due to a single slip is investigated.

The model results are computed by integrating Eqs. (2.45) and (2.47), using the numerical values of the parameters given in Table 4.1. Similar to the static analysis, the resulting dimensionless states are rescaled back to physical time and lengths using the characteristic length and the characteristic time, defined in Eq. (2.43).

The model response for an applied torque of 30 in-lb is plotted in Figure 4.15 to illustrate the behavior. The magnitude of the acceleration is very large due to such a high natural frequency. As mentioned earlier, no dynamic response was detected by the accelerometers, despite such a large amplitude acceleration predicted by the model. It is possible that the Coulomb friction assumption is not appropriate for this system. The model assumes that an instantaneous change in friction occurs when the slip is initiated and terminated. The displacement data however suggest that the friction changes rather slowly compared to the structural response time. Consequently, the system is not excited. The results imply that for a very stiff system subjected to a relatively low loading rate, dynamic response
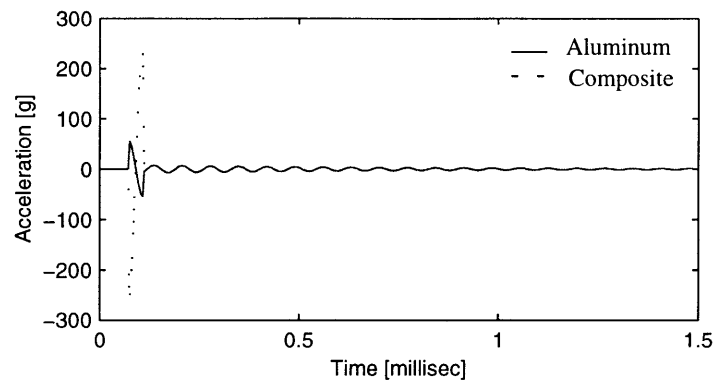
Figure 4.15 Joint accelerations predicted by model for $T_A = 30$ in-lb

should not be expected. Conclusions about the dynamic response of a system that houses such a stiff component cannot be drawn from these experimental results.

4.1.4 Summary

In summary, thermal creak was demonstrated in a typical joint type component. The behavior described by the model was displayed in the experiment and thus validating that the model incorporates the mechanisms that cause thermal creak. Qualitatively, the creak model correlates well with the data. The model captures the main characteristics and trends seen in the experimental results.

The assumptions in the model introduced some error. The sources of discrepancies in the slip amplitudes, the energy dissipation, and the initial slip instances were identified. The loading rate and the uncertainties in the friction parameter contributed to these discrepancies. The main discrepancy was found in the dynamic response of the system. A simple Coulomb friction model was sufficient in capturing the key behaviors in the large time scale response, but it was not appropriate for predicting the dynamic response for such a stiff system. A higher order friction model can capture a wider range of behaviors, including presliding displacements and dependence on loading rate. However, the complex friction model requires more parameters to be determined experimentally. Uncertainties in friction parameters and environment are expected in real structures thus building a com-

plex friction model that captures these behaviors may not be feasible. The Coulomb friction model may be applicable for a wide range of systems under a wide range of loading conditions, if the friction in a component changes relatively fast compared to the structural response time. The effect of thermal creak on the dynamics of an attached system cannot be generalized based on the results of this very stiff system.

4.2 Thermal creak induced dynamics experiment

Due to the large number of potential creak elements in the truss, obtaining a deterministic creak model of the MODE truss is impractical. Unlike the experiment for the joint characterization, no data on the friction parameters or the joint behaviors exist. In addition, the creak source was not isolated. As a result, the actual location of the creak source, the creak frequency, and the magnitude of energy release cannot be determined *a priori*. Information on the location of the sources, the magnitude of the response, and the propagation path can only be inferred from the data. The results from the thermal tests on the MODE truss are presented in this section. The structural response due to thermal creak is characterized and a qualitative correlation with the model is presented.

4.2.1 Model description

In Chapter 2, the parametric study indicated that a wide range of structural response was possible depending on the parameters. The key nondimensional parameters depend on the slip mechanism. The creak source, the direction of slip, friction parameters, and the location of creak source all affect the type of structural response expected in the dynamics experiment. Here, a static model is developed to evaluate the energy storage level. A creak model is developed by assuming a creak source and mechanism.

Thermoelasticity model

The thermoelastic response of the structure under the thermal loading conditions are qualitatively characterized to understand the energy storage mechanism in the structure. The thermal properties of the different materials in the structure are listed in Table 4.2. Recall

that the convection chamber provides a fairly uniform thermal load. The convective heat transfer coefficient for the turbulent air in the chamber is assumed to be 100 W/m²-K. The Biot number for the aluminum joints and the steel diagonal wires are on the order of 0.001, and thus a lumped analysis is valid in approximating the thermal response of these components. The thermal time constants are approximately 30 seconds and 130 seconds for the steel cable and the aluminum joints, respectively. Based on the time constant of the cable, the lag between the cable and the ambient temperatures is assumed to be negligible. The Biot number for the Lexan strut is approximately two due to the low thermal conductivity. Thus a temperature differential between the surface and the center of the strut is expected. The time constant associated with the radial conduction for the strut was computed to be approximately 120 seconds. During this duration, the ambient temperature changes approximately 8 °C and -3.4 °C at heating and cooldown period, respectively. As a result, the difference in the average temperatures of the aluminum joint and the lexan strut are relatively small. A fairly uniform temperature distribution in the truss structure is expected. Based on these time constants, it is assumed that the ambient temperature is a relatively good representation of the structural temperature in the convection tests.

TABLE 4.2 Thermal properties of MODE components

Parameter	Lexan	Aluminum	Stainless Steel
C_p[J/kg-K]	1300	962	628
k [W/m-K]	0.2	200	16

Recall that two different setups were implemented to radiatively cool the structure in the vacuum chamber. In both loading conditions, the transient thermal response is difficult to determine analytically because the emissivity values of the different components in the truss are not known. The first setup using the shroud resulted in a non-uniform temperature distribution in the structure due to the differential heating between the top and the bottom shroud. The second setup, using the cold plate, however, maintained a relatively uniform temperature. Due to the slow radiative heat transfer and good conduction paths

in the structure, the temperature distribution is assumed to be fairly uniform for this thermal loading setup. The conduction characteristic time is faster than the radiative heat transfer characteristic time, and thus the surface temperature is assumed to be a good representation of the structural average temperature.

A static analysis of the truss is performed to compute the change in the internal forces in the structure due to the thermal load. The static analysis assumes that the truss member carries axial loads only. The equilibirum relations for the truss in conjunction with the constitutive relation are first established. By imposing a geometric constraint that the truss maintains the box shape, the strain of the truss members can be computed. For this application, the analysis assumed that the structure is isothermal. For the convection tests, the structural temperature is assumed to be the ambient temperature. For the radiative tests, the average of all the surface temperature measurements was taken to be the structural temperature. The reduced temperature data were then fit to an exponential function and input to the static model.

The structural properties used in the static analysis are obtained from the finite element model of the truss [36]. Most of the material properties and the dimensions are obtained from [36]. The coefficients of thermal expansion were obtained from other references [Table 4.3]. Because the longeron consists of dissimilar materials, the effective coefficient of thermal expansion (CTE) is computed to be 4.2×10^{-5} $^\circ C^{-1}$.

TABLE 4.3 MODE truss member CTE

Truss member	CTE $[10^{-6}/^\circ C]$
Longeron	42.0
Batten	62.5
Diagonal	14.5

Creak model

The possible sources of thermal creak in MODE were discussed in Chapter 3. In this chapter, one of the potential sources are investigated to correlate the model results with the experimental data and to demonstrate the capabilities of the model. The creak source is assumed to be the pin joint in the longeron in the first bay. One of the longerons slips in the longitudinal direction relative to the batten frame fitting, and hence the rest of the bay. The slipping longeron is assumed to be located in one of the end bays. The creak source and the location are qualitatively identified using the data and this identification procedure is discussed in the model correlation section with the results.

Once the creak source and the slip mode are assumed, the MODE truss is reduced to the simple model developed in Chapter 2. The first bay is represented by the creak element and the attached SDOF system is now replaced with a MDOF system representing the remainder of the structure. The slider shown in Figure 2.1 represents the slipping longeron and the pin represents the rest of the bay without the slipping strut. The degrees of freedom of interest are the axial motion of the slipping strut and the axial motion of the bay at the interface.

The model parameters are extracted from an existing finite element model developed by Barlow [36]. The stiffness and the mass matrices of a single bay without the nonlinear strut was used. The stiffness k_1 is the stiffness associated with the degree of freedom at
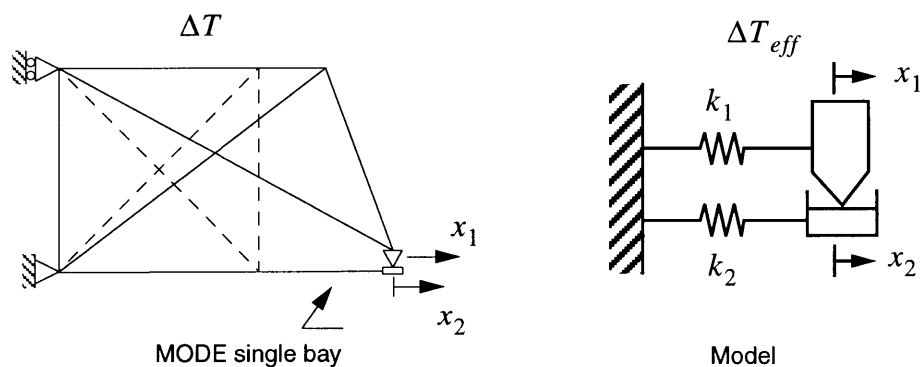

Figure 4.16   MODE creak model

the friction interface, obtained by static condensation. The axial stiffness of the strut k_2 is computed assuming a linear deflection. To approximate the effective modal mass m_1, the frequency associated with the mode closest to the slip modeshape is used. The modal mass for the slipping longeron m_2 was approximated to match the first longitudinal mode frequency of the strut. The thermal displacement mismatch parameter α_r is determined by assuming that the temperature distribution is uniform. No data on the friction parameters of the MODE joints are available and thus an assumed value is used. The friction ratio at the interface is assumed to be relatively high. The model parameters are shown in Table 4.4. Both a static and a dynamic creak models are used. To determine the internal forces the static creak model is used. For determining the dynamic response of the structure, the dynamic creak element is used.

An existing finite element model of the MODE truss was used to obtain the modeshapes and the frequencies. The assumption that the motion of the first bay is dominated by the slip mode is made. In the modal analysis, only the higher modes were used because the data were in the high frequency range. The structural dynamics model included 27 modes in 1400-3000 Hz range and a modal damping ratio of 0.015. The creak response is applied at the node at which the slip occurs as an excitation force.

TABLE 4.4 Numerical values of the MODE creak model parameters

κ	15
α_r	0.07
f_k	0.95
μ	0.073
ω [rad/s]	1320

The results from the dynamics experiment are presented and discussed in the subsequent sections. The thermoelastic responses of the structure in the two thermal chambers are characterized. The dynamic response of the structure due to the thermal creak is then characterized. The responses under the two different loading conditions are compared.

Some data reduction was necessary to isolate thermal snap events from other events observed during the tests, such as electrical events. For details on the data reduction and identifying thermal snap events, refer to [37].

4.2.2 Thermoelastic response

The thermal response and the stress state of the MODE truss in the convection and the radiative chambers are qualitatively characterized to understand the energy storage mechanism. The critical temperature at which the creaks occurred are presented to quantify the bounds on the energy storage.

Convection tests

The temperature history of the ambient air for test day 1 is shown in Figure 4.17. The figure represents a typical temperature history of most of the convection tests. The temperature histories for the remaining test days are shown in [37]. As expected, the surface temperature of the structure is very close to the ambient temperature. The exponential fit to the data, as discussed earlier in the model description section, is shown in solid line.
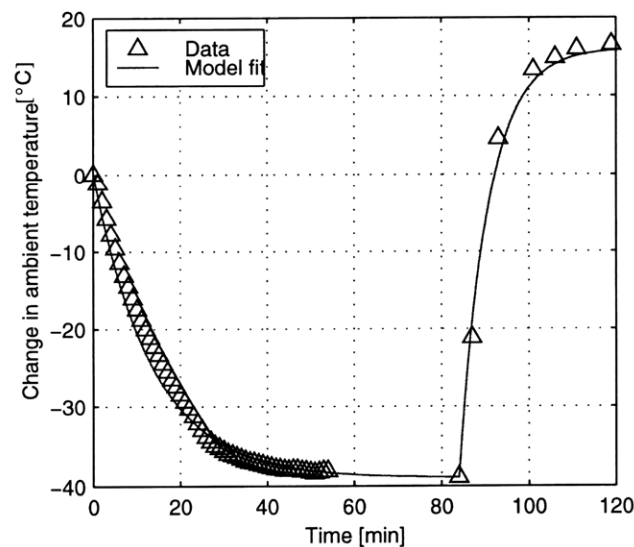

Figure 4.17 Ambient temperature history on test day 1

The corresponding strain measurement in the steel diagonal is plotted in Figure 4.18. The predicted mechanical strain in the truss members are plotted along with the experimental results. The figure indicates that as the ambient temperature decreases, the strain, and hence the tension in the diagonal is reduced, as the model predicts. Note a large discrepancy between the model and the data exists [Figure 4.18]. It is likely that the energy dissipation due to various slips contributed to the lower change in the mechanical strain. The strain is computed using the static creak model for a qualitative comparison [Figure 4.19]. The parameters listed in Table 4.4 were used and the initial state was chosen to match the magnitude of the strain.
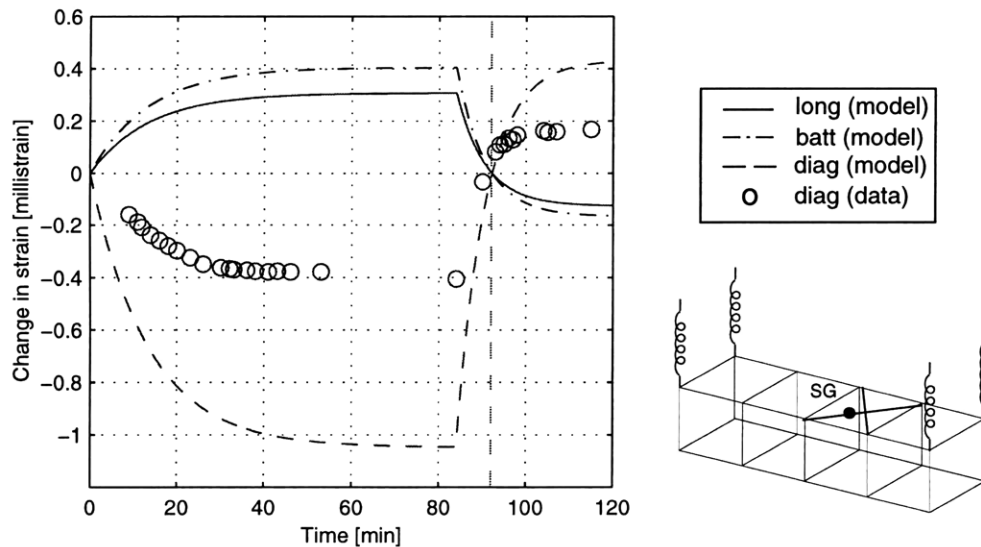
Figure 4.18   Strain history on test day 1

Radiative tests

The strain measurements during the radiative tests were taken on test day 9 using the second setup where the cold plates were used to apply the thermal load [Table 3.5]. The corresponding temperature history of the structure is presented in Figure 4.20. Selected temperature data are presented due to the fairly uniform response. The average temperature was computed as the mean of all the temperature measurements at different locations. The thermal response of the structure under the first setup with the shroud is significantly
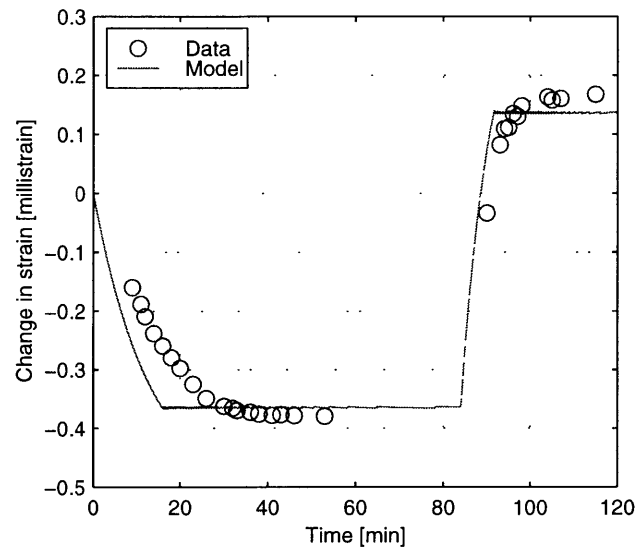
Figure 4.19 Correlation of strain history with creak model

different and is discussed later when the relevant results are presented. Figure 4.20 shows that initially a significant lag between the structure surface temperature and the cold plate temperature exists. As the time progresses, conduction within the structure dominates and thus the temperature distribution becomes fairly uniform.
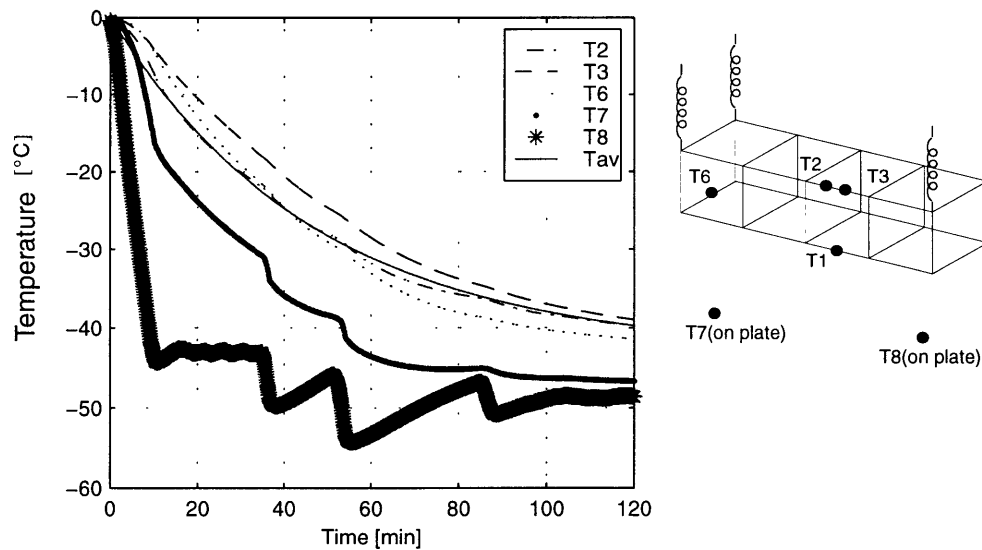

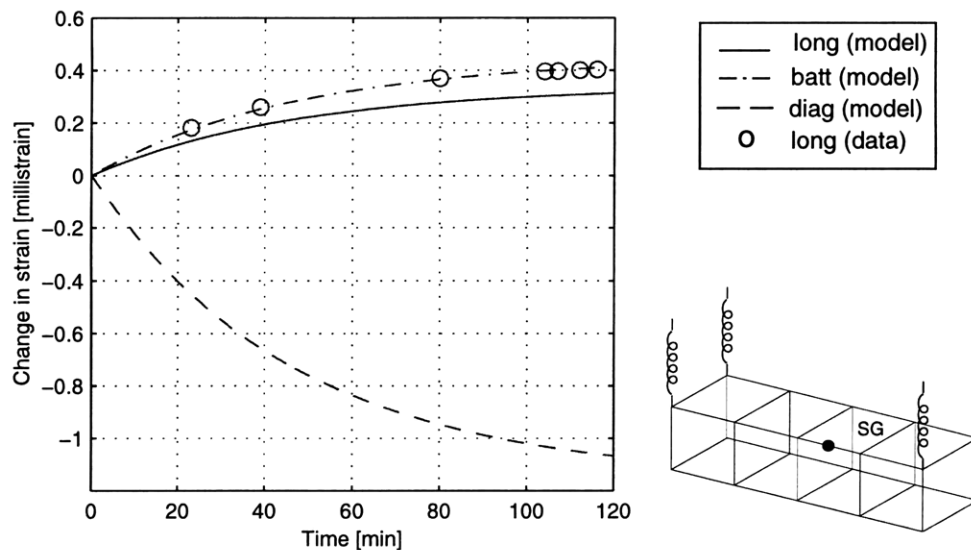**Figure 4.20** Temperature history on test day 9

Figure 4.21 Strain history for test day 9

The strain in one of the longerons in the adjustable preload bay was measured. The strain history is presented in Figure 4.21. The model results based on the static analysis is presented. The figure shows that the model agrees with the radiative test results relatively well. Unlike the convection test results, the model underpredicts the strain level. Despite the fact that the temperature distribution in the structure for both test days are fairly uniform and the total temperature change in both cases are approximately -40 °C, an inconsistency between the convection test and the radiative test exists. The discrepancy suggests that the slips were smaller and less frequent than those encountered in the convection tests.

Critical temperature

The temperature at which an event was observed was recorded. The results are presented in Figure 4.22 and Figure 4.23. All the temperatures are relative to the room temperature as indicated by Δ. For the convection tests, the ambient temperature is plotted. For the radiative test data, the average surface temperature of the structure at the time of the events is used. The plots show that no events were detected at absolute ΔT's below a certain level, suggesting that a critical state related to the thermal input exists. A more random

trend would be displayed if the events were mechanically induced. The variation among the events is primarily attributed to varying creak sources from event to event.

Note that most events were observed during the cooling period. As seen in the joint experiment results, slips were allowed during the stress relaxation because of the loading his
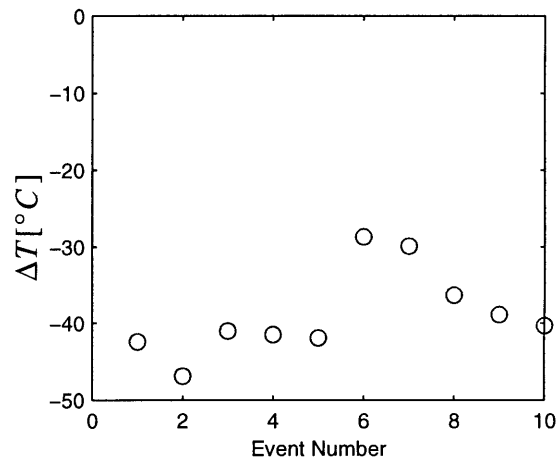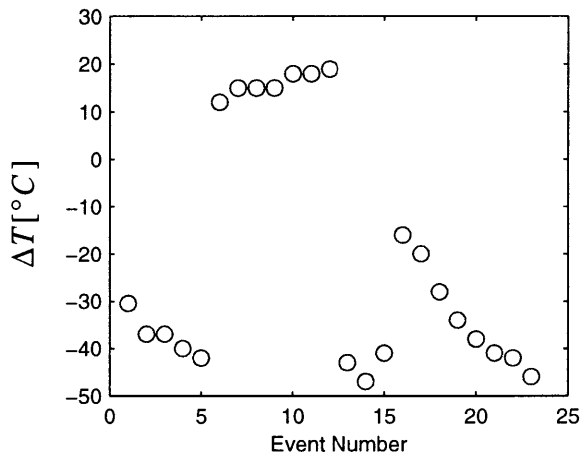
Figure 4.22 Ambient temperature at event occurrence during convection tests

Figure 4.23 Average surface temperature at event occurrence during radiative tests

tory condition. The critical stress at which an event occurs is difficult to obtain because the exact internal forces depend on the loading history, energy dissipation from prior slips, and initial condition.

4.2.3 Dynamic response characterization

Experimental results from one test day from both the convection tests and the radiative tests are presented to qualitatively characterize the dynamic response of the truss structure due to thermal creak. The thermal load history is first shown along with the times of the events. The spatial and time variation of the creak events are discussed. The creak source location and energy propagation paths are qualitatively characterized. Data from the remaining test days can be found in [37].

Convection tests

The results from the seventh test day are presented in this section. The temperature histories of the ambient air and the surface of the truss are shown in Figure 4.24. As mentioned in Chapter 3, only one thermocouple was used to monitor the surface temperature of the structure because the surface temperatures at various locations were uniform. The dotted vertical line indicates the time at which an event was detected and recorded.
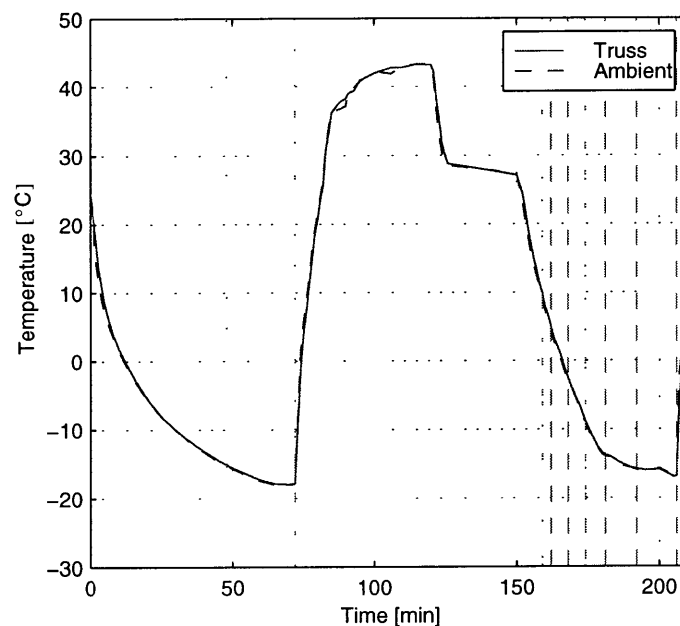
Figure 4.24 Temperature history for convection test on test day 7

The thermal cycle begins with cooling to achieve a ΔT of -40 °C in 70 minutes. The second cycle begins at approximately t=150 min and attains a ΔT of -40 °C in 50 minutes. The loading rate was higher in the second cycle. Note that the thermal profile is very similar to that on test day 1 shown in Figure 4.20. Thus a similar strain history is assumed for this test run.

The dynamic response of the structure at the third event is presented in Figure 4.25. The locations of the accelerometers are denoted by the circle. The accelerometers are labeled with either A or C to indicate the type of the accelerometer. The arrow next to the acceler-

ometer denotes the direction of the acceleration measured. An accelerometer was placed on the chamber ceiling by the suspension spring attached near C2.
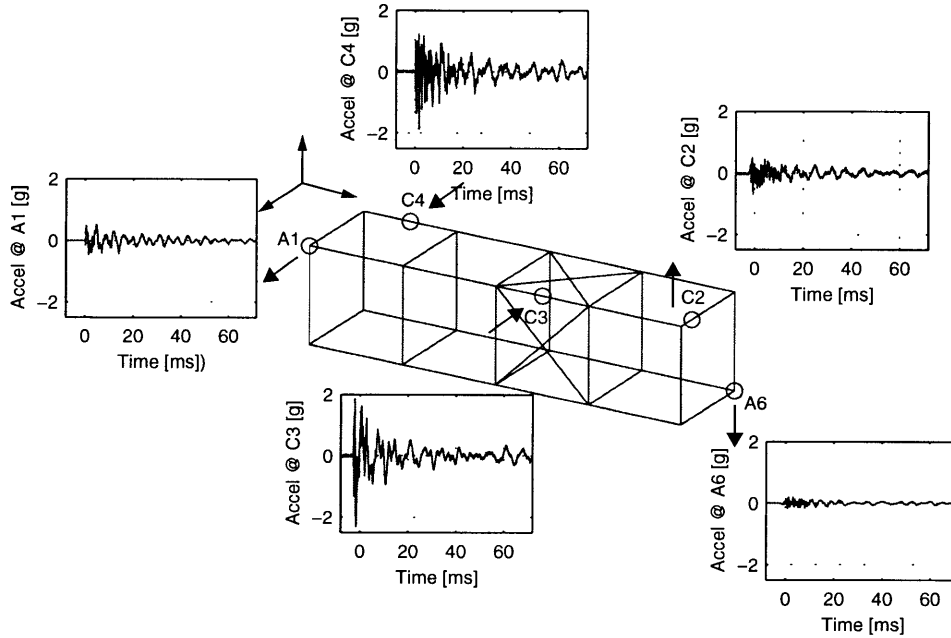
Figure 4.25 Time response of structure at event 3 on test day 7

The time response shows that the structure is fairly quiet until a sudden impulsive response is observed at all the accelerometers on the structure. The accelerometer on the ceiling did not detect such a sudden impulsive behavior and hence is not shown. The time response displays characteristics of a structural response due to a broadband disturbance. The response is multi-mode in nature and the disturbance was felt globally. The higher frequency vibrations damp out rapidly and trailing lower frequency response remains. Such a response is typical of the system response due to thermal creak as seen in Chapter 2.

The spectrogram of these responses are shown in Figure 4.26 to observe the time dependent frequency response. The spectrogram also supports that the response is multi-mode in
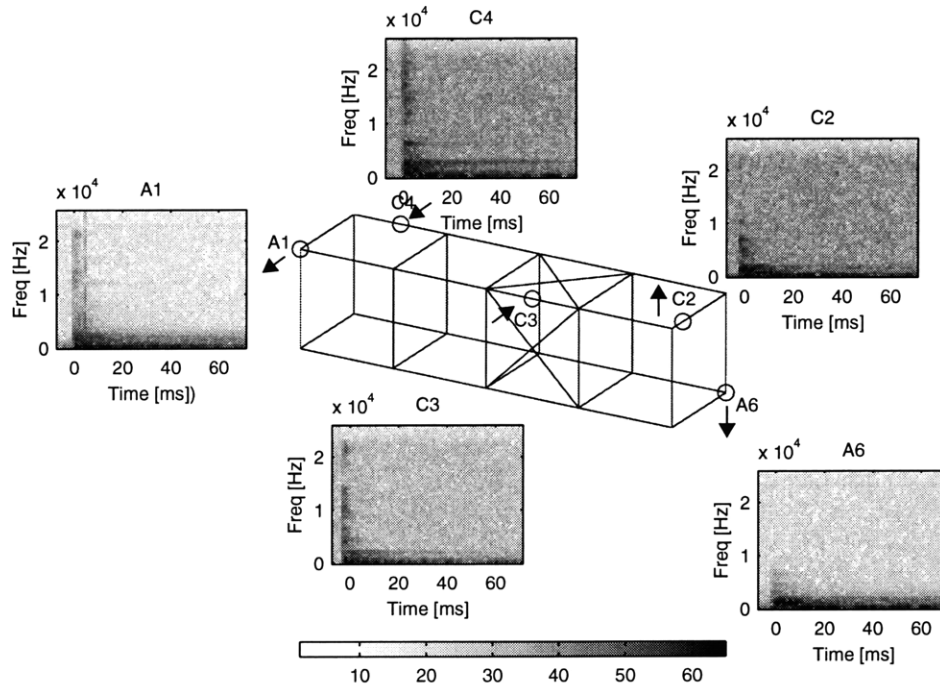
Figure 4.26 Spectrogram of structural response at event 3 on test day 7

nature. The dominant frequencies for this event at different locations are 3 kHz, 6 kHz, and 9 kHz.

Both the time and the frequency response indicate that the high frequency vibrations are dominant in the accelerometers located at the middle of the struts (C3, C4). These accelerometers pick up mostly higher modes or local modes of the structure. The accelerometers near the end of the structure (A1, A6, C2) sense mostly smaller magnitude, lower frequency vibrations. Global modes evidently dominate the response at these locations.

The general location of the creak source can be inferred by comparing the magnitudes and the frequency content in the response. Recall that higher frequency dominates near the source and the high frequency content is filtered as the disturbance propagates away from the source due to the dispersive effects of the medium and the joints. The joints effectively act as a high pass filter [28]. Thus, the sensor detecting the largest magnitude is assumed

to be the nearest site of the creak source. For this event, the creak source is likely to be between sensors C3 and C4 [Figure 4.25].

The initial response detected by the accelerometers are plotted in Figure 4.27 to investigate the disturbance propagation. The signals from the accelerometers C4 and A1 were fed into a different Tektronix unit with a different trigger signal, and thus they are not plotted. Note that the disturbance was first sensed by C3. Recall that the acceleration at C3 had the highest frequency content. These characteristics reinforce that the creak source was closest to C3.

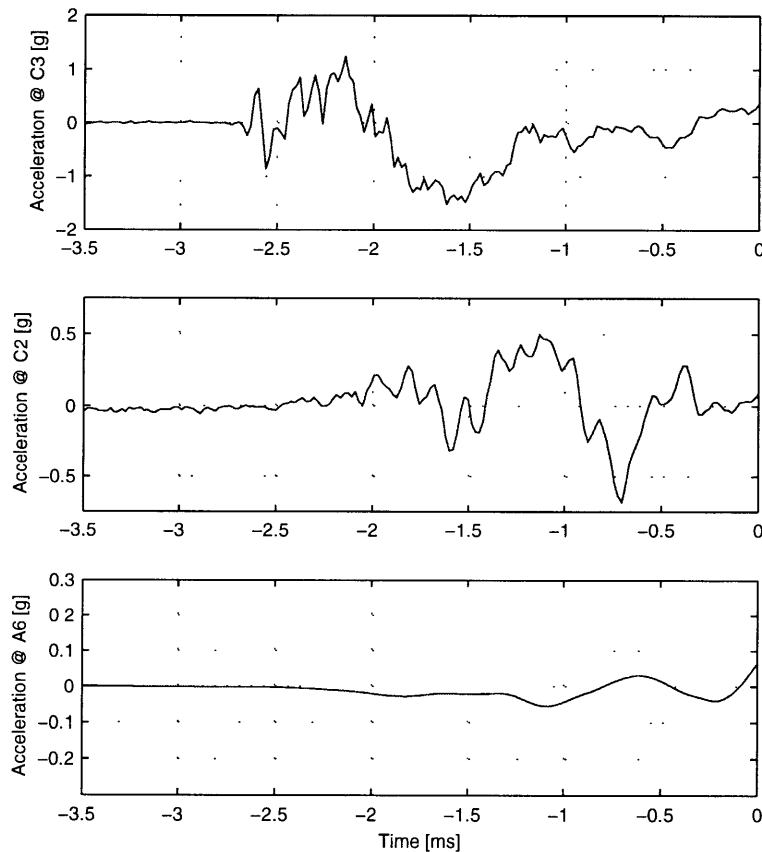

Figure 4.27 Disturbance propagation for event 4 on test day 7

The response of the truss varied from event to event in terms of frequency content and shape of the time response. Such variation implies that the creak source varied from event

to event. The accelerations at the same location from different events were compared to search for a similar response to identify a common creak source between events. Such common creak source was indicative in the results from test day 7. Figure 4.24 shows that a series of successive events were observed during the second cooling period of the cycle. These successive events are plotted in Figure 4.28. Each row shows the time response at the location of the sensor shown in Figure 4.25. Note that the response at each sensor location is very similar for all of these events. Such similarity was found among these events only. No such correlation was found in any other test data or with the other data. This behavior suggests that the same creak source was triggered for these successive events. The magnitude of the response is largest for the first creak and the magnitude decreases with each event. Such a trend was observed in the joint characterization experiment, where the large amplitude slips only occurred in the initial slips and a variation in smaller magnitude slips followed.

The temperature history shows that the time between these successive events increased. Such time dependence in creak frequency was demonstrated by the model in Chapter 2. The magnitude at each slip was constant in the model result.

Radiative tests

The data from test day number eight are investigated in this section. The first setup where the shroud was used for thermal loading was used. The thermal response of the truss structure along with the shroud temperatures are shown in Figure 4.29. The dotted vertical line indicates the time of an event occurrence. The temperature distribution of the structure is not uniform. Only one event was detected during this test day.

The dynamic response of the structure is presented in Figure 4.30. The corresponding spectrogram is plotted in Figure 4.31. Note that only one accelerometer detected the disturbance. Further, the high frequency response dominates the response. The disturbance was felt locally, presumably very close to the source, thus suggesting that the wave propa-
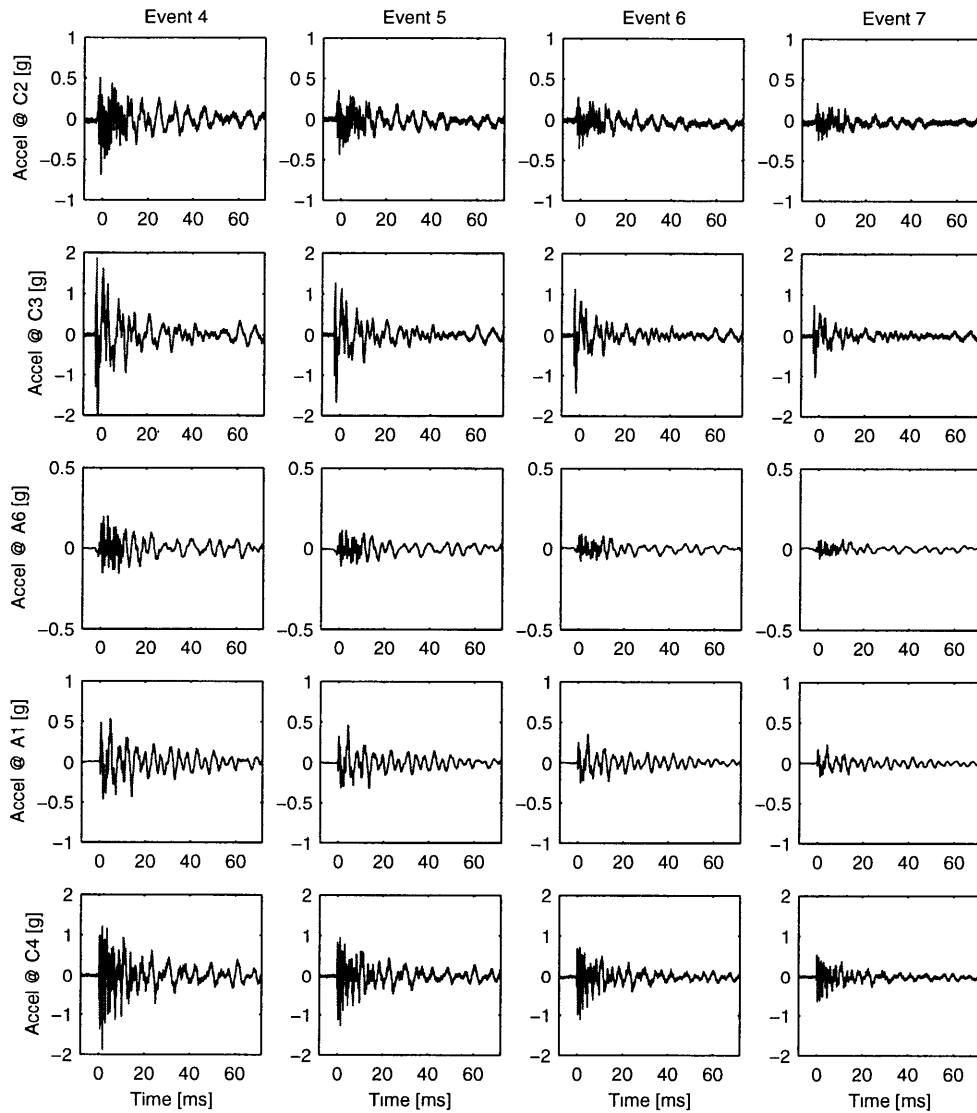
Figure 4.28 Series of successive events on test day 7

gation dominates the response. It is also possible that the lower frequency response may have been washed out by the relatively large noise level.

The results from the convection tests showed that the high frequency response has significantly damped out when it reached the end of the truss from the possible creak source. The dominant frequencies seen in this event are above 10 kHz, which is an order of magnitude higher than those observed during the convection tests. As a results, disturbance
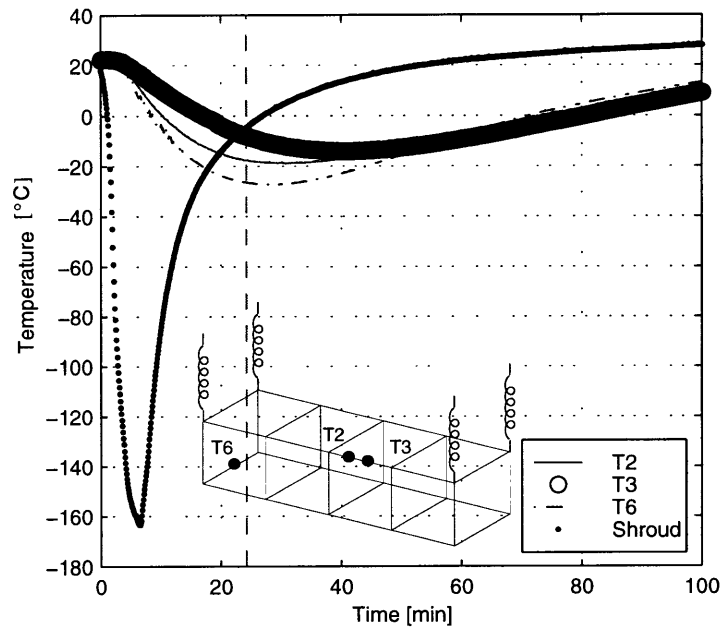
Figure 4.29 Temperature history for test day 8
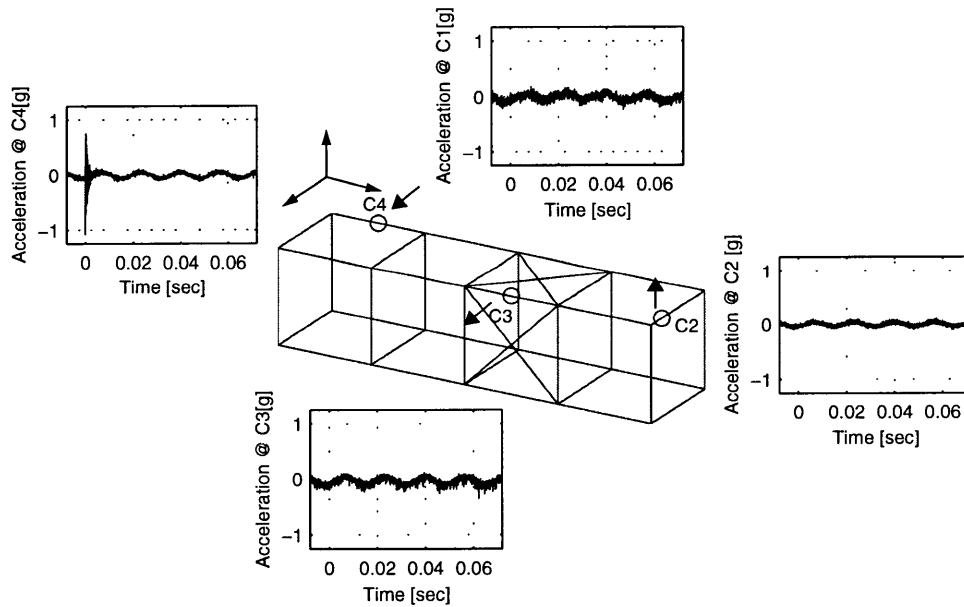
Figure 4.30 Time response of structure at event 1 on test day 8
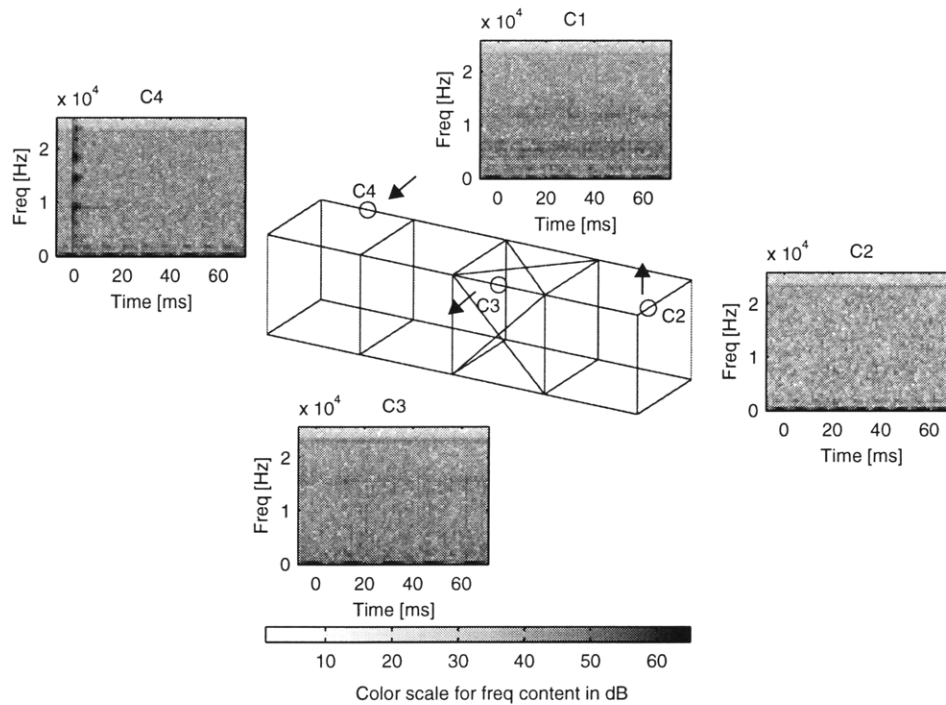
Figure 4.31 Spectrogram of event 1 on test day 6

may have never reached the other sensors or the energy has considerably dissipated such that the magnitude is lower than the noise level. To investigate the propagation of high frequency vibration, the convection test data (9/29) were filtered using a butterworth high pass filter with the cutoff frequency of 10kHz [Figure 4.32]. The locations of sensors C2, C3, and C4 remained the same in both test days 5 and 6. The filtered data at C2 show that the amplitude of the acceleration has significantly attenuated. Thus even if the high frequency waves reached the other sensors, the signal is swamped by the chamber noise.

Summary of events

The total number of events observed during the tests are summarized in Figure 4.33. The thermal load profile was not identical for all the tests but they were very similar as mentioned in Chapter 3. Note that the number of events observed varied from test day to test day.
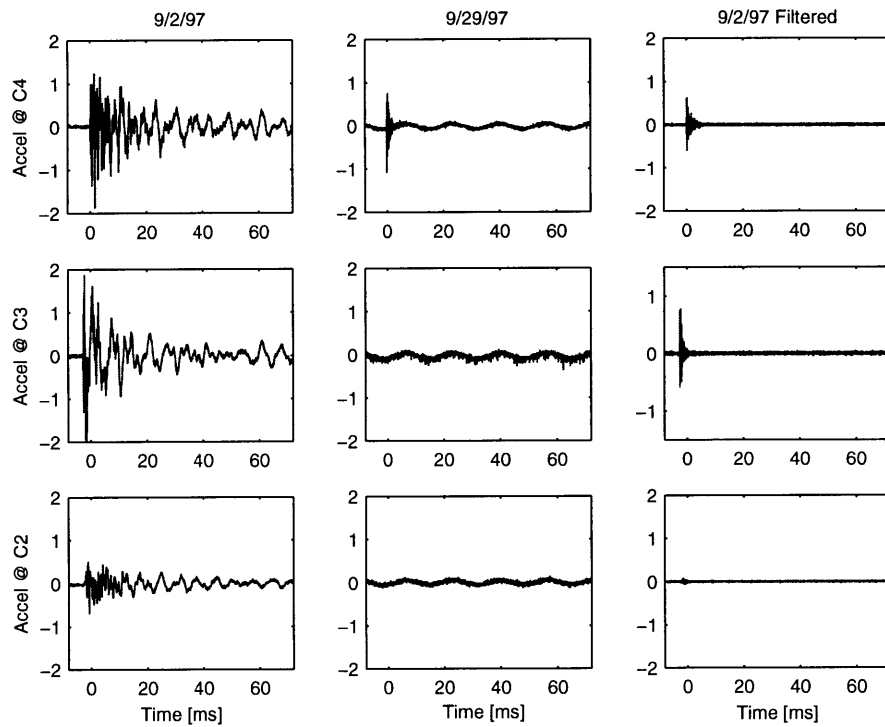
Figure 4.32 Filtered data vs. actual data
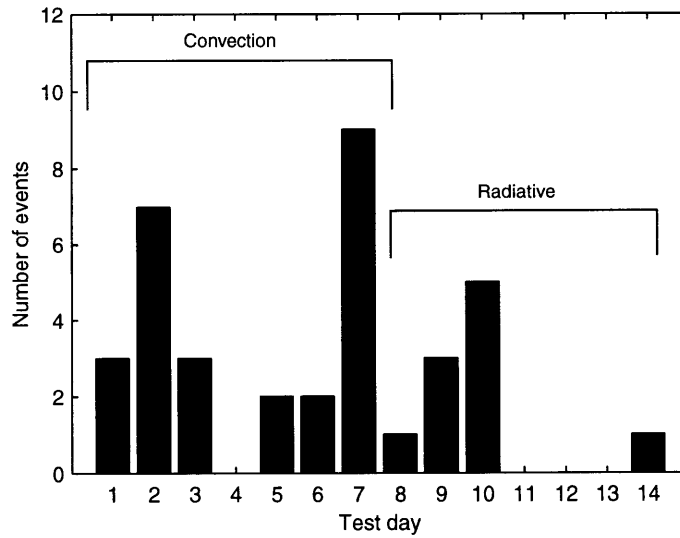
Figure 4.33 Number of snap events observed

Overall, more events were observed during the convection tests than the radiative tests. The turbulent air that caused the bouncing motion of the truss may have contributed to the

increase in the frequency of the snap events. In addition, the loading rate in the convection tests were higher than that of the radiative tests. The structure attained a ΔT of -40 °C in 50 minutes as opposed to 120 minutes in the radiative tests.

These different loading conditions affect the friction behavior, and hence the characteristics of the dynamic response during the convection tests varied from that during the radiative tests. The convection test results showed that 1) the disturbance was propagated throughout the structure, 2) frequency was mostly in the one kHz range and 3) the magnitudes of the events ranged from 0.01 g to 1 g. The radiative test results indicated that 1) the disturbance was felt locally, 2) the frequency content was mostly in the 10kHz range and 3) the corresponding magnitude ranged up to 20 g. In all of the radiative tests, events were detected only at one location. For more details on the thermal creak characterization in the frequency and time domain, see [37].

In general, different events showed different magnitudes and frequency content as a result of varying creak sources and varying creak response. Variation in creak response was observed in the joint characterization test. Recall that such scatter is attributed to the friction, loading rate, and environment. For the thermal tests, similar variation was encountered. The tests were conducted over a period of six months. As seen in the joint tests, the friction parameters varied with time. The effect of cooling and heating rate on thermal snap occurrence, and the effects of temperature, vacuum, and external mechanical disturbance on friction behavior are unknown. Sources of experimental error are discussed in depth in [37].

4.2.4 Model correlation

A qualitative correlation between the experimental data and the model results is presented in this section. The data from test day 7 are used for the model correlation . Recall that the dominant frequencies for the events on this day were 3kHz, 6kHz, and 9kHz. These frequencies approximately correspond to the longeron axial modes. As a result, the creak source is assumed to be the pin joint slipping in axial direction. Further, the results indi-

cated that the creak location was most likely to be between sensors C4 and C3 based on the relative magnitudes of the response [Figure 4.25]. Based on this inspection, the location was assumed to be one of the pin-clevis joints in the first bay.

The acceleration data were filtered to observe the response in the frequency range of the model, namely 1400-3000 Hz. A fifth order Butterworth bandpass was used to filter the data. The correlation is presented in Figure 4.34. Note that the accelerometers C2, A1, and A6 were measuring acceleration in the transverse direction. However, the longitudinal vibrations are detectable due to the poisson effect. In the model, the characteristic length was approximated to be $x_1^* = 2 \times 10^{-6}$ m (to match the amplitude of the vibrations obtained from the data) due to the lack of data on the friction mechanism.

The results show that the model qualitatively captures the behavior. The shape of the response match well. The model however exhibits a higher frequency content. The frequencies do not match due to the modeling error in the finite element model and the reduction of the bay dynamics to the dynamic creak element.

The discrepancies between the model and the data could also be due to the assumptions about the location of the creak source. Further, the dynamics model does not capture the wave propagation characteristics. The attenuation of the signal away from the source is not apparent in the model results. Finally, despite the fact that the MODE truss is a non-linear structure, a linear finite element model was used to model the dynamics of the structure.

Sensitivity analysis

To qualitatively investigate the effect of the parameters on the response, the parameters f_k, κ, and μ were deviated from the nominal values shown in Table 4.4. The assumed creak location was also varied as a parameter. Only one parameter was varied from the nominal value while the others retained the nominal values.
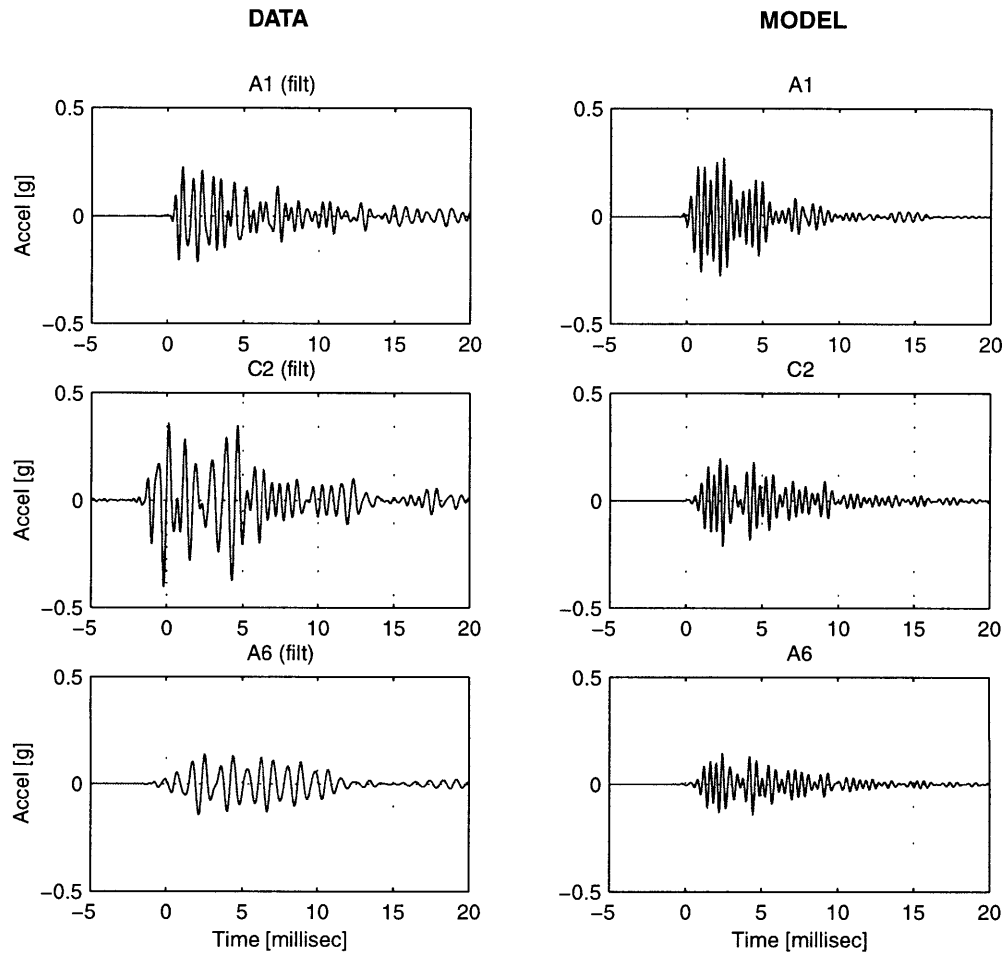
Figure 4.34 Model correlation for event 4 on test day 7

Recall that the magnitude of the disturbance is proportional to the quantity $2(1-f_k)$ for the dynamic creak element [Eq. (2.55)]. The percent change in the magnitude of the response is proportional to the percent change in the quantity $2(1-f_k)$. The shape of the response, however, was unaffected by f_k. A small variation in the mass ratio μ, up to approximately 20% change, induced a small change in the shape and the magnitude of the response. As the mass ratio significantly deviated from the nominal value, the shape of the response also deviated from those shown in Figure 4.34. For $\mu < 0.14$, the shape of the envelope and the magnitude remains unchanged. The response was more sensitive to an increase in the mass ratio than a decrease in the mass ratio. The magnitude of the response was relatively insensitive to decrease in stiffness ratio κ and the shape of the responses

was sensitive to κ. Changes in the number of peaks in the envelope as well as the shift in the peaks were observed, indicating that different modes were being excited. For a value as low as κ = 1.5, the magnitude of the largest peak in the response of A1 decreased by 20%. However, the magnitude was significantly decreased as κ increased.

Finally, the creak location was varied. The magnitude of the response was relatively insensitive to the creak location. The relative magnitude among the sensors varied for different creak locations as expected. The general shape of the responses varied significantly as the creak location varied, again indicating that different modes were being excited.

In summary, the magnitude of the response was most sensitive to the change in f_k. The change in the magnitude was linearly proportional to $2(1-f_k)$. The magnitude of the response was linearly proportional to x_1^* because the static contribution $\Delta\xi$ in Eq. (2.62) dominated the creak response. The dynamic response of the creak element was a higher order effect and as a result, any change in its mass ratio μ had a minimal effect on the magnitude of the system response. The shapes of the responses were quite sensitive to κ and the creak location. As discussed in Section 2.3.1, the time between the slip initiation and the slip termination points were functions of μ and κ. Varying these parameters affected this time difference between the two successive step forces. As a result, different modes were excited and a different mode mix resulted.

Experimental errors

Some measurement errors are introduced due to the limitations of the hardware implemented in the experiment. The most severe is that the accelerometers of type A have a bandwidth of 0-500 Hz. These accelerometers can measure, in practice, events with a frequency content higher than 500 Hz. However, the magnitude will not be accurate and only qualitative comparisons have meaning. Most of the events observed in the experiment displayed a frequency content of 1000 Hz and higher. For the higher bandwidth accelerometers, type C, the accuracy in the amplitude of the vibrations decreases for frequencies of 8000 Hz and higher. Thus even these accelerometers inaccurately measured the high fre-

quency events seen in the radiative tests. The possibility of accelerometer resonance was not a concern because of the multi-modal nature of the events.

Some events may have been missed due to the limitations of the data acquisition system and a relatively large noise level. Randomly selecting a trigger accelerometer may have caused some events to be missed. Lower frequency content of an event could not be measured due to the high bandwidth setting on the data acquisition system. As a result, no further information on the low frequency vibrations were extracted. Further, any event whose magnitude is less than the noise level could have not been detected. In the convection tests, the noise level was not a serious problem. During the radiative tests, however, relatively high noise level was encountered. Due to the bandwidth limitations of the accelerometers and the data acquisition system, some error in the measurement of the frequencies are expected for the higher frequencies. Thus, miscellaneous errors due to the electronics and sensors were not important in this context.

Initial conditions for the MODE experiment were duplicated to a certain extent. The exact procedure of deployment was not repeated at every test run. As a result, some joints may be at a more likely initial condition to slip than others. Such variation in the initial condition introduced the randomness in the types of the events observed in the experiment. The thermal loading profile was not identical for each test run. The thermal cycle began with either a heating or a cooling period. As seen in the joint characterization experiment, the loading history affects the creak response. Thus, the variation in the number of events and event types may be a result of the variation in the thermal load histories.

Despite the possibly large errors in the magnitudes measured by the accelerometers, the relative magnitudes between the accelerometers and the events were accurate. Further, these data indicate that events did occur and a qualitative correlation is valid.

4.2.5 Summary

In summary, thermal creak events were demonstrated in a representative deployable truss structure. The results provided strong evidence that these events were thermally-induced. The behavior seen in the experiment qualitatively agreed with the main characteristics predicted by the model. The events were observed only during the thermal transients. The events occurred after the stresses had built up to a critical level. The repeated events of the same creak source was observed. The decrease in the creak frequency with decreasing thermal loading rate was clear as demonstrated in Chapter 2. The dynamic response was that of an impulsive broadband disturbance, where many modes in a system were excited.

The response exhibited some wave propagation characteristics. The attenuation of the vibrations away from the apparent creak source location was displayed. The high frequency vibrations did not propagate well due to the relatively rigid joints and viscoelastic effect in the structure. The model capabilities are limited by the finite element model and the conventional structural dynamics analysis.

Chapter 5

FLIGHT EXPERIMENT

The Interferometry Program Experiment (IPEX) II is a flight experiment conducted during the STS-85 shuttle mission in August 1997. The experiment was designed by researchers at the Jet Propulsion Laboratory (JPL) to investigate the microdynamic disturbances in deployable truss structures including thermal creak. Ref [40] contains a detailed description of the experiment and the results. In this chapter, a brief description of the experiment is provided and selected results from the flight experiment are used for qualitative model correlation. The capabilities and the limitations of the model are discussed based on the results.

5.1 Experiment description

5.1.1 Test article

The test article for the experiment is a nine-bay deployable truss structure, whose dimensions are 2.3 m x 0.3 m x 0.3 m. A schematic drawing of the truss is shown in Figure 5.1. The truss consists of graphite longerons, graphite battens, and steel cable diagonals. The structure is preloaded at approximately 1780 N (400 lb) in the longerons. A pulley mechanism in the center of the cable diagonals provides the deployment and preloading mechanism [Figure 5.2]. The end fittings of the longeron and batten struts are stainless steel balls [Figure 5.3]. The ball joints sit in stainless steel spherical sockets. These mechanisms and the joints are potential creak sources.
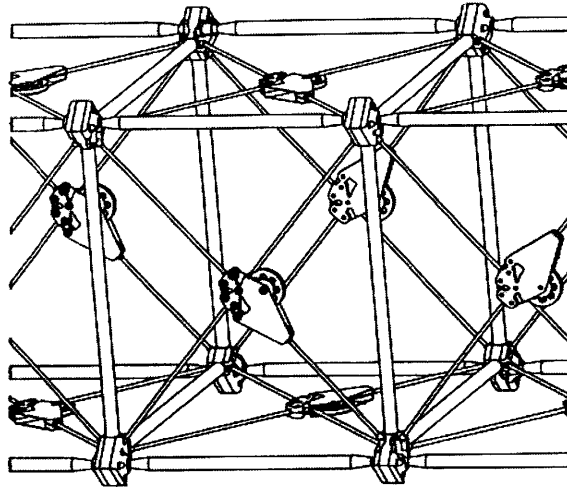
Figure 5.1 A section of IPEX deployable truss
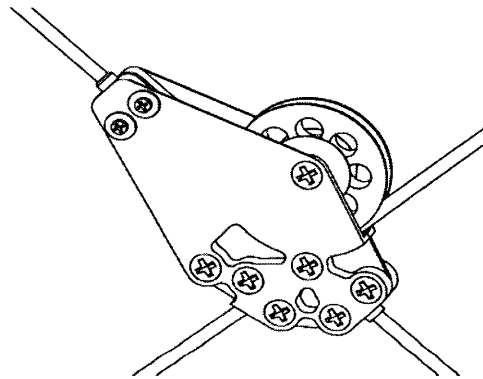
Figure 5.2 Cable pulley mechanism

The material properties and the dimensions of the truss elements are listed in Table 5.1. Under uniform thermal loading, the CTE mismatch in this statically indeterminate structure will induce thermal stresses in the truss elements. The stresses are computed based on the equilibrium, constitutive, and compatibility relations for the system. Details on the static model of the truss are presented in Section 5.1.3. A change in the internal forces of $9.2 \text{ N/}^{\circ}\text{C}$, $10.3 \text{ N/}^{\circ}\text{C}$, and $-6.9 \text{ N/}^{\circ}\text{C}$ are developed in the longeron, batten, and the diagonal, respectively, where a positive force indicates tension. Consequently, the preload in the structure decreases with increasing temperature until the cable slackens at approximately $\Delta T = 194^{\circ}\text{C}$.
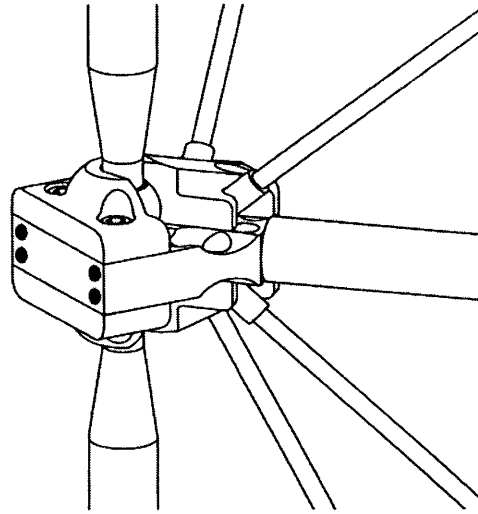
Figure 5.3 Ball joint assembly

TABLE 5.1 Material properties of the IPEX II truss elements

Material properties	Longeron	Batten	Diagonal
E [N/m^2]	2.34×10^{11}	2.34×10^{11}	5.62×10^{10}
α [°C^{-1}]	-4.3×10^{-7}	-8.55×10^{-7}	1.53×10^{-5}
ρ [kg/m^3]	1605	1605	7900
l [m]	0.26	0.29	0.39
d [m]	0.0116	0.0116	3.175×10^{-3}

5.1.2 Test environment and instrumentation

The IPEX truss was cantilevered off the side of a free flying spacecraft ASTRO-SPAS (A/S) [Figure 5.4]. The A/S was deployed from the space shuttle. The experiment was conducted under many different operation modes of A/S. One of the operation modes was a quiescent mode where all the thrusters, gyros and other instrumentations on A/S were turned off. This quiescent period lasted five minutes. This chapter focuses on the data from this quiescent period.

During the quiescent mode, the A/S and IPEX truss were suddenly exposed to sunlight as the platform exited the Earth's shadow. The orientation of A/S was inertially fixed such that the solar vector is at 45 degrees off of the negative x-axis of A/S [Figure 5.4]. The solar vector lies in the A/S x-z plane. As a result, the solar heating of the truss is relatively uniform and shadowing effects between the members are minimal.

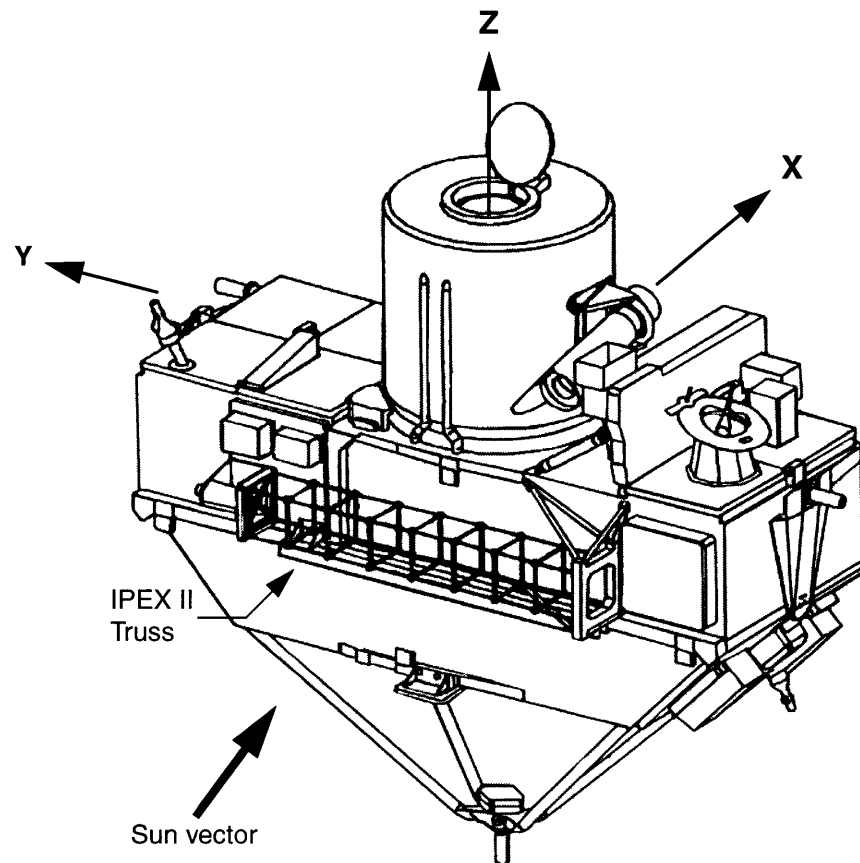**Figure 5.4** Orientation of the solar vector relative to IPEX and A/S

The truss was equipped with the following sensors: 1) micro-g accelerometers to measure microdynamic vibrations, 2) temperature sensors to measure the temperature distribution of the truss, and 3) loadcells. The accelerometers were mounted on the joint assembly and the pulley assembly. The locations of the accelerometers are shown in Figure 5.5.
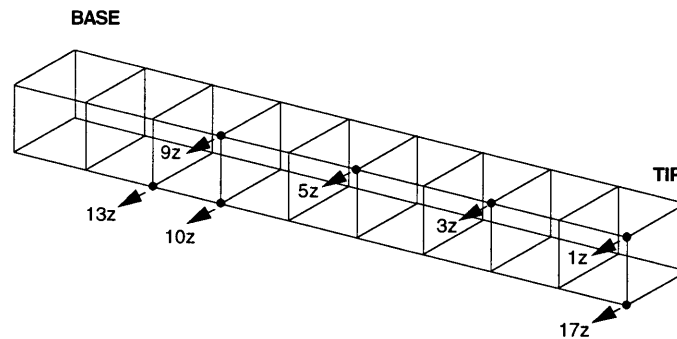
Figure 5.5 IPEX accelerometer map

The thermal sensors were collocated with the accelerometers inside the accelerometer casing. Three thermal sensors were embedded in the struts. The data were recorded for the entire five minute period at a sampling rate of 1 kHz.

5.1.3 Model description

Thermal model

Simple thermal analysis of the IPEX truss is performed to assess the experimental data and qualitatively characterize the temperature distribution of the truss. The heat load on the truss is first computed based on the orientation of the truss relative to the sun vector. As mentioned earlier, the truss is at a fixed orientation in inertial space. Because the test period was relatively short compared to the orbit period, the earth and the albedo heating are assumed to be constant. The following additional assumptions are made in the thermal analysis.

1. Radiative heat transfer between the truss and A/S is negligible
2. Radiative heat transfer between the members are negligible.
3. Inter-member shadowing effect is negligible.
4. Conduction is negligible.

Based on these assumptions the strut, the cable, and the joint assembly average temperatures were computed using the lumped mass analysis. The joint assembly is assumed to be a block with dimensions of 0.012m x 0.012m x 0.019m. The thermal properties of the

truss material and the heat load parameters are shown in Table 5.2 and Table 5.3, respectively.

TABLE 5.2 Thermal properties of the IPEX II truss elements

Thermal properties	Gr/Ep	Stainless Steel
C_p [J/kg-K]	880	502
α_s	0.97	0.4
ε	0.86	0.12

TABLE 5.3 Heat load parameters for IPEX II during quiescent mode

Solar flux [W/m^2]	1350
Albedo factor	0.2
Earth heating [W/m^2]	250
Earth view factor	0.4

Creak model

Similar to the MODE creak model, a creak source and a slip mechanism are hypothesized. The ball joint of the longeron in the first bay is assumed to be the creak source. The joint is assumed to slip in the transverse direction along the surface of the spherical cavity. The geometry of the first bay along with the slip mechanism is illustrated in Figure 5.6. The same approach described in the MODE truss modeling section is implemented to obtain the dynamic response of the IPEX truss. A finite element model of IPEX truss developed by Ingham [41] is used to obtain the stiffnesses and the modal masses for the creak element and the modeshapes and frequencies for the structural dynamics model. The model parameters are shown in Table 5.4.
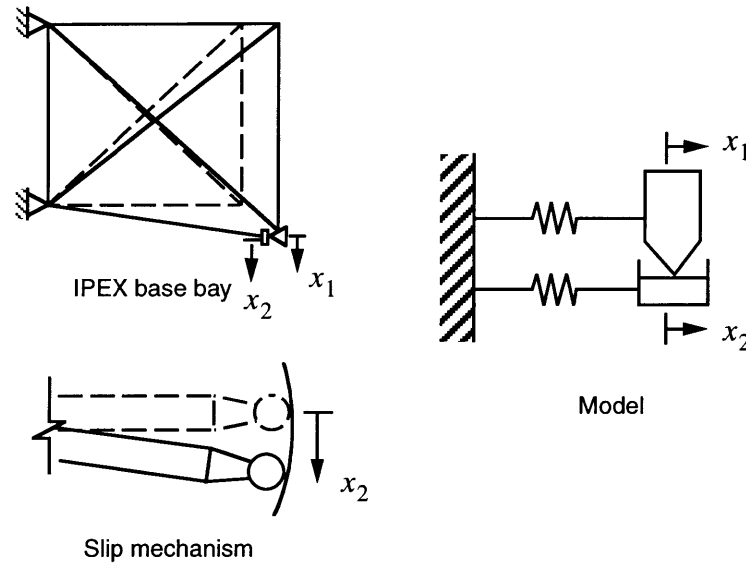
Figure 5.6 Assumed slip mode in IPEX

TABLE 5.4 Model parameters for IPEX

κ	0.5
α_r	0
μ	0.2
f_k	0.9

5.2 Results

5.2.1 Thermoelastic response

The temperature distribution of the truss is characterized in this section. The sunrise occurred at 40 seconds after the quiescent mode began. The steady state temperature of the truss just prior to existing the Earth's shadow was approximately -35 °C. The temperature distribution is plotted in Figure 5.7.

The total temperature change from sunrise to the end of the test are shown in Figure 5.8. Note that the thermal sensors collocated with the accelerometers measured a small temperature change compared to the sensors embedded in the struts. Table 5.5 presents the

corresponding temperature change that the strut and the joint experience. The results suggest that the thermal sensors on the pulley assembly and the joint assembly were following the local thermal state at the pulley and the joint assembly, and thus were not representative of the strut or the cable temperatures.
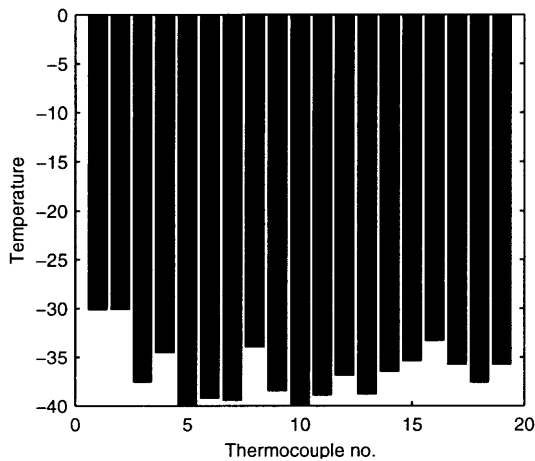
Figure 5.7 Steady temperature in shadow
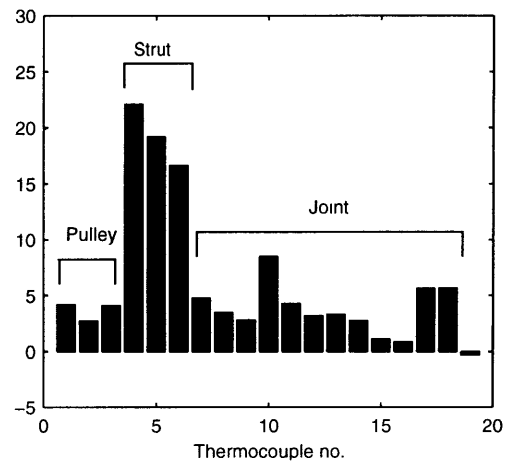
Figure 5.8 Temperature change during transition from shadow to sunrise

TABLE 5.5 Model results of temperature change during transition from shadow to 260 seconds after sunrise

Truss component	ΔT [$^\circ$C]
Strut	22
Cable	15
Joint assembly	5

Because the CTE of the strut is extremely low relative to the cable CTE, the thermal response of the strut has a negligible effect on the thermoelastic response of the truss. Thus, the thermal response of the cable governs the thermoelastic response. The cable temperature computed from the thermal analysis is used to obtain the thermoelastic response because the temperature data from the thermal sensors on the pulley assembly are not good representative of the thermal state of the cable.

The good agreement between the model and the data suggests that the analytical result for the cable thermal response is a good approximation. Note that the cable experiences a significant temperature change during the test. Such a thermal response is large enough to induce stresses that can cause creak in the structure. The internal forces in the longeron change by approximately 140 N. While in the shadow, the preload in the longeron has increased by 550 N due to the significant temperature drop. Thus it is likely that many snap events occurred prior to the quiescent period.

5.2.2 Dynamic response

The flight data during the quiescent period showed that creak events were ubiquitous. A preliminary characterization of the dynamic response are presented in [40]. The events included discrete global structural modes with relatively large magnitudes. Some high frequency with lower magnitude events were observed. As seen in the parametric study in Chapter 2, a range of structural behavior was possible depending on the exact parameters. The IPEX truss contained many possible creak sources and slip modes, such that a wide range of behavior is expected. The flight data analysis is an on-going project and thus a preliminary model correlation is presented in this section.

An event that occurred at 54.7 seconds into the quiescent period is selected to compare to the model results. The dominant frequency content is in the 200-300 Hz range for this event. The model results and the filtered data are presented in Figure 5.8. The data were filtered using a Butterworth bandpass between 200 and 300 Hz. In the model results, the characteristic length was chosen to be $x_1^* = 5 \times 10^{-8}$ m to match the magnitudes of the data.

The data and the model agree qualitatively well. Similar to the results seen in the MODE convection tests, the disturbance was felt throughout the structure. The frequency content agrees well, suggesting that the assumed slip mode is a good approximation. Note that the shape of the response near the base, (13z, 10z, and 9z) shows a better correlation with the model than the response away from the base. The disagreement is attributed to the
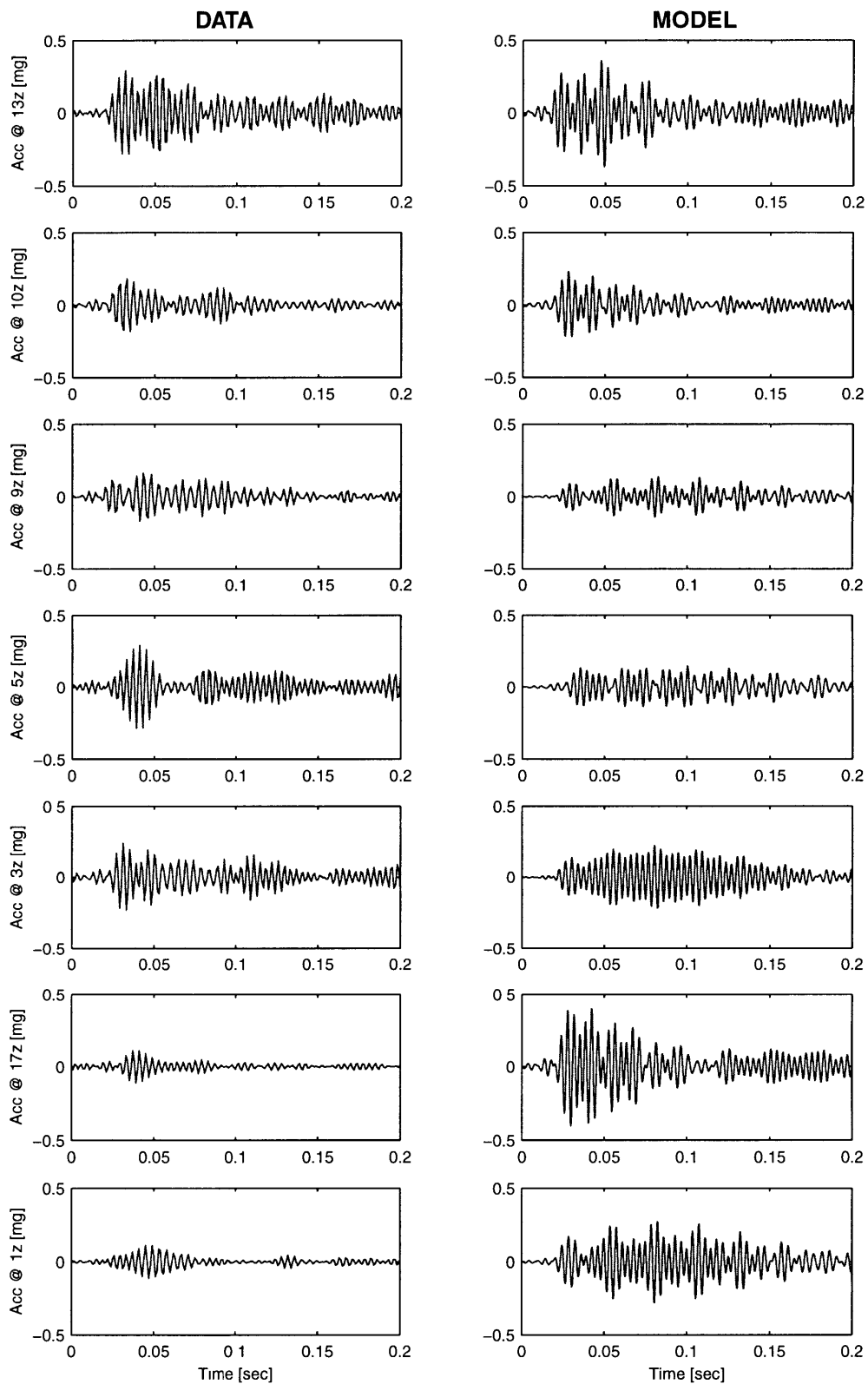
Figure 5.9   IPEX model correlation for creak event at t=54.7sec

assumed location of the creak source and the reduction of the base bay to a single DOF system.

Sensitivity analysis

Similar to the results seen in the sensitivity analysis for MODE, the key nondimensional parameters were varied to qualitatively understand the effect of the parameters on the system response. As seen in the case with the MODE, the change in the magnitude of the response was proportional to the change in the quantity $2(1-f_k)$. Unlike the MODE case, the system response was not sensitive to the change in the mass ratio μ. The mass ratio was varied up to $\mu = 0.2$, an order of magnitude larger from the nominal value, and the response was only slightly affected both in magnitude and in the shape. The stiffness ratio κ had a small effect on the shape of the response. For decreasing values of κ, the magnitude of the response was also insensitive to the change in the stiffness ratio. For increasing values of κ, the magnitude decreased noticeably. As an example, for a stiffness ratio $\kappa = 0.1$, the upper bound on the magnitude was approximately the same. For $\kappa = 5$ the bound on the magnitude was 50% lower than the nominal value. The creak location caused a slight change in the magnitude of the response. Depending on the locations, the shape of the response remained approximately the same. Some locations, however, did significantly alter the shape from the nominal result.

The dynamic response of IPEX was less sensitive to the changes in the parameters than that of MODE. The friction parameters have a same effect on the magnitude of the response as expected. The response is most sensitive to the change in these parameters. However, the response was fairly insensitive to the changes in the mass ratio μ and the stiffness ratio κ. The creak location affected the shape of the response the most as seen in the MODE results. In conclusion, a sensitivity analysis for each structure is necessary because the result is structure specific and is not necessarily dependent on the parameters.

Experimental errors

The type of experimental errors encountered in the tests with the MODE truss were not of concern for the IPEX truss. Some of the electronic noises were identified. Unlike the MODE thermal creak events, events observed in the IPEX data were in the range of the specification of the accelerometers. Further, the data were recorded throughout the entire period of the experiment to minimize the possibility of missing events. Thus, the use of the model for a qualitative correlation is valid.

Chapter 6

CONCLUDING REMARKS

The primary objective of the thesis was to investigate the phenomenon of thermal creak, as motivated by the design needs of precision space structures such as interferometers. In this chapter, the thesis is summarized by reviewing the contributions and discussing the recommendations for future work.

6.1 Contributions and conclusions

The primary contribution lies in thermally induced disturbance characterization. Both analytical and experimental investigations in thermal creak induced dynamics were initiated for the first time.

(i) A general framework for thermal creak modeling was developed. The model provided an insight to a qualitative understanding of the mechanisms of thermal creak. Based on the understanding of the thermal creak mechanism, the potential creak sources and the possibility of creak events under various thermal loading conditions for a variety of structures can be identified and evaluated.

(ii) The creak model can be used as a tool to aid in developing thermal creak mitigation strategies. The model pointed out the key parameters that dictate the creak response and the resulting dynamic response of the structure. The magnitude, the creak frequency and

the frequency content strongly depend on the thermal strain mismatch parameter, the friction parameters, and the thermal loading condition.

(iii) A complex nonlinear mechanism was reduced to a simple model to aid in design analyses of precision space structures. The creak model is generic enough that it can be applied to any type of a structure for material, component, and system level creaks. Further, the model is simple enough that many creak models can be used to explore the effects of the different creak sources and locations in a complex structure and parametrically bound the problem.

(iv) Despite the fact that thermal creak is a disturbance internal to the system, the model allows the nonlinear response to be modeled as an external force to approximate the disturbance. The modeling approach illustrated in the thesis allows a nonlinear mechanism to be decoupled from the linear structural response and exploit already existing linear structural models.

(v) A simple experiment validated the mechanisms that cause thermal creak. The experiment revealed additional parameters that affect the response, not predicted by the model. The stiffness of the system and the loading rate may significantly alter the creak response predicted by the model. The role of friction and the limitations of Coulombic friction model in thermal creak were established.

(vi) Thermal creak in a deployable structure was demonstrated for the first time in a controlled environment. First direct measurements of thermal creak events in a real space structure were obtained. Various ranges of behavior were observed as the model predicted. The dynamic response was in a qualitative agreement with the model prediction.

(vii) The analytical and the experimental work of the thesis was a useful input to the design of the flight experiment. This experiment was the first direct deliberate observation of thermal creak in space. The flight experiment was a further demonstration that thermal creak is a problem.

(viii) The development of the analytical tools and the lessons learned from the experimental investigation contribute to an analysis technique for thermal creak prediction and assessments. The analytical work can be formalized into a guideline for analyzing thermal creak disturbance for preliminary spacecraft design.

6.2 Recommendations for future work

Thermal creak modeling

In the thermal creak model, several simplifying assumptions were made. The experimental data indicated that some of these assumptions may be contributing to the discrepancies between the model and the data. First of all, an extended friction model may improve the correlation between the model and the data. The effects of temperature and vacuum on friction mechanism should be investigated. Based on the literature and experimental data, the stiffness of the system and the loading rate affect the friction behavior and may need to be incorporated in a dynamic friction model to obtain a better prediction of creak response magnitudes. The joint characterization tests displayed memory dependency in the response. Memory effects such as dependence on the loading history and the initial conditions should be investigated analytically and experimentally.

In determining the dynamic response, a conventional structural dynamics model was implemented for convenience. However, because thermal creak is a broadband disturbance, high frequency local modes of the structure are likely to be excited. These high frequency modes are not well captured by the conventional structural dynamics models. Wave propagation models should be investigated to assess the trade-off between the model complexity and the gain in the accuracy of the model.

The thermal creak induced dynamic response was obtained by numerically integrating the equations of motion because the behavior is a transient response. Stochastic modeling for these transient disturbances may prove useful as an analysis technique for thermal creak characterization.

Thermal creak testing

The joint characterization tests revealed many aspects of friction behavior and other parameters that may affect the creak response. Simple component tests to extract friction parameters and to better model the nonlinear mechanisms are needed for thermal creak predictions.

The results from the thermal tests of the MODE truss were difficult to correlate with the model because of the multiple creak sources in the structure. A more controlled experiment, where the creak source is isolated may provide further understanding of the creak disturbance propagation throughout the structure. Because the experiment was an initial effort in demonstrating and identifying thermal creak events, the test matrix was not well structured. The thermal loads and the sensor locations varied from tests to tests. An identical experimental setup with a more complete and better designed test matrix may provide further insight into the identification of creak sources and hence improve the correlation between the model and the data. Finally, the flight experiment provided a significant amount of data yet to be analyzed. Further investigation of the flight data may provide a better understanding of the creak behavior and reveal the dominant effects of the space environment on thermal creak.

REFERENCES

[1] Kaplan, M., "Origins," presented at *Origins Technology Workshop*, Dana Point, CA., June 1996.

[2] Foster, C. L., Tinker, M. L., Nurre, G. S., and Till, W. A., "The Solar Array-Induced Disturbance of the Hubble Space Telescope Pointing System," *61st Shock and Vibration Symposium*, Oct. 1990.

[3] Bath, M., Introduction to Seismology, 2nd Ed., Birkhauser Verlag, Basel, 1979.

[4] McManus, H. L., "Control of Space Structure Thermal Deformation: An Overview," Smart Structures and Intelligent Systems, *Proceedings of the Meeting, The International Society of Optical Engineering*, Albuquerque, NM, Vol. 1917, Feb., 1993, pp.545-554.

[5] Mahaney, J. and Strode, K., "Fundamental Studies of Thermal-Structural Effects on Orbiting Trusses," AIAA Paper 82-650.

[6] Mahaney, J. and Thornton, E. A., "Self-Shadowing Effects on the Thermal-Structural Response of Orbiting Trusses," *Journal of Spacecraft and Rockets*, Vol. 24, No. 4, July-Aug., 1987, pp.342-348.

[7] Kim, Y. A., "Transient Thermo-Structural Analysis of an Insulated Space Structure," Master's Thesis, M.I.T., 1995.

[8] Ferri, A. A., "Modeling and Analysis of Nonlinear Sleeve Joints of Large Space Structures," *Journal of Spacecraft and Rockets*, Vol. 25, No.5, 1988, pp.354-360.

[9] Hertz, T. J. and Crawley, E. F., "Damping in Space Structure Joints," AIAA Paper 84-1039. May 1984.

[10] Onoda, J, Sano, T., and Minesugi, K., "Passive Vibration Suppression of Truss by Using Backlash," *Proceedings of the 34th AIAA/ASME/ASCE/AHS/ASC Structures, Structural Dynamics, and Materials Conference* (La Jolla, CA), AIAA paper 93-1549.

[11] Crawley, E. F., Sigler, J. L., van Schoor, M. C., and Gronet, M. J., "Prediction and Measurement of Damping in Hybrid Scaled Space Structure Models," SSL Paper 7-88.

[12] Dutson, J. D. and Folkman, S. L., "A Nonlinear Finite Element Model of a Truss Using Pinned Joints," *Proceedings of the 37th AIAA/ASME/ASCE/AHS/ASC Structures, Structural Dynamics and Materials Conference*, April 1996, AIAA

96-1408.

[13] Ferney, B. D. and Folkman, S. L., "Results of Force-State Mapping Tests to Characterize Struts Using Pinned Joints," *Proceedings of the 36th AIAA/ASME/ASCE/ AHS/ASC Structures, Structural Dynamics and Materials Conference*, April 1995, AIAA 95-1150.

[14] Folkman, S. L., Rowsell, E. A., and Ferney, G. R., "Influence of Pinned Joints on Damping and Dynamic Behavior of a Truss," *Journal of Guidance and Control, and Dynamics*, Vol. 18, No. 6, Nov.-Dec. 1995, pp.1398-1403.

[15] Masters, B., "Multi-Degree of Freedom Force-State Component Identification,"Master's Thesis, M.I.T., 1993.

[16] Lake, M. S., Warren, P. A., and Peterson, L. D., "A Revolute Joint with Linear Load-Displacement Response for Precision Deployable Structures," *Proceedings of the 37th AIAA/ASME/ASCE/AHS/ASC Structures, Structural Dynamics and Materials Conference*, April 1996, AIAA 96-1500.

[17] Srinivasan, A. V., "Dynamic Friction," Large Space Structures: Dynamics and Control, edited by Atluri, S. N. and A. K. Amos, Springer-Verlag, Heidelberg, Germany, 1988, pp.179-194.

[18] Crawley, E. F. and O'Donnell, K. J., "Force-State Mapping Identification of Nonlinear Joints," *AIAA Journal*, Vol. 25, No.7, July, 1987.

[19] Bullock, S. J. and Peterson, L. D. , "Nonlinear Micron-Level Mechanics of a Precision Deployable Space Structure Joint," *Proceedings of the 37th AIAA/ASME/ ASCE/AHS/ASC Structures, Structural Dynamics and Materials Conference*, April 1996, AIAA 96-1333.

[20] Armstrong-Helouvry, B., Dupont, P., and Canudas de Wit, C., "A Survery of Models, Analysis Tools, and Compensation Methods for the Control of Machines with Friction," *Automatica*, Vol. 30, No. 7, 1994, pp.1083-1138.

[21] Bowden, M. L., "Dynamics of Space Structures With Nonlinear Joints," Ph.D Thesis, M.I.T., 1988.

[22] Webster, M., "Modeling BeamLike Space Trusses With Nonlinear Joints With Application to Control," PhD Thesis, Dept. of Aeronautics and Astronautics, M.I.T., 1991.

[23] Wang, Y., "Frequency Response Characteristics of a Revolute Impact Pair," *Nonlinear Vibrations*, Vol. 54, 1993, pp.171-178.

[24] Kim, Y. A. and McManus, H., "Thermally induced vibrations of space structures,"

presented at *Thermal Stresses 96.*

[25] Boley, B. A., and Wiener, J. H., Theory of Thermal Stresses, Robert E. Krieger Publishing Company, Inc., Malabar, 1985.

[26] von Flotow, A.H., "The Acoustic Limit of Control of Structural Dynamics," Large Space Structures: Dynamics and Control, S.N. Alturi, A.K. Amos (Eds.), Springer-Verlag, Heidelberg, Germany, 1988.

[27] Zak, M., "Dynamical Response to Pulse Excitations in Large Space Structures," Large Space Structures: Dynamics and Control, S.N. Alturi, A.K. Amos (Eds.), Springer-Verlag, Heidelberg, Germany, 1988.

[28] Doyle, J. F., Wave Propagation in Structures: An FFT-Based Spectral Analysis Methodology, Springer-Verlag, New York, 1989, pp.69.

[29] Graff, K. F., Wave Motion in Elastic Solids, Oxford University Press, London, 1975.

[30] Next Generation Space Telescope (NGST) Study Proposal, 1996.

[31] Thornton, E. A., Thermal Structures for Aerospace Applications, AIAA Education-Series, J.S. Przemienecki (Ed.), AIAA, Inc., Reston, 1996.

[32] Gutierrez, H., finite element model of NGST, M.I.T, 1997.

[33] Gutierrez, *H.,* "Jitter Analysis and Mitigation Conceptual Design", presented at *M.I.T. Space Systems Laboratory Semina*r, 1997.

[34] Dunn, C., "The Design, Construction, and Testing of a Composite Microsatellite Structure," Master's Thesis, M.I.T., 1999.

[35] TEK Hardware Reference Manual, Tektronix, 1989.

[36] Barlow, M. S., The Dynamics of Deployable Truss Structures in Zero-gravity: The MODE STA Results," Master's Thesis, M.I.T., 1992.

[37] Ingham, M., "Microdynamics and Thermal Snap Response of Deployable Space Structures," Master's Thesis, M.I.T., 1998.

[38] Juvinall, R. C. and Marshek, K. M., Fundamentals of Machine Component Design, 2nd Ed., John Wiley and Sons, New York, 1991, pp.367.

[39] Warren, P. A., and Peterson, L. D., "Sub-micron Mechanical Stability of a Prototype Deployable Space Telescope Support Structure," *Proceedings of the 38th AIAA/ ASME/ASCE/AHS/ASC Structures, Structural Dynamics and Materials Conference,* Kissimmee, April, 1997.

[40] Levine, M. B., "The Interferometry Program Experiments: IPEX I&II," P*roc. SPIE Astronomical Telescopes and Instrumentation Conference*, Kona Hawaii, March, 1998, Paper 3350-14.

[41] Ingham, M., finite element model of IPEX II truss, M.I.T., 1998.

Appendix A

FRICTION TEST RESULTS

The results from the mechanical tests on the slip joint is presented. The friction ratio f_k is plotted as a function of loading rate in Figure [Figure A.1].
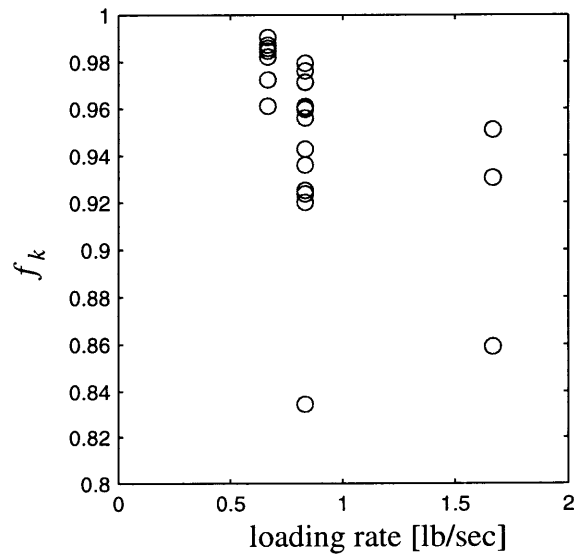

Figure A.1 Friction parameter vs. loading rate

17